DNA-mediated assembly of optical components for light manipulation at the nanoscale

Francesca Nicoli

München 2018

DNA-mediated assembly of optical components for light manipulation at the nanoscale

Francesca Nicoli

Dissertation

durchgeführt an der Fakultät für Physik

der Ludwig–Maximilians–Universität

München

vorgelegt von

Francesca Nicoli

aus Bergamo, Italien

München, den 04.09.2018

Erstgutachter: Prof. Dr. Tim Liedl

Zweitgutachter: PD Dr. Theobald Lomüller

Tag der mündlichen Prüfung: 30.10.2018

Contents

List of publications

Publications that are part of this work

- Nicoli, F.; Roos, M. K.; Hemmig, E. A.; Di Antonio, M.; de Vivie-Riedle, R.; Liedl, T. Proximity-Induced H-Aggregation of Cyanine Dyes on DNA-Duplexes. *J. Phys. Chem. A* **2016**, *120* (50), 9941–9947.
- Nicoli, F.;* Barth, A.;* Bae, W.; Neukirchinger, F.; Crevenna, A. H.; Lamb, D. C.; Liedl, T. Directional Photonic Wire Mediated by Homo-Förster Resonance Energy Transfer on a DNA Origami Platform. *ACS Nano* **2017**, *11* (11), 11264–11272.
- Zhang, T.;* Nicoli, F.;* Pilo-Pais, M.; Liedl, T. Facile and Fast DNA-Functionalization of Quantum Dots Using Purine Nucleotide-ZnS Affinity. *J. Am. Chem. Soc.* **2018**, (under review)
- Nicoli, F.; Zhang, T.; Jin, B.; Selbach, F.; Argyropoulos, C.; Liedl, T.; Pilo-Pais, M. DNA Mediated Self-Assembly of Plasmonic Antennas with a Single Quantum Dot in the Hot Spot. *ACS Nano* **2018**, (under review).

* these authors contributed equally to the work

Publications that are not part of this work

- Funck T.; Nicoli F.; Kuzyk A.; Liedl T. Sensing Picomolar Concentrations of RNA Using Switchable Plasmonic Chirality. *Angew. Chem. Int. Ed.* **2018**

Zusammenfassung

Die Selbstorganisation von DNA ist eine leistungsstarke Bottom-Up-Herstellungstechnik, die es ermöglicht, Billionen von Nanostrukturen parallel zu produzieren. Dank der molekularen Erkennungseigenschaften und der intrinsisch hohen räumlichen Auflösung des DNA-Moleküls sind alle diese Strukturen hochgradig adressierbar und erlauben die präzise Steuerung der Position von Nanokomponenten und deren Distanzen zueinander. Diese Eigenschaften ermöglichen die Manipulation der Licht-Materie-Wechselwirkung auf der Nanoskala, wo die physikalischen Phänomene und die Eigenschaften von Strukturen von der gegenseitigen Anordnung und dem Abstand ihrer Komponenten abhängen. In dieser Arbeit werden verschiedene optisch aktive Nanokomponenten wie Fluorophore, Halbleiter-Quantenpunkte und metallische Nanopartikel in maßgeschneiderten Konfigurationen angeordnet, um verschiedene physikalische Phänomene zu untersuchen. Im ersten Teil dieser Arbeit werden DNA-Nanostrukturen verwendet, um zwei spezifische Prozesse der Lichtsammlung nachzuahmen: Farbstoff-Farbstoff-Kopplung und Fern-Energietransport. Die Kopplung von zwei Cyanin-3-Farbstoffen wird durch kovalente Verknüpfung der Moleküle mit einem DNA-Gerüst gesteuert. Durch Variation ihrer Entfernung im Sub-Nanometer-Maßstab wird eine H-Dimerisierung beobachtet. Um den Langstrecken-Energietransport zu untersuchen, wird eine 16 nm lange photonische Leitung auf einer DNA-Origami-Plattform montiert. Die Energiekaskade von einem primären Donor zu einem letzten Akzeptor wird durch Fluorophore der gleichen Art vermittelt, die in der Lage sind, einen Energietransfer durchzuführen. Dank der Modularität des DNA-Origami ist es möglich zu bestimmen, dass das Phänomen der Homo-Energieübertragung zu einer insgesamt verbesserten Ende-zu-Ende-Übertragungseffizienz führen kann. Im zweiten Teil dieser Arbeit wird die DNA-Selbstorganisation verwendet, um die Exziton-Plasmon-Kopplung zu untersuchen, indem ein kolloidaler Quantenpunkt in der Lücke zwischen zwei Goldnanopartikeln positioniert wird. Zu Beginn wird eine neue Methode zur Funktionalisierung kolloidaler Quantenpunkte mit DNA entwickelt. Diese neue Technik beruht auf der Affinität zwischen DNA-Basen und der Oberfläche der Nanopartikel. Im Gegensatz zu bestehenden Verfahren erfordert es keine chemisch modifizierte DNA oder spezielle Ausrüstung und kann bei Raumtemperatur in nur 15 Minuten durchgeführt werden. Anschließend werden einzelne Quantenpunkte in den Hot Spot von Plasmonenantennen aus 40 nm Goldnanopartikeln platziert. Die Anordnung basiert auf DNA-Komplementarität, Stöchiometrie und sterische Hinderung und kann auf verschiedene Materialien erweitert werden. Da nur kurze DNA-Stränge benötigt werden, um die Komponenten zu verbinden, besitzen diese Antennen eine sehr kleine Lücke (~ 6 nm), die wichtig ist, um hohe Purcell-Faktoren und plasmonische Verstärkung zu erreichen. Mit diesen Strukturen wird eine bis zu 30-fache Fluoreszenzzunahme im Vergleich zu Quantenpunkten ohne Antenne erreicht.

Abstract

DNA self-assembly is a powerful bottom-up fabrication technique that enables the realization of trillions of nanodevices in a parallel manner. Thanks to the molecular recognition properties and the intrinsically high spatial resolution of the DNA molecule, all of these devices are highly addressable and allow sub-nanometer precise control over the distance and the positioning of nano-components. These features are highly desirable for the manipulation of light-matter interaction at the nanoscale, where the physical phenomena and the properties of devices depend on the reciprocal arrangement and distance of their components. In the work presented here, DNA self-assembly is used to arrange different optically active nano-components, such as fluorophores, semiconductor quantum dots and metallic nanoparticles, in custom-tailored configurations, in order to explore specific physical phenomena.

In the first part of this work, DNA nanostructures are used to mimic two specific processes of light harvesting: dye-dye coupling and long-range energy transport. The coupling of two cyanine 3 dyes is controlled by covalently linking the molecules to a DNA stand. By varying their distance at sub-nanometer scale, an H-type dimerization is observed. To study long-range energy transport, a 16 nm photonic wire is assembled on a DNA origami platform. The energy cascade from a primary donor to a final acceptor is mediated by fluorophores of the same kind able in order to perform homo-energy transfer. Thanks to the modularity of DNA origami, it is possible to demonstrate that the homo-energy transfer phenomenon can indeed lead to an overall enhancement in end-to-end transfer efficiency.

In the second part of this work, DNA self-assembly is used to study exciton-plasmon coupling by positioning a colloidal quantum dot in the gap between two gold nanoparticles. To start, a new method for functionalizing colloidal quantum dots with DNA is developed. This new technique relies on the affinity between DNA bases and the capping shell of the nanoparticles. Opposed to existing methods, it is fast, does not require chemically modified DNA or specialized equipment, and it can be carried out at room temperature in as short as 15 minutes. Subsequently, single quantum dots are placed inside the hot-spot of plasmonic antennas consisting of pairs of 40 nm gold nanoparticles. The assembly is based on DNA complementarity, stoichiometry, and steric-hindrance principles, and can be extended to different materials. Since only short DNA strands are required to link the components, these antennas possess a very small gap (~6 nm), which is important to achieve high Purcell factors and plasmonic enhancement. With these devices, an increase in fluorescence of up to 30-fold is obtained in comparison to quantum dots that are not placed within the antenna.

1 Light manipulation at the nanoscale

Nanoscale optically active components, such as organic fluorophores, colloidal metallic nanoparticles and semiconductor quantum dots, strongly interact with light at the nanoscale, due to their intrinsic electronic properties and their size smaller than the wavelength of light.[1–3] Being able to tune these interactions is of great importance for both the study of fundamental physical principles and the artificial manipulation of their optical properties. One way of achieving this control is to spatially arrange and combine the nanocomponents in a custom, tailored manner.[4,5]

Even though very different phenomena are presented in this work, the important underlying thread is the use of DNA as a building block for nanometer- and sub-nanometer-precise fabrication.[6,7] Throughout this work, DNA nanotechnology is the starting point for the study of diverse optical phenomena arising from the interaction between different nano-optical components. In chapter 2 a dedicated section explains in detail how DNA nanotechnology allows simple one-pot self-assembly of trillions of devices in solution. Such nanostrcuctures can be measured both in bulk and in single-molecule setups, making them easily adaptable to different investigation techniques. Their versatility, precise addressability, and ease of fabrication make DNA-mediated self-assembled structures extremely good candidates for pushing the limits of light-matter interactions at the nanoscale. [8–10]

A large portion of this work is dedicated to DNA self-assembly for light harvesting. I focused on the construction of precisely arranged systems of fluorophores to enable dye coupling and energy transfer. A profound understanding of these phenomena is fundamental for achieving efficient light harvesting and energy transport, with potential applications in the field of photovoltaics. The aim is to control the coupling strength and the energy transfer capabilities of an ensemble of chromophors, in a similar manner as nature does in natural light harvesting complexes (LHCs). Plants and photosynthetic bacteria have the ability to efficiently collect light throughout the visible spectrum, transfer it to a reaction center, and transform it into chemical energy for sugar synthesis.[11–13] The high efficiency of the collection process is made possible by arrangement of the LHCs with respect to the reaction center and the precise spatial control over the chromophores, such as chlorophylls and carotenoids, inside the LHCs (see figure 1-1). In order to maximize the energy transfer efficiency these dyes are closely spaced and their reciprocal orientation needs to be favorable for a strong dipole-dipole interaction. Since the exciton formed by absorbed light has to travel over long distances, it is ideal to avoid an energy penalty resulting from funneling the excitation from dyes of higher to lower energy. Nature overcomes this issue by transferring the exciton over many chromophores of the same kind, gaining transport length without energy loss. Additionally, even though light collection is performed by a limited set of light absorbing molecules, it covers large portions of the visible spectrum. Thanks to the close spacing between the chromophores, their molecular orbitals can interact, resulting in a modified absorption spectrum compared to that of the single molecule. These new energy states, created through orbital coupling, expand the spectral range in which LHCs can absorb light.[14–19]

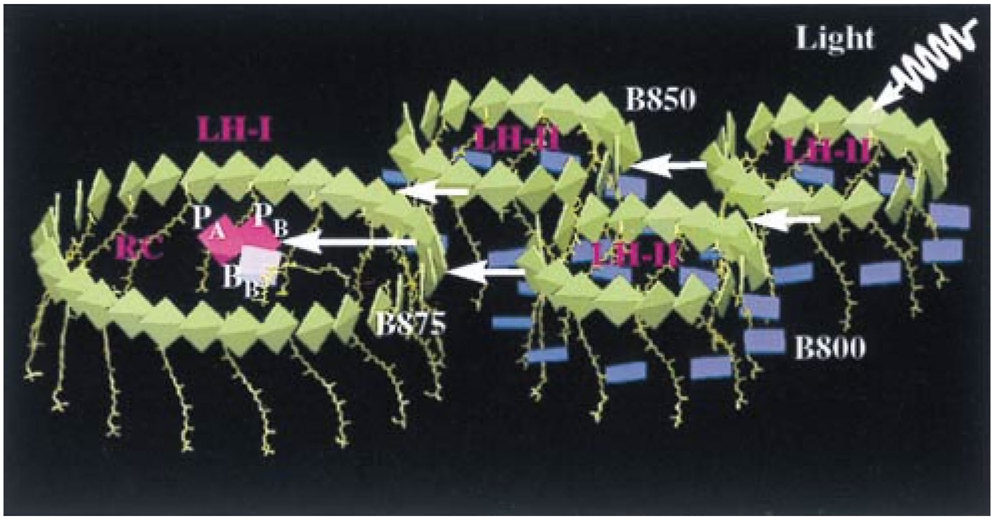

Figure 1-1 Schematic representation of light absorption and energy transfer in natural LHCs. *The light absorbed by the chromophores in the LHCII is transferred through a series of steps to the LHC I and the reaction center. Reproduced with permission from Ref. 18 copyright (1998) National Academy of Sciences, U.S.A.*

Inspired by natural LHCs, I used different DNA scaffolds to arrange dyes in a pre-determined manner to study dye-dye coupling and long range energy transfer. In chapter 3 I demonstrate the control over dye-dye coupling by creating a H-type aggregation of two cyainine3 molecules linked to a DNA strand.[20] The close-range interaction is modulated by their precise sub-nanometer spacing on the DNA and the rigidity of the polymer. In chapter 4 I look at nanometer-range energy transfer between dyes, focusing on the effect that multiple dyes of the same kind have on the overall energy transfer.[21]

Here I use a rigid 3D DNA origami structure as a template to assemble a liner chain of three green fluorophores flanked on each side by a blue and red dye, with a relative spacing of 3 to 5 nm. The energy is transferred from the high to the low energy dye through the intermediate chain of green fluorophores. It is shown that the presence of multiple intermediate energy dyes results in a more efficient energy transfer. The nanometer precise arrangement of the chain and the selective incorporation of dyes is achieved thanks to the high addressability of the DNA origami structure, as explained in details in section 2.4.6.

Chapters 5 and 6 are dedicated to creating hybrid assemblies of metal nanoparticles (MNPs) and quantum emitters (QEs), in order to shape their optical response to incident light. When illuminated at the resonance frequency the free electrons in MNPs undergo collective oscillations called plasmons. These charge oscillations produce a strong electromagnetic field that is highly localized to a few nm from the particle surface.[1,22,23] If two NPs are brought in close proximity their plasmons start to interact with each other and the electric field is now concentrated in the gap between the particles, a region called "hot-spot". Due to the ability of confining and enhancing the incoming radiation, metallic NPs can be thought of as nano-optical antennas.[24–26] If a molecule, such as a QE, is placed in the hot-spot region, its optical response is greatly modified by its interaction with the field. The electric field has two effects which depend on its strength and spatial confinement. The first increases the absorption of the QE. The second produces a "cavity effect", where the available quantized states of the field concentrated in the small mode volume increase the emission rate of the emitter, so called Purcell effect. If the coupling between the cavity and the QE is in the weak regime, the QE can radiate into free space and these devices display an enhanced fluorescence emission.[27–30] Given the localized nature of the hot-spot region, in order to promote QE-plasmon interaction one has to be able to place the QE with nanometer precision in respect to the MNPs.

Again I use the nanometer precise assembly capabilities of the DNA molecule to deterministically place a QE, in the form of a colloidal quantum dot (QD), in the hot-spot region created in the gap between two 40 nm gold NPs (AuNPs). In chapter 5 I illustrate the development of a new method to conjugate DNA and colloidal QDs, which is a fundamental requirement to interface the component with DNA self-assembly. It is shown how by exploiting the chemical affinity between specific DNA bases and the zinc (Zn) shell of the QDs, I can attach the desired DNA strand to the particles.[31] In chapter 6 I establish a new assembly technique to build antenna-QD complexes. I discuss the advantage of these QD-antenna complexes over the state of art devices and why I think such structures are ideal for enabling exciton-plasmon coupling, bringing the realization of tunable single photon sources and ultra-fast optoelctronic devices a step closer to practical realization.[32]

2 Theoretical background

This chapter describes the physical principles governing the phenomena presented in this work, such as energy transfer and plasmon-exciton interaction. The chapter is divided in four sections: the first part is dedicated to fluorescence and fluorescent molecules; the second part draws a parallel between the quantum mechanical model of “particle in a box” and the behavior of cyanine dyes and quantum dots; the third part is focused on MNPs and the interaction between plasmons and excitons; the last section is dedicated to introducing the field of DNA nanotechnology and DNA self-assembly techniques.

2.1 Photophysics of organic dyes: fluorescence and energy transfer

When light interacts with matters different phenomena can arise; light can be either scattered through elastic or inelastic scattering, or absorbed. Absorption of light by matter may lead to luminescence of the compound, for example chemical luminescence, thermal luminescence and photoluminescence. Photoluminescence is the process in which a molecule, upon the absorption of a photon, emits light into space only due to internal electronic transitions, without any change of the chemical state. This type of emission is also different from thermal radiation, because it does not rely on heating. Many processes can take place after the absorption of a photon, for example intersystem crossing, molecular quenching, internal conversion, phosphorescence and fluorescence. Fluorescence is the phenomenon in which the decay of the electron from the excited state to the ground state, without changing its spin, results in the emission of a photon.

Unless stated otherwise, this section is mainly based on the following books: “Principles of Fluorescence Spectroscopy” by J. Lakowicz,[33] “Molecular Fluorescence” by B. Valeur[3] and “Handbook of Fluorescence Spectroscopy and Imaging” by M. Sauer, J. Hofkens and J. Enderlein.[34]

2.1.1 Absorption

In organic molecules, such as fluorophores, the absorption of a photon can promote the electronic transition from ground state (lower energy) to excited state (higher energy). The transition takes place from the highest occupied molecular orbital (HOMO) to the lowest unoccupied molecular orbital (LUMO). Molecular orbitals are classified in σ, π and n depending on the type of bond between atoms. In fluorophores, such as cyanine dyes, the orbitals responsible for the electronic transition in the visible range originate from a π-type bonding. The π-bond, together with the higher energy σ-bond, originates from the formation of carbon double bond (C=C), typical of organic molecules. A π-orbital consists of the horizontal hybridization of two p-atomic orbitals of the carbon atoms. According to molecular orbital theory, the formation of a π-bond generates a boding π-orbital and an anti-bonding π^*-orbital. The absorption of a photon promotes the vertical transition of one electron in the bonding π-orbital to the anti-bonding π^*-orbital (see figure 2-1). The transition from HOMO to LUMO conserves the spin of the electron, meaning that the ground and the excited state have the same spin multiplicity ($\mathrm{M} = 2\mathrm{S} + 1$) of $\mathrm{M} = 1$, and they are therefore called singlet states (S). After excitation, spin-orbital coupling can result in a transition involving a change of spin (intersystem crossing). In this case the electron goes from the excited singlet state to a triplet state, (T), of lower energy with $\mathrm{M} = 3$.

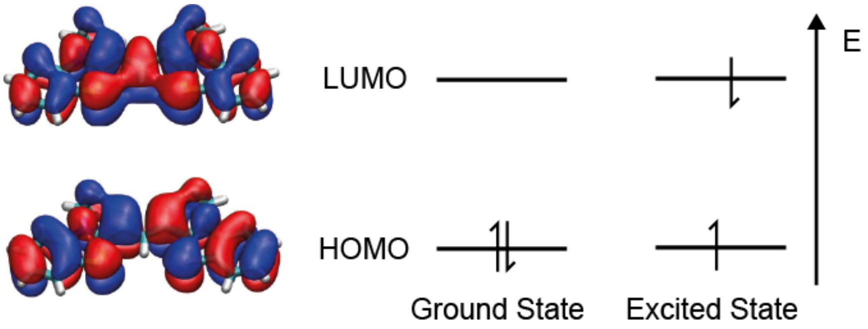

Figure 2-1 Molecular orbitals and HOMO-LUMO transition. *Molecular orbitals corresponding to the HOMO and LUMO states of a Cy3 molecule and scheme of the electronic transition from the ground top the excited state.*

The probability of a photon to be absorbed by a molecule is measured by absorbance. The measurement can be carried out in solution by quantifying the amount of light absorbed by the liquid containing the molecule of interest. The absorbance at a specific wavelength, λ, is defined as:

$$A(\lambda) = \log\frac{I_0(\lambda)}{I(\lambda)} \tag{2.1}$$

here $I_0(\lambda)$ is the intensity of the beam entering the sample and $I(\lambda)$ is the beam intensity leaving the sample. Absorbance of a dilute solution of fluorophores obeys the Beer-Lambert law:

$$A(\lambda) = \varepsilon(\lambda) * c * l \tag{2.2}$$

where c is the concentration of absorbing molecules in the sample,l the length the beam travels in the sample, and $\varepsilon(\lambda)$ is the molar absorption coefficient, which quantifies the ability of the molecule to absorb photons. When a molecule is excited at a frequency in resonance with an allowed transition, the absorption of a photon, and subsequent promotion of an electron to a higher energy state, creates a displacement of charges which generates a transient dipole moment oscillating at the frequency of the incident field. ε is related to the dipole oscillator strength f of the electronic transition moment and the photon cross-section $\sigma(\lambda)$ of the molecule. The value of f is different for each orbital transition, and it determines which one is more favorable, while $\sigma(\lambda)$ depends on the area of the molecule that can interact with photons. Typical molar absorption values for the $\pi \rightarrow \pi^*$ transition of an organic dye are on the order of $\sim 10^5\ M^{-1}cm^{-1}$. The oscillator strength and how it relates with the absorption and emission spectrum of a molecule are very important to describe the phenomenon of resonance energy transfer, so they will be described in detail in section 2.1.6.

2.1.2 Spectral broadening

In addition to electronic states, a molecule possesses also vibrational states associated with the thermal motion of its atomic nuclei. The vibrations occur on a longer timescale than electronic transitions, $10^{-10} - 10^{-12}\ s$ and $10^{-15}\ s$, respectively. This difference in time scale implies that during the absorption of a photon the molecule does not change its initial vibrational state and the electron undergoes a vertical transition. The population of electrons in the vibrational states follows the Boltzmann distribution, so at room temperature most of the electrons in the ground state have the energy of the lowest vibrational state. The energy of these states is on the order of $\sim k_b T$, two orders of magnitude lower than the energy of the electronic transition. All the energy levels and transitions of a molecule can be described schematically with the *Jablonski diagram* in figure 2-2. Since each electronic level contains multiple vibrational energy states, the absorption and emission spectra appear as broadened Lorentzian distributions, compared to for example single atoms. The electronic transitions between singlet states take place mostly from the lower vibraitional state of $\mathrm{S_0}$ ($\mathrm{S_{0-0}}$) to one of the vibrational states of the $\mathrm{S_{n-m}}$ (where $\mathrm{n} \geq 1$ and $\mathrm{m} \geq 0$), depending on the energy of the absorbed photon. The probability of the molecule to absorb photons in a certain energy range is reflected by the shape of the absorption spectrum $\varepsilon(\lambda)$.

2.1.3 Fluorescence and other competing processes

After the absorption process has caused a vertical, electronic transition, the electron stays in the excited state for a time that is much larger than other energy-lowering processes (see table 2-1), that can therefore take place before, and compete with, the electronic decay.

Internal conversion (IC) occurs between states with the same spin multiplicity, meaning the transitions happen only from singlet to singlet or triplet to triplet state. It is a non-radiateve phenomenon which brings the molecule from higher excited states, $\mathrm{X_n}$ (with $\mathrm{X = S}$ or T and $\mathrm{n} > 1$), to the lowest excited state $\mathrm{X_1}$. Although less efficiently than from $\mathrm{S_2}$ to $\mathrm{S_1}$, IC can also happen between $\mathrm{S_1}$ and $\mathrm{S_0}$ states, competing with fluorescence emission. Vibrational relaxation takes place within a certain electronic level $\mathrm{X_n}$ ($\mathrm{n} \geq 0$), when the molecule is in a higher state than $\mathrm{X_{n-0}}$. This process brings the energy of the electron to the lowest vibrational state of the respective electronic level. The vibrational energy lost by the molecules is transferred to the solvent in which they are immersed.

Energy Transition Process	Characteristic Times [s]
Absorption	10^{-15}
Vibrational Relaxation	$10^{-12} - 10^{-10}$
Lifetime of Excited State $\mathrm{S_1}$ (Fluorescence)	$10^{-10} - 10^{-7}$
Intersystem Crossing	$10^{-10} - 10^{-8}$
Internal Conversion	$10^{-11} - 10^{-10}$
Lifetime of Excited State $\mathrm{T_1}$ (Phosphorescence)	$10^{-6} - 1$

Table 2-1 Characteristic times of energy transition processes in organic fluorophores

The electron at the lower vibrational state of the first single state, $\mathrm{S_{1-0}}$, can decay to the singlet ground state $\mathrm{S_{0-m}}$ by emitting a photon, this process is called fluorescence. The molecule emits photons with a certain energy distribution described by the shape of the emission spectrum. Even though the electronic transition has the same energy, the distribution of the emitted photons is red-shifted compared to absorption. This effect is called the Stoke shift and it is caused by the broadening of the electronic levels due to the presence of vibrational states. When decaying the electron can either go directly to the lower vibrational state of the singlet ground state through the transition $\mathrm{S_{1-0}} \rightarrow \mathrm{S_{0-0}}$, or it can decay to a higher vibrational state $\mathrm{S_{1-0}} \rightarrow \mathrm{S_{0-m}}$. In the latter case, the electron undergoes vibrational relaxation from $\mathrm{S_{0-m}}$ to $\mathrm{S_{0-0}}$. The concepts of spectral broadening and Stoke shift are fundamental for the phenomenon of homo-resonance energy transfer illustrated in chapter 4.

Another process that can take place after the absorption of a photon and can decrease the fluorescence emission is called intersystem crossing (ISC). ISC refers to the case where an electron undergoes a spin-forbidden transition between electronic states of different multiplicity, for example from the singlet state S_1 to the triplet state T_1. This process is possible due to spin-orbit coupling of the electrons in the molecule, and its efficiency strongly depends on the type of molecular orbital. Since the time scale at which ISC and fluorescence emission occur are comparable (Table 1), the two processes often compete. Due to the long lifetime of the electron in the state T_1, the molecule undergoes several collisions with the solvent, leading to radiationless de-excitation. Furthermore during this time, the molecule is more prone to oxidation, which results in photo-bleaching. For some compounds, typically in the solid form, the transition $T_1 \rightarrow S_0$ can happen through emission of a photon. This phenomenon is called phosphorescence.

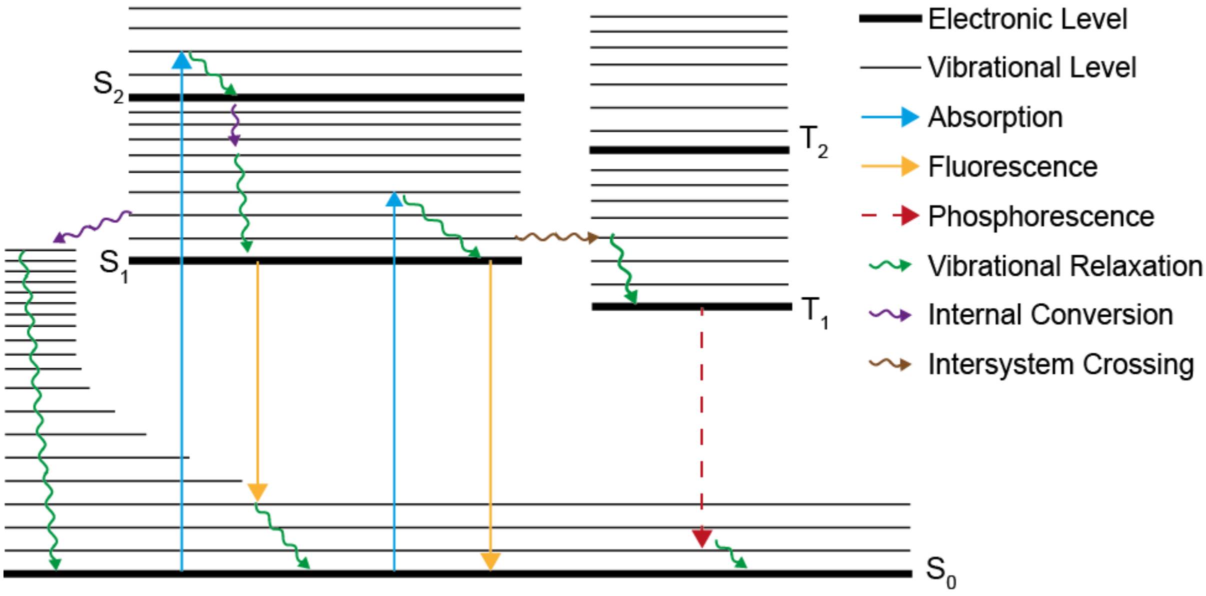

Figure 2-2 Jablonski Diagram. *Scheme of the possible transitions taking place in a fluorophore. Electronic transitions are indicated by a straight arrow, while other processes (vibrational relaxation, IC and ISC) are indicated by a wavy arrow. The electronic and vibrational levels are indicated by a bold and fine line, respectively.*

2.1.4 Einstein coefficients: probabilistic description of spontaneous emission

After the phenomenological description of absorption and emission, a fundamental question has to be answered: how do electrons in the excited state decay to the ground state? Before the formal quantum mechanical description of the concept vacuum and its quantized states was developed, absorption and emission were considered intrinsic properties of the molecule, and treated as probabilistic processes. In this paragraph a brief summary of this description is presented. In section 2.3.5 the quantum electrodynamics description is presented in relation to cavities and their ability to modify the spontaneous emission rate. The derivation in this section is mainly based on the following books: "Quantum optics" by M. Fox[35] and "Principles of nano-optics" by L. Novotny and B. Hecht[36]

In the quantum mechanical description of light absorption and emission from a two-level system, the energy of the exciting and emitted photon has to be equal to the energy difference between the lower and higher electronic state $\hbar\omega_0 = E_2 - E_1$, where $\omega_0$is the angular frequency of the photon. Once a molecule or atom is excited, it will not remain on this excited state forever but it will rather decay to the ground state, even in the absence of external perturbation. This decay probability is called spontaneous emission. Einstein provided a probabilistic description of the excitation and de-excitation processes introducing three different coefficients corresponding to spontaneous emission, A_{21} , absorption, B_{12} , and stimulated emission, B_{21} . The model system under consideration in his description is a black box in thermal equilibrium, filled with N particles, which cannot collide with each other and can only interact with the incident radiation field in the box.

Absorption and stimulated emission take place when the molecule interacts with the incoming field which has a certain spectral energy density $\rho(\omega)$. The population of molecules in the ground state N_1 brought to the excited state by the incident filed is:

$$-\frac{dN_1}{dt} = B_{12}\, N_1 \rho(\omega) \tag{2.4}$$

The field also causes stimulated emission which acts as a de-populating phenomenon of the molecules in the excited state represented by the population N_2:

$$-\frac{dN_2}{dt} = B_{21}\, N_2 \rho(\omega) \tag{2.5}$$

These coefficients are not independent; in fact at thermal equilibrium and in absence of spontaneous emission, the number of molecules undergoing an upwards transition must be equal to the number of decaying molecules:

$$B_{12}\, N_1 = B_{21}\, N_2 \tag{2.6}$$

Since the molecules are in thermal equilibrium at temperature T, the population of molecules should follow the Boltzmann distribution:

$$\frac{N_2}{N_1} = e^{-\frac{\hbar\omega}{k_B T}} \tag{2.7}$$

The contradiction between equations 2.6 and 2.7 forced Einstein to incorporate a Spontaneous emission term, A_{21}, assumed to be a pure probabilistic process, independent of the incident radiation, and an intrinsic property of the molecule. Taking into consideration the population of excited molecules N_2, the decay follows the following rate equation:

$$-\frac{dN_2}{dt} = A_{21}\, N_2 \tag{2.8}$$

The condition of equal upwards and downwards transitions at thermal equilibrium is now:

$$B_{12}\, N_1 \rho(\omega) = A_{21}\, N_2 + B_{21}\, N_2 \rho(\omega) \tag{2.9}$$

The Boltzmann distribution including the new spontaneous emission term becomes:

$$\rho(\omega) = \frac{{A_{21}}/{B_{21}}}{\left({B_{12}}/{B_{21}}\right) e^{\frac{\hbar\omega}{k_B T}} - 1} \tag{2.10}$$

The field spectral density in the box at thermal equilibrium corresponds to the black body radiation:

$$u(\omega) = \frac{\hbar\omega^3}{\pi^2 c^3} \frac{1}{e^{\frac{\hbar\omega}{k_B T}} - 1} \tag{2.11}$$

In order for equations 2.10 and 2.11 to hold true, follows that:

$$B_{12} = B_{21} \tag{2.12}$$

and:

$$A_{21} = \frac{\hbar\omega^3}{\pi^2 c^3}\, B_{21} \tag{2.13}$$

The Einstein coefficients representing the transition rates of the molecule can also be calculated from a quantum mechanical point of view where the emission is treated as a time-dependent perturbation. According to Fermi's golden rule, the transition from state 1 to state 2 is given by:

$$\gamma_{1\to 2} = \frac{2\pi}{\hbar}|M_{12}|^2\rho(\omega) \qquad (2.14)$$

where $\rho(\omega)$ corresponds to the density of final states, and M_{12} is the matrix element. The density of states is a very important parameter in the description of spontaneous emission. Considering an excited two-level system, when the electron returns to the ground state, the photon is emitted into free space that is quantum mechanically described as a continuum of states (see section 2.3.5 for a more detailed explanation on the density of states of the vacuum). The number of modes (or states) in free space in the volume between $E = \hbar\omega$ and $E + dE$ is proportional to ω^2. The matrix element in Fermi's golden rule depends on the wave functions of the initial and final state of the molecule, $\psi_1(r)$ and $\psi_2(r)$ respectively, and on the Hamiltonian of the perturbation, H':

$$M_{12} = \langle 2|H'|1\rangle = \int \psi_2^*(r)\, H'\psi_1(r) \qquad (2.15)$$

where r indicates the position of the electron.

In order to calculate the perturbation, the interaction between the electric field and the dipole of the molecule has to be considered. Here, only the electric field-dipole interaction is considered, because magnetic interactions and higher order multipoles are orders of magnitude weaker. When the electric field $\vec{E}_0$ excites an electron, the charge separation in the molecule creates a transient dipole moment $\vec{p} = -e\vec{r}$. The Hamiltonian of perturbation can be written as:

$$H' = -\vec{p}\cdot\vec{E}_0 = e\,(xE_x + yE_y + zE_z) \qquad (2.16)$$

Assuming that compared to the size of the molecule, the electric field is constant along each direction, the matrix element becomes:

$$M_{12} = eE_x \int \psi_2^*(x)\, x\psi_1(x) dr^3 \qquad (2.17)$$

For the x polarization of the electric filed. The electric dipole moment of the transition, μ_{12}, can be written as:

$$\mu_{12} = \; -e\int \psi_2^*(x)\, x\psi_1(x) dr^3 = -e\langle 2|x|1\rangle \qquad (2.18)$$

for y and z directions the same formula holds true for both, the matrix element and the dipole transition. The matrix element therefore becomes:

$$M_{12} = -\vec{\mu}_{12}\cdot\vec{E}_0 \qquad (2.19)$$

In this description, the electric dipole of the transition is a property of the molecule since it depends on the wave function of the initial and final state. Since the absorption and emission rates are determined by $\vec{\mu}_{12}$, they should in principle be absolute values. However this conclusion does not hold true, because of the density of states of the environment surrounding the molecule. In section 2.3.5 it will be shown how the rates can be modified by the cavity effect, which changes the density of states of the vacuum.

The transition rate can calculated from Fermi's golden rule knowing the density of states $\rho(\omega)$ and the perturbating electric field of the vacuum $\vec{E}_0$:

$$\rho(\omega) = \frac{\omega^2 V}{\pi^2 c^3} \tag{2.20}$$

$$E_0 = \left(\frac{\hbar\omega}{2\varepsilon_0 V}\right)^{1/2} \tag{2.21}$$

Both the density of sates and the vacuum field will be calculated in details in section 2.3.5. Substituting these two quantities in equation 2.14 (Fermi golden rule) gives:

$$W_{12} = \frac{\omega^3}{3\pi\hbar c^3 \varepsilon_0}\mu_{12}^2 \tag{2.22}$$

In the case of spontaneous emission, the rate is equal to Einstein coefficient A_{21}

2.1.5 Quantities describing fluorescence

As described in section 2.1.3, there are other processes, such as ISC and IC, which compete with fluorescence emission. Therefore the de-excitation of a molecule can be described by two rates: radiative decay, k_r, associated with the fluorescence emission, and a non-radiative decay, k_{nr}, associated with the competing processes. These two quantities are used to define two important parameters: the quantum yield, ϕ, which describes the brightness of the fluorophore, and the lifetime, τ, which describes the dynamics of the emission process.

The fluorescence lifetime can be described with rate equations by considering the decay of a population of excited molecules in solution:

$$-\frac{d[C^*]}{dt} = (k_r + k_{nr})\,[C^*] \tag{2.23}$$

where $[C^*]$ is the concentration of excited molecules in solution (the star indicates the excited state). The equation can be solved by integration and by defining $[C_0^*]$ as the concentration of excited molecules at time 0, for example after a short exciting laser pulse:

$$[C^*(t)] = [C_0^*] \cdot e^{-t/\tau} \tag{2.24}$$

Here τ is the fluorescence lifetime and is defined as:

$$\tau = \frac{1}{k_r + k_{nr}} \tag{2.25}$$

The lifetime describes the exponential decay of the photons intensity emitted from a molecule in the excited state. Importantly, it defines the time during which observation of the molecule is possible. Fluorescence lifetime can be measured by exciting either the bulk solution or the single molecules with a short laser pulse and recording the fluorescence decay with, for example, an avalanche photodiode. The fluorescence decay is then fitted with the exponential decay model and the lifetime extracted from the fit.

Some fluorophores, for example cyanine dyes, have multiple radiative lifetimes, due to their structure. When they are in the excited state they can undergo a *cis-trans* transition. While the dyes are in the *trans* conformation they do not radiate. In this case, a multi-exponential fit of the decay time is necessary to determine the lifetime values.

Another important parameter to describe the behavior of a fluorophore is its brightness, which is usually quantified in terms of quantum yield, ϕ. The quantum yield is defined as the ratio between the absorbed photons and the emitted photons. Considering the radiative and non-radiative decay, ϕ can be written as:

$$\phi = \frac{k_r}{k_r + k_{nr}} = k_r \cdot \tau \tag{2.26}$$

If all the absorbed photons were re-emitted through fluorescence decay ϕ would be equal to one, but, as described above, other radiationless processes compete with emission.

2.1.6 Resonance Energy Transfer

When a molecule is in the excited state its energy can be quenched by the presence of a second molecule. There are different mechanisms of fluorescence quenching, such as electron and proton transfer, excimer formation and energy transfer. The discussion in this section will be focused on resonance energy transfer. As the name suggests, in this process the energy is transferred from an excited donor molecule, (D), to an acceptor molecule (A) in a radiative or non-radiative manner. In case of D and A being two different molecules the transfer is called hetero-transfer, while if D and A are the same molecule it is called homo-transfer.

The content of this section, including the mathematical derivation, is based on the following book: “FRET - Förster Resonance Energy Transfer – From theory to applications” edited by I. Medintz and N. Hildebrandt.[37]

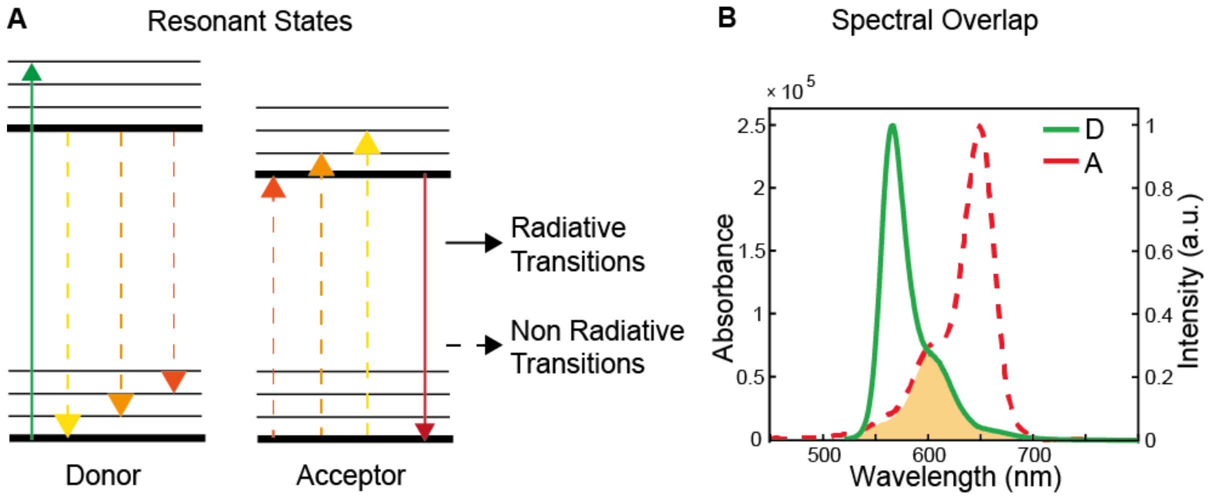

Figure 2-3 Resonant states and spectral overlap. *(A) Scheme of resonant states between a donor and an acceptor molecule. The arrows of the same color correspond to transitions that are in resonance. (B) Spectral overlap between the donor emission (green full fine) and the acceptor absorption (red dashed line). The overlap integral is colored in orange.*

The necessary condition for enabling energy transfer is the existence of resonant states between the donor and the acceptor energy states, as schematically shown in figure 2-3 A. The existence of these resonance states is manifested in the spectral overlap between donor emission and acceptor absorption (see figure 2-3 B). The spectral overlap is quantified by the overlap integral, $J(\lambda)$:

$$J(\lambda) = \int F_D(\lambda) * \varepsilon_A(\lambda) * \lambda^4 d\lambda \qquad (2.27)$$

which is the integrated area of the overlap between the normalized emission spectrum of the donor, $F_D(\lambda)$, and the extinction of the acceptor, $\varepsilon_A(\lambda)$.

The radiative-type of transfer can be described as a two-step process: the excited donor D^* emits a photon which is then absorbed by the acceptor A:

$$D^* \rightarrow D + h\upsilon \;\Rightarrow A + h\upsilon \;\rightarrow A^*$$

This process is known also as the “inner filter” effect, because some of the photons emitted by D^* are reabsorbed by the other molecules in solution, causing a decrease in emission intensity in the region of spectral overlap, resulting in a distortion of the emission spectrum of the donor.

Non-radiative transfer requires, in addition to the spectral overlap, some other interaction between the donor and the acceptor molecule. One type of interaction can be orbital overlap, which results in an electron exchange between the pair of molecules. This mechanism is known as Dexter-transfer and it is a very short range interaction, that takes place at distances $< 1\ nm$. Another non-radiative transfer relies on coulombic interactions, which are long range and therefore typically predominant at distances between $1 - 10\ nm$.

Resonance energy transfer occurring at long range is based on a radiationless exchange of energy *via* dipole-dipole interaction. It was originally described by Förster in 1946,[38] (ref. 38 is the English translation from the original paper: Förster, T. (1946) Naturwissenschaften, 33 , 166–175;) and therefore is known by the name Förster Resonance Energy Transfer (FRET). In Förster's description, the energy transfer is based on dipole-dipole interaction between the donor and acceptor, where the two molecules are approximated as point-dipoles. This approximation is valid if the size of the molecules is much smaller than the incident wavelength, and their distance from each other is larger than the molecular dimension. The transient dipole moment of the donor can be expressed as $\boldsymbol{p}_D = e\ D_D\widehat{\boldsymbol{d}}$, where e is the electron charge, D_D is the displacement of charges in the donor molecule, and $\hat{d}$ is the unit vector indicating the direction of the dipole moment. The donor dipole moment oscillates in a range of frequencies, ν_D, generating an electric filed, $\vec{E}_D$ at the location of the acceptor. The electric field of a dipole can be expressed as:

$$\mathbf{E}_\mathrm{D} = \frac{eD_D\left[3\left(\widehat{\boldsymbol{d}}\cdot\hat{\boldsymbol{r}}\right)\cdot\hat{\boldsymbol{r}} - \widehat{\boldsymbol{d}}\right]}{4\pi\varepsilon_0 n^2 R_{DA}^3}\cos(2\pi\nu_D) \tag{2.28}$$

The acceptor is positioned at a certain distance, R_{DA}, along the direction of $\hat{r}$, as illustrated in figure 2-4. The orientation factor of the two dipoles is defined according to the physical quantities in figure 2-4 as:

$$\kappa = \cos\theta_T - 3\cos\theta_D \cdot \cos\theta_A \tag{2.29.a}$$

$$\kappa = \widehat{\boldsymbol{d}}\cdot\widehat{\boldsymbol{a}} - 3\left(\widehat{\boldsymbol{d}}\cdot\hat{\boldsymbol{r}}\right)\cdot\left(\hat{\boldsymbol{r}}\cdot\widehat{\boldsymbol{a}}\right) \tag{2.29.b}$$

For two dipoles rotating freely in space the average value of κ^2 is $2/3$. This assumption becomes important when determining distances by means of transfer efficiency.

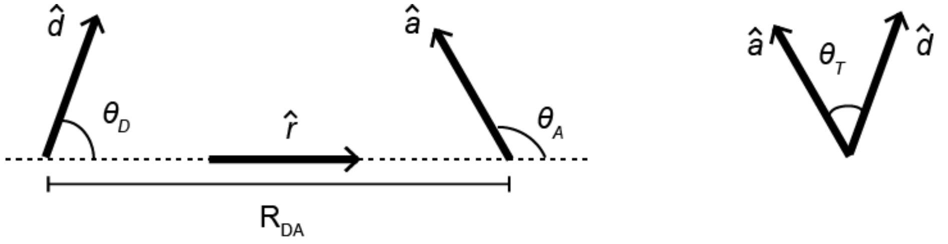

Figure 2-4 Schematic representation of the dipole orientation of a FRET pair. *The unit vectors $\hat{\boldsymbol{d}}$ and $\hat{\boldsymbol{a}}$ indicate the orientation of the donor and acceptor dipoles, respectively. The unit vectors $\hat{\mathbf{r}}$ indicates the direction of the separation distance between donor and acceptor* ($\mathbf{R_{DA}}$)*. The angles $\boldsymbol{\theta_D}$and $\boldsymbol{\theta_A}$represent the inclination of the donor and acceptor dipoles with respect to $\hat{\mathbf{r}}$. $\boldsymbol{\theta_T}$is the angle between the donor and acceptor dipole.*

The component of the electric field along the direction of the acceptor dipole, $\hat{a}$, is:

$$\mathbf{E}_\mathrm{D} \cdot \hat{\boldsymbol{a}} = \frac{-eD_D\kappa\cos(2\pi\nu_D)}{4\pi\varepsilon_0 n^2 R_{DA}^3} \tag{2.30}$$

Before describing in more detail the resonance condition and the transfer rate, it is important to see how the dipole moment relates with the spectral characteristics of the molecules. In case of the donor, the dipole strength $f_D(\nu)$ is related to the emission rate and is described by the donor emission spectrum $F_D(\nu)$, its quantum yield ϕ_D, and fluorescence lifetime τ_D (for the full derivation see book Chapter 3):

$$f_{eD}(\nu) = \frac{3(4\pi\varepsilon_0)m_e c^3\phi_D F_D(\nu)}{8\pi^2 n\nu^2 e\tau_D} \tag{2.31}$$

The oscillator strength of the acceptor is instead related to its absorption spectrum expressed in terms of the extinction coefficient $\varepsilon_A(\nu)$ (for the full derivation see ref. 37, chapter 3):

$$f_{aA}(\nu) = \frac{3(\ln 10)\,(4\pi\varepsilon_0)n\,m_e c\,\varepsilon_A(\nu)}{\pi N_A e^2} \tag{2.32}$$

where n is the refractive index of the medium in which the molecules are embedded, m_e and e are the mass and charge of the electron, respectively, and $N_A$is Avogadro’s number.

As mentioned above, resonance is a necessary condition for the energy transfer. This requirement implies that the frequency at which the donor oscillates has to partially overlap with the frequency at which the acceptor can be excited. The amount of energy transferred to the acceptor at time t depends of the difference between the oscillation frequency of the donor and the acceptor $\nu_D - \nu_A$. This resonance condition was expressed by Föster as an “all-or-nothing” condition. The energy transferred to the acceptor, W_A, is always zero, except at the resonance condition$-\frac{1}{2t} < \nu_D - \nu_A < \frac{1}{2t}$, where it becomes:

$$W_A = \frac{q_e^2 E_D^2}{8m_e} t^2 \tag{2.33}$$

E_D is expressed in terms of oscillation of charges and distance between the dipoles by equation 2.30. Substituting equation 2.30 in equation 2.33, the energy stored by the acceptor becomes:

$$W_A = \frac{e^4 D_D^2 \kappa^2 t^2}{8m_e (4\pi\varepsilon_0)^2 n^4 R_{DA}^6} \tag{2.34}$$

The energy stored by the oscillator is given by:

$$W_D = \frac{1}{2} k D_D^2 = 2\pi^2 m_e \nu^2 D_D^2 \tag{2.35}$$

By substituting D_D^2 with the oscillator strength given in equation 2.34, W_A becomes:

$$W_A = \frac{e^4 W_D \kappa^2 t^2}{16\pi^2 m_e^2 \nu^2 (4\pi\varepsilon_0)^2 n^4 R_{DA}^6} \tag{2.36}$$

The equation has to be extended over the range of frequencies of the donor emission expressed in terms of its oscillator strength$f_{eD}(\nu)$. Following Föster's all-or-nothing approximation, the frequency range of the acceptor absorption in resonance with the donor is $f_{aA}(\nu)\frac{1}{t}$. The probability for a photon to be emitted between $\nu + d\nu$ and meet the resonance is $f_{eD}(\nu)\, f_{aA}(\nu)\frac{1}{t}d\nu$. The energy transferred to the acceptor over the whole frequency range is:

$$W_A = \frac{e^4 W_D \kappa^2 t}{16\pi^2 m_e^2 (4\pi\varepsilon_0)^2 n^4 R_{DA}^6} \int_{-\infty}^{+\infty} \frac{f_{eD}(\nu)\, f_{aA}(\nu)}{\nu^2} d\nu \tag{2.37}$$

The transfer rate from D to A is obtained by differentiating eq. 2.34 with respect to time:

$$\frac{dW_A}{dt} = k_T W_D \tag{2.38}$$

Where k_T is:

$$k_T = \frac{e^4 \kappa^2}{16\pi^2 m_e^2 (4\pi\varepsilon_0)^2 n^4 R_{DA}^6} \int_{-\infty}^{+\infty} \frac{f_{eD}(\nu)\, f_{aA}(\nu)}{\nu^2} d\nu \tag{2.39}$$

The oscillator strength of donor emission and acceptor absorption relate to their respective spectra as described by equations 2.31 and 2.32. The rate expression then becomes:

$$k_T = \frac{9(\ln 10)\,\kappa^2 \phi_D}{128\pi^5 N_A \tau_D R_{DA}^6} \int_{-\infty}^{+\infty} \frac{c^4 F_D(\nu)\, \varepsilon_A(\nu)}{\nu^4} d\nu \tag{2.40}$$

The integral corresponds to the overlap integral expressed in terms of frequency instead of wavelength:

$$J(\nu) = \int_{-\infty}^{+\infty} \frac{c^4 F_D(\nu)\, \varepsilon_A(\nu)}{\nu^4} d\nu = \int_{-\infty}^{+\infty} F_D(\lambda) * \varepsilon_A(\lambda) * \lambda^4 d\lambda = J(\lambda) \tag{2.41}$$

The Förster radius can be defined as the constant:

$${R_0}^6 = \frac{9(\ln 10)\, \kappa^2 \phi_D}{128\pi^5 N_A \tau_D} J \tag{2.42}$$

which depends only on the spectral overlap of donor and acceptor, the quantum yield and the lifetime of the donor. Therefore the transfer rate for any given donor-acceptor pair depends only on their distance:

$$k_T = \frac{1}{\tau_D} \left(\frac{R_0}{R_{DA}}\right)^6 \tag{2.43}$$

The transfer efficiency can be expressed as the ratio of rates:

$$\epsilon = \frac{k_T}{\tau_D^{-1} + k_T} = \frac{R_0^6}{R_0^6 + R_{DA}^6} \tag{2.44}$$

As illustrated in figure 2-5, when the distance between donor and acceptor is equal to the Förster radius the transfer efficiency is exactly 0.5.

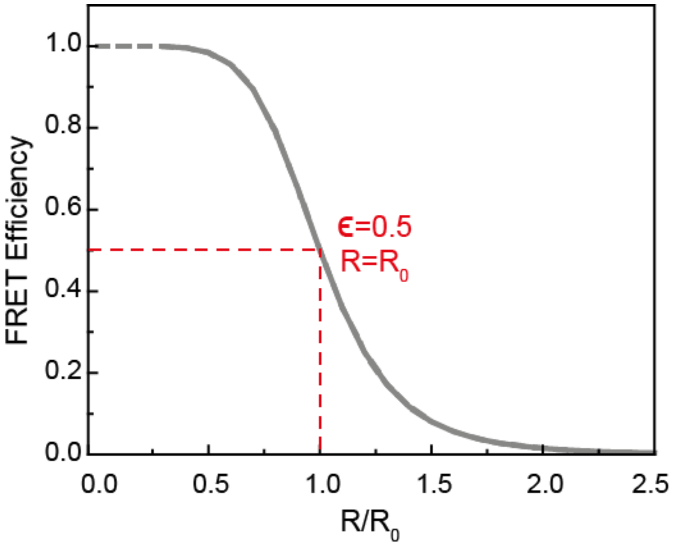

Figure 2-5 FRET efficiency curve. *Dependence of FRET efficiency on the distance between donor and acceptor* **R** *normalized by the Föster radius of the FRET pair* $\mathbf{R_0}$. *The curve is plotted from equation 2.44 where the* $\mathbf{R^{-6}}$*dependence of the efficiency is illustrated.*

2.2 Particle in a box in practice: cyanine dyes and quantum dots

The quantum mechanical concept of "particle in a box" describes the phenomenon of a particle, for example an electron, spatially confined in an energy potential $V(x)$ with infinitely high walls (see figure 2-6). The particle cannot escape the potential walls and this confinement results in the quantization of the particle's energy states and wave functions that can be calculated analytically. The derivation in this section is based on the following book: "Quantum mechanics" by B. H. Bransden and C. J. Joachin.[39]

The function describing the potential can be written as:

$$V(x) = \begin{cases} 0, & 0 < x < L \\ \infty, & x \geq L \end{cases} \tag{2.45}$$

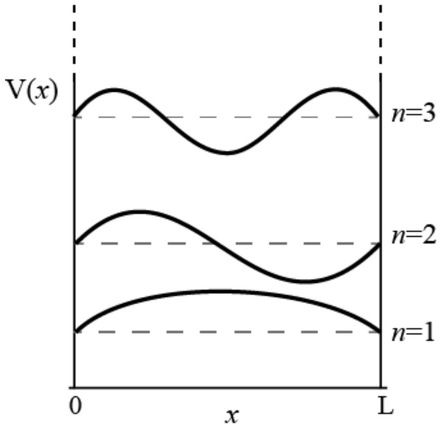

Figure 2-6 Schematic of particle in a box. *The potential* $\boldsymbol{V(x)}$ *is zero between x=0 and x=L, and infinite elsewhere. The bold lines represent the wave functions of the particle in the quantum state n.*

The time-independent Schrödinger equation of the system is:

$$-\frac{\hbar^2}{2m}\frac{d^2\psi}{d^2x} + V(x)\,\psi(x) = E\,\psi(x) \tag{2.46}$$

Inside the box the potential is zero, therefore only the first term of the Schrödinger equation needs to be considered. Furthermore the wave function at the potential edges should be continuous, a condition that is satisfied only when $\psi(a = 0) = 0$ and $\psi(a = L) = 0$. The solution is of the form $\psi(x) = \sin kx$, where the wave vector $k = n\pi/a$, from the boundary condition $\sin ka = 0 = \sin n\pi$. The wave functions of the different states are $\phi_n(x) = A_n \sin\frac{n\pi}{a}x$. The energy of the quantum states n are:

$$E_n = \frac{\hbar^2 k_n^2}{2m} = \frac{\hbar^2 \pi^2 n^2}{2mL^2} \tag{2.47}$$

Since the quantization of states comes from the boundary conditions on the wave function of the particle, the discrete energy states originate from the spatial confinement of the particle in the potential well.

The two emitters studied in this work, cyanine dyes and quantum dots, can be described and understood with the formalism of the particle in a box model. The former are naturally occurring dyes and the second are man-made nanocrystal of semiconductor material. In both of these emitters the excitation and emission energy depends on the extent of the electron confinement similarly to the one exerted by the infinite potential well.

2.2.1 Quantum dots

Quantum dots (QDs) are low dimensional semiconductor nanocrystals with a size ranging between $2-6\,nm$. Their small size localizes the motion of the electron-hole pair in all three dimensions, generating optical properties that are different from the corresponding bulk material.[2,40] Typically, bulk semiconductor materials have an energy gap between the valence and the conduction band of ~ 1 eV, corresponding to emission wavelength in the near infra-red.[41] Upon light absorption at the band-gap, an electron is promoted to the conduction band and a hole (positively charged electron vacancy) is created in the valence band. The electron-hole pair can be described by a hydrogen-like Hamiltonian:[35,36]

$$\hat{H} = -\frac{\hbar}{2m_e^*}\nabla_e^2 - \frac{\hbar}{2m_h^*}\nabla_h^2 - \frac{e^2}{\varepsilon|r_e - r_h|} \tag{2.48}$$

where ε is the dielectric constant of the material, $|r_e - r_h|$ is the distance between the electron and the hole, and their motion is characterized by the respective effective masses m_e^* and m_h^*. Since the typical Bhor radius of an electron-hole pair is ~10 nm, particles with smaller dimensions exhibit quantum mechanical properties due to quantum confinement. The properties of QDs can generally be described with the particle in the box model where the electron and hole wave functions take defined shapes, and the energy depends on the QD size as $E \propto R^{-2}$. The energy of the first state is described by a phenomenological formula that takes into account the deviations from the ideal model of particle in a box, where the energy difference between the ground and excited state depends on the extent of the confinement:

$$E_{QD}(R) = E_{BG} + \frac{\pi^2\hbar^2}{2R^2}\left(\frac{1}{m_e^*} + \frac{1}{m_h^*}\right) - 1.786\,\frac{e^2}{\varepsilon R} - 0.248\,E_{Ry}^* \tag{2.49}$$

Here, $E_{BG}$is the energy of band-gap of the semiconductor material. The second term corresponds to the quantum mechanical confinement. The third and fourth term are the coulomb potential and the Rydberg energy, respectively, which account for the attractive forces between the electron and the hole. A scheme of the resulting quantization of energy as a function of the size of the nanocrystal is illustrated in figure 2-7. Usually the energy of a QD, E_{QD}, refers to the first quantized level, and corresponds to the energy displayed by the photoluminescence (PL) spectrum. QDs absorb continuously from the first energy level to higher energies, but electron-hole pair recombination leads to the emission of a photon, which always takes place from the same energy level. This level determines the color of a colloidal solution of QDs (see figure 2-7 A).[2,40,42]

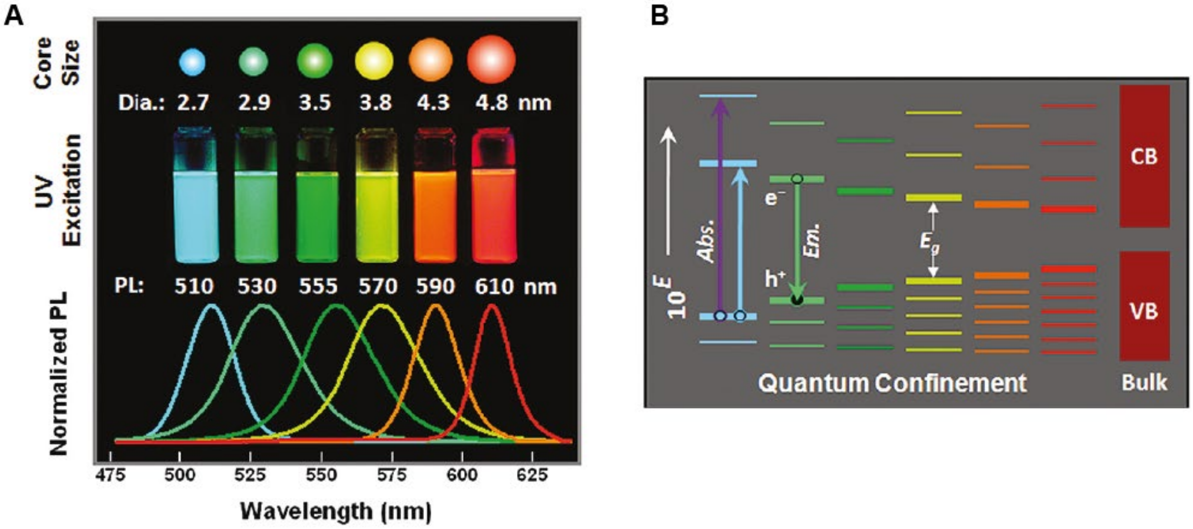

Figure 2-7 Size, color, and energy states of QDs. *(A) QDs of the same material exhibit different colors depending on their size. The color is usually defined by their PL spectrum. (B) Scheme of the energy levels for different sizes of QDs and comparison with the band gap of the corresponding material in its bulk form. Adapted with permission from Ref. 42 copyright (2011) American Chemical Society.*

Not only is the energy of the QD discrete, but its density of states is also quantized. Compared to other low-dimensional structures, such as quantum wells and quantum wires where the electrons are free to move in two or one dimension, the electrons in a QD cannot move freely in any dimension (from here the name of 0-Dimensional structures). The density of states is therefore described by the delta function, as opposed to 3-D, 2-D and 1-D structures which display a continuous density of states (see figure 2-8).[2,35,41] The physical structure of QDs can vary depending on the method of fabrication. In this work only colloidal QDs with a core/shell[43] structure are considered and their characteristics are illustrated in Chapter 5.

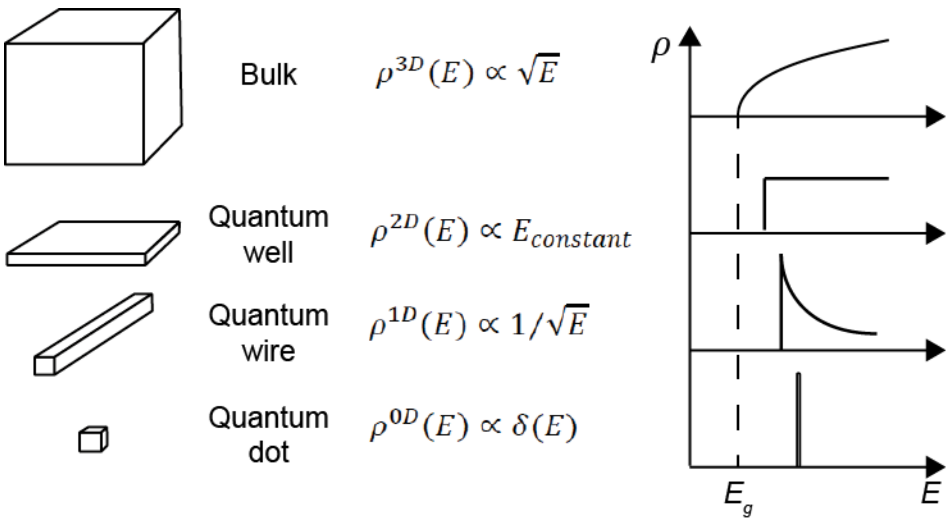

Figure 2-8 Density of states of low-dimensional materials. *Scheme of the dimensionality of materials with the corresponding nomenclature. Each low-dimensional structure has a different energy dependent density of states. The bulk, quantum well, and quantum wire structures have a continuous density of states, while the quantum dot has a discrete distribution (only the first sate is shown).*

2.2.2 Cyanine dyes

As described in section 2.1, the electronic transitions in an organic molecule occur between two molecular orbitals known as HOMO (lower energy orbital) and LUMO (higher energy orbital). These orbitals are generated by the delocalization of electrons ($\pi -$electrons) over a chain of carbon molecules with alternating double or triple carbon bonds. These electrons are spatially de-localized along the carbon chain, therefore their spatial confinement depends on the extent of the chain itself. According to the particle in a box system, as the confinement becomes stronger (smaller L) the energy separation between the ground state and the excited states of the electron becomes larger. Following the particle in a box model for organic molecules, the energy difference is:[34,44]

$$\Delta E = E_{LUMO} - E_{HOMO} = \frac{\hbar^2\pi^2}{2mL^2}\left(n_{LUMO}^2 - n_{HOMO}^2\right) \tag{2.50}$$

In a system containing $N\ \pi -$electrons, the occupied states in HOMO are $n_{HOMO} = N/2$ and in $n_{LUMO} = N/2 + 1$. Substituting the two quantum numbers in equantion 2.47 with the occupation the energy difference becomes: $\Delta E = \frac{\hbar^2\pi^2}{2mL^2}(N + 1)$.

This quantum mechanical effect is present in all conjugated systems,[44] but it is evident in the class of dyes called cyanine dyes. The basic structure is common for all of dyes of the family and it is illustrated in figure 2-9 A. It consists of a chain of carbon atoms that can be as short as three and as long as seven atoms, and is flanked on each side by two aromatic rings. The sides of the “box” which limit the extent of the π −system are the two nitrogen atoms.[44] The cyanine dyes own their specific name, for example cyanine 3 (Cy3) and cyanine 5 (Cy5) to the number of carbon atoms composing the chain. As illustrated by the example in figure 2-9 B, when the chain becomes longer, the absorption and emission of the dyes shift towards longer wavelengths, indicating a decrease of the energy difference between the ground and excited state.[45] In this case Cy3 has a maximum absorption and emission at ~550 nm and ~570 nm, while Cy5 absorption and emission are red-shifted to ~650 nm and ~670 nm, respectively.

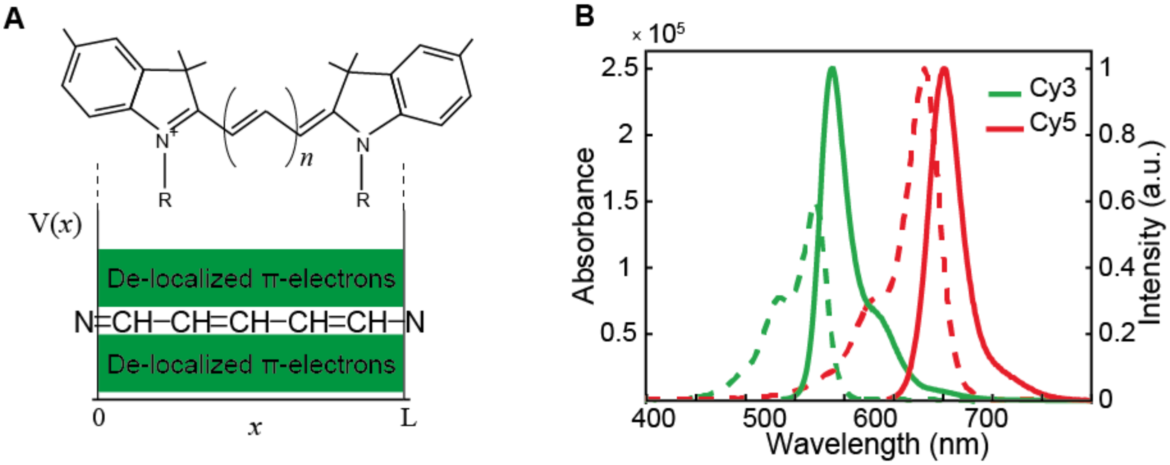

Figure 2-9 Cyanine dyes and particle in a box. *(A) Comparison of the confining potential of the particle in a box model with the CH chain of cyanine dyes confining the de-localized* $\boldsymbol{\pi}$*-electrons. (B) Example of how the energy of the HOMO-LUMO transition is shifted towards higher wavelengths when the CH chain becomes longer.*

2.3 Metal nanoparticles interaction with light

In this section the interaction between light and metals is described and the concept of plasmons is introduced from a general perspective. Subsequently the attention is focused on the interaction between light and metallic nanoparticles, in which typical dimensions are much smaller than the wavelength of the incident field. A description of localized surface plasmons is presented, followed by their applications in the field of fluorescence enhancement.

This section is based on the following books: “Plasmonics: Fundamentals and Applications” by S. A. Maier,[46] “Modern plasmonics” by N.V. Richardson and S. Holloway,[47] and “Introduction to Metal-Nanoparticle Plasmonics” by M. Pelton and G. Bryant.[48]

2.3.1 The dielectric function of metals

The response of metals to an incident electric field can be calculated from a classical perspective, using Maxwell equations in the context of the Drude model of metals. In this model, the electrons in the metal are considered as a free electron gas moving against a background of positive, fixed ions. The model assumes no interactions between ions and electrons and no long-range electron-electron interaction. The instantaneous collision between electrons is the only mechanism considered and it is described by the collision frequency $\gamma = 1/\tau$, where τ is the relaxation time of the free electron gas.

When an external electric field $\boldsymbol{E}$ is impinging upon a metal, the motion of the electron gas can be described by the equations of motion:

$$m\ddot{\boldsymbol{x}} + m\gamma\dot{\boldsymbol{x}} = -e\boldsymbol{E} \tag{2.48}$$

The electric field associated with a light beam has a harmonic time dependence $\boldsymbol{E}(t) = \boldsymbol{E}_0 e^{-i\omega t}$, therefore the motion of electrons is also in the form of $\boldsymbol{x}(t) = \boldsymbol{x}_0 e^{-i\omega t}$. Considering the polarization generated by the displacement of electrons in the metal, $\boldsymbol{P} = -\boldsymbol{nex}$ and substituting the solution for the displacement into equation 2.48, the relation between polarization of the metal and incident electric field becomes:

$$\boldsymbol{P} = -\frac{ne^2}{m(\omega^2 + i\gamma\omega)}\boldsymbol{E} \tag{2.49}$$

Now the electric displacement of charges, $\boldsymbol{D}$, can be calculated from $\boldsymbol{D} = \varepsilon_0\boldsymbol{E} + \boldsymbol{P}$:

$$\boldsymbol{D} = \varepsilon_0\left(1 - \frac{\omega_p^2}{\omega^2 + i\gamma\omega}\right)\boldsymbol{E} \tag{2.50}$$

where the plasma frequency of the free electrons is defined as $\omega_p = \sqrt{\frac{ne^2}{\varepsilon_0 m}}$. The dielectric function of metals can be extracted from equation 2.50:

$$\varepsilon(\omega) = \varepsilon_0\left(1 - \frac{\omega_p^2}{\omega^2 + i\gamma\omega}\right) \tag{2.51}$$

$\varepsilon(\omega)$ is therefore a complex function $\varepsilon(\omega) = \varepsilon_1(\omega) + i\varepsilon_2(\omega)$ where:

$$\varepsilon_1(\omega) = 1 - \frac{\omega_p^2\tau^2}{1 + \omega^2\tau^2} \tag{2.52.a}$$

$$\varepsilon_2(\omega) = \frac{\omega_p^2\tau^2}{\omega(1 + \omega^2\tau^2)} \tag{2.52.b}$$

The dielectric function describes the metal's response to an external electric field. The resulting interaction depends on the frequency of the incident field driving the electrons in the metal. If the frequency of the incident field is higher than the plasma frequency the radiation penetrates inside the metal because the charges cannot oscillate fast enough to counteract the action of the external field. On the other hand, when the frequency of the field is below the plasma frequency, the radiation is reflected by the surface of the metal. Since the plasma frequency of metals is in the UV portion of the spectrum, visible light is reflected, giving metals their typical shiny appearance.

2.3.2 Bulk plasmons

To understand the concept of plasmons and the importance of plasmon frequency, it is necessary to analyze how electromagnetic waves propagate in metals. According to the Maxwell equations, If there are no external inputs, the gradient of the charge displacement is $\nabla \cdot \boldsymbol{D} = 0$, which implies $\varepsilon(\omega)\boldsymbol{K} \cdot \boldsymbol{E} = 0$. The two possible solutions for this equation are:

$$\varepsilon(\omega) = 0 \tag{2.53.a}$$

$$\boldsymbol{K} \cdot \boldsymbol{E} = 0 \tag{2.53.b}$$

Equation 2.53.a corresponds to a longitudinal wave and it is satisfied for negligible damping ($\gamma \approx 0$) when $\omega_p = \omega$. This situation describes the collective oscillation of the conduction electrons in the metal, called bulk plasmons. It can be demonstrated that the plasmon frequency is the natural driving frequency of the oscillation of free electrons. The second solution to Maxwell's equation corresponds to the propagation of a transverse wave. This is only valid at $\omega > \omega_p$, meaning that for frequencies lower than the plasmon frequency there is no propagation of the transverse wave in the metal.

2.3.3 Localized surface plasmons

In a bulk material, plasmons are collective oscillations of electrons in a metal, generated by an external electric field of a certain frequency. When the size of the material becomes smaller than the wavelength of the exciting light, electron oscillation cannot propagate in the material due to the small size of the particle. The oscillation becomes therefore localized; hence the name localized surface plasmons. This type of plasmons can be excited by direct illumination at the resonance frequency. Typical objects that can sustain localized surface plasmons are metallic nanospheres and nanoellipsoids.

The model system considered is a nanosphere of radius R (see figure 2-10 A). When an electric field is impinging upon the NP, the electrons in the metal oscillate creating a localized accumulation of charges at its edges (see figure 2-10 B). The plasmon resonance condition can be derived using the quasi-static model if two requirements are met. Fist, the dimensions of the particle must be much smaller than the wavelength of the incident light, $R \ll \lambda$, which allows for the driving field to be considered static over the nanoparticle dimensions. Second, the electric field inside the particle mist be uniform.

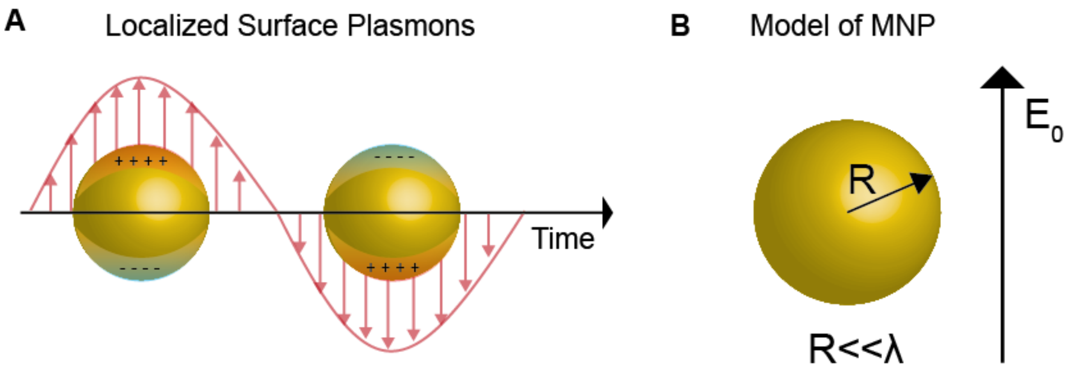

Figure 2-10 Localized surface plasmons in MNPs. *(A) Scheme of how electrons in MNPs follow the oscillation of the incident electric field. (B) Model of the MNP considered in the derivation.*

As shown in figure 2-10 A, the system under consideration is an isotropic sphere of radius R in a uniform electric field E_0. The response from the sphere is described by the dielectric function $\varepsilon(\omega)$, while the response from the medium surrounding the particle is governed by the medium dielectric function $\varepsilon_m(\omega)$. With the electrostatic approximation, the fields inside and outside the sphere can be calculated from Laplace equation of the potential $\nabla^2\Phi = 0$ and the general relation $\boldsymbol{E} = -\nabla\Phi$.

Thanks to the geometric symmetry of the problem, the electric potential inside (Φ_{in}) and outside (Φ_{out}) the sphere can be derived analytically:

$$\Phi_{in} = -\frac{3\varepsilon_m}{\varepsilon + 2\varepsilon_m} E_0 r \cos\theta \tag{2.54.a}$$

$$\Phi_{out} = -E_0 r \cos\theta + \frac{\varepsilon - \varepsilon_m}{\varepsilon + 2\varepsilon_m} E_0 R^3 \frac{\cos\theta}{r^2} \tag{2.54.b}$$

The external potential Φ_{out} can be logically divided in two terms: the first part of equation 2.54.b $-E_0 r \cos\theta$ is the external field driving the plasmons in the particle; the second part represents the field that is generated by the electrons oscillating in the particle. As illustrated in figure 2-10, when the free electrons are displaced towards one side of the particle, positive charges accumulates on the opposite side. The charge displacement process creates a polarization inside the nanoparticle. The dipole moment associated with the particle is:

$$\boldsymbol{p} = 4\pi\varepsilon_0\varepsilon_m R^3 \frac{\varepsilon - \varepsilon_m}{\varepsilon + 2\varepsilon_m} \boldsymbol{E}_0 \tag{2.55}$$

The second part of equation 2.54.b can be written as $\boldsymbol{p} \cdot \boldsymbol{r} / 4\pi\varepsilon_0\varepsilon_m r^3$, which indicates that the field generated by the charge displacement depends of the polarization of the particle. The polarizabilty of a particle (α) can be defined as the quantity that is independent from the external electric field, but is determined only by the geometry of the particle, and the dielectric functions of the metal and the surrounding medium:

$$\alpha = 4\pi R^3 \frac{\varepsilon - \varepsilon_m}{\varepsilon + 2\varepsilon_m} \tag{2.56}$$

The polarizabilty has a maximum value when $\mathrm{Re}[\varepsilon(\omega)] = -2\varepsilon_m$. This relation is called the *Fröhlich condition* and represents the dipole surface plasmon mode associated with the particle.

In the derivation presented so far, the impinging field was considered static, but in reality light is a periodically oscillating wave in the form of $\boldsymbol{E}(\boldsymbol{r}, t) = \boldsymbol{E}_0 e^{-i\omega t}$, therefore also the displacement of charges and the dipole moment oscillate with field. Due to the displacement of changes in the nanoparticle a very strong electromagnetic field is created near the surface and it is enhanced at the resonance condition:

$$\boldsymbol{E}_{near} = \frac{3\boldsymbol{n}(\boldsymbol{n} \cdot \boldsymbol{p}) - \boldsymbol{p}}{4\pi\varepsilon_0\varepsilon_m r^3} \tag{2.57}$$

Next to the electric field close to the surface of the nanoparticle, its dipole also radiates in the far-field in the form of a spherical wave, leading to scattering of the incident wave. The scattering and absorption cross-section of the particle are:

$$C_{scatt} = \frac{k^4}{6\pi}|\alpha|^2 = \frac{8\pi}{3}k^4a^6\left|\frac{\varepsilon - \varepsilon_m}{\varepsilon + 2\varepsilon_m}\right|^2 \tag{2.58.a}$$

$$C_{abs} = k\mathrm{Im}[\alpha] = 4\pi k a^3 \mathrm{Im}\left[\frac{\varepsilon - \varepsilon_m}{\varepsilon + 2\varepsilon_m}\right] \tag{2.58.b}$$

As for the electric field and polarizability, the cross sections have a maximum at the resonance dictated by the Fröhlich condition.

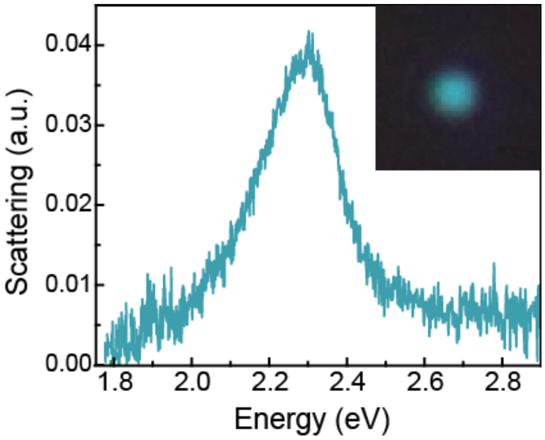

Figure 2-11 Scattering of a 60 nm AuNP. *Scattering signal of a single 60 nm AuNP acquired with a dark-field microscope.*

An example of plasmon resonance of 60 nm AuNP is presented in figure 2-11. The scattering signal of the NP was measured with a dark-field microscope. The resonance curve is very broad due to the fact that the oscillation of electrons in the particle is damped by two competing processes: a radiative decay where the plasmons decay by the emission of photons, and non-radiative decay where an electron-hole pair is created *via* absorption. These processes cause a de-phasing of the excitation, and can be described by a de-phasing time T_2. T_2has two components: T_1which is associated with the radiative and non-raditive decay, and T_2^*which is associated with elastic collisions of electrons in the metal:

$$\frac{1}{T_2} = \frac{1}{2T_1} + \frac{1}{T_2^*} \tag{2.59}$$

The de-phasing time is related to the line width of the plasmon resonance Γ:

$$\Gamma = \frac{2\hbar}{T_2} \tag{2.60}$$

It is very useful to relate the width of the plasmon to the quality factor Q of a resonant cavity:

$$Q = \frac{E_{res}}{\Gamma} \tag{2.61}$$

where $E_{res}$is the energy at the resonance. The concept of the quality factor is very important when treating the effect of the plasmonic field on quantum emitters (see section 2.3.5).

2.3.4 Plasmonic hot-spots in dimers of metallic nanoparticles

To describe the coupling between two MNPs it is useful to approximate them as point dipoles. When two dipoles interact they generate an optical response that depends on their reciprocal arrangement. If the two dipoles are arranged side-by-side they oscillate in phase, shifting the frequency of oscillation towards lower energy. In the case of two MNPs, the coupling between the oscillating electrons depends on the distance d between the spheres. If d is comparable with the NP size and larger than 1 nm, then the near field of the particles can couple.[49] The electrons of the two NPs oscillate in phase giving rise to new plasmonic modes that are different from the ones of the isolated particle. The electric field created in the gap between the particles, called the hot-spot, is enhanced by several orders of magnitude compared to the field of the single sphere.

The hybridization of plasmonic modes in dimers of NPs can be described in analogy to the hybridization of orbitals in molecules and is illustrated in figure 2-12. Depending on how the dipoles of the particles couple, four different modes can be created. Two of them are called “dark” modes because they cannot be excited by direct illumination, while the other two are called “bright” modes, since they can be excited by direct illumination. The dimer structure has two reference axes: a longitudinal axis along the direction connecting the center of the two NPs, and a transverse axis perpendicular to the dimer. If the polarization of the incident light is aligned with the longitudinal axis, the coupling of the electrons in the particles gives rise to a mode with a red-shifted resonance compared to the single NPs, but with a strong localized field in the gap, since the accumulation of charges is concentrated between the NPs. If the polarization of the exciting beam is parallel to the transverse axis, then the electrons couple along the transverse direction creating a higher energy mode.

Thanks to the plasmon hybridization, a dimer of MNPs can be seen as an antenna capable of focusing the radiation in a very small volume with the creation of a hot-spot in the gap.[22,50,51] These nanoantennas have been exploited for a variety of applications, from trapping nano-objects,[52] to improved sensing.[53,54] One of the applications of nanoantennas exploited in this work is the control of the radiative behavior of quantum emitters.[28,29,55] The physics behind the interaction between plasmons and quantum emitters is explained in detail in the next section and it is the main subject of chapter 6.

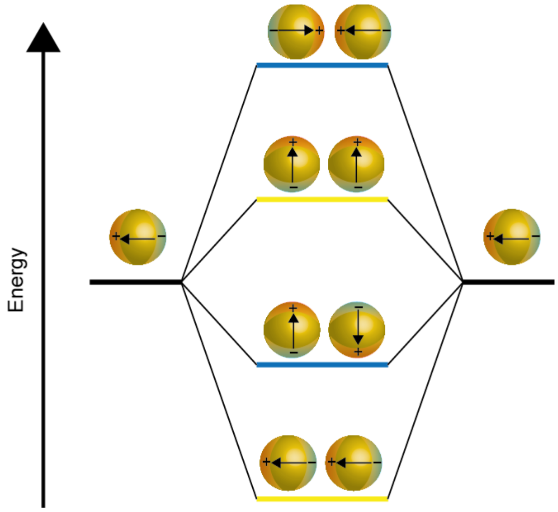

Figure 2-12 Plasmon hybridization. *Scheme of the hybridization of plasmon modes in two coupled MNPs. The states marked in yellow and blue represent the bight and the dark states, respectively.*

2.3.5 Vacuum sates and cavity effect

From a pure quantum mechanical point of view, the excited state of a quantum emitter is an eigenvalue of the Hamiltonian of the system, and it is orthogonal to the ground state. Hence the electron should not naturally decay from the excited state to the ground state. As described in section 2.14, the decay from the excited state is explained as a perturbation of the system. This perturbation depends on the transition dipole moment of the emitter and on the density of states of the environment surrounding it. Consequently the emission rate of an emitter (fluorophore or quantum dot) is not an intrinsic property, but it can be altered by changing the density of states of the surrounding electric field.

This section is based on the following books: “Quantum optics” by M. Fox[35] and “Principles of nano-optics” by L. Novotny and B. Hecht[36]

Vacuum states and spontaneous emission

In case of spontaneous emission, the molecule interacts with the states of the electromagnetic vacuum. The vacuum is a physical concept that is derived from the zero-energy point of an oscillating electric field. If we consider light from a quantum mechanical perspective, the electric field can be treated as a quantum mechanical harmonic oscillator with the Hamiltonian:

$$\widehat{H} = \frac{\hat{p}^2}{2m} + \frac{1}{2} m\omega^2 \hat{x}^2 \tag{2.62}$$

The time-independent Schrödinger equation $\widehat{H}|\psi\rangle = E|\psi\rangle$ can be solved analytically, and the energy corresponding to different quantized states is:

$$E_n = \left(n + \frac{1}{2}\right)\hbar\omega \tag{2.63}$$

From the expression of the quantized energy it is clear that at the zero-point energy of the oscillator (when $n = 0$) the energy is not zero even if no photons are excited. The energy originates from a randomly oscillating field, called the electromagnetic *vacuum field*. The magnitude of this field can be calculated by considering a cavity of volume V where the thermal energy is much smaller than the zero-point energy, $k_B T \ll \hbar\omega$. In case of visible light, $\lambda \sim 500\ nm$, for the thermal energy to be close to the vacuum energy the temperature must be $T \sim 30000\ K$. The energy of the field is

$$2 \times \int \frac{1}{2} \varepsilon_0 \mathcal{E}_{vacuum}^2 dV = \frac{1}{2}\hbar\omega \ \longrightarrow$$

$$\mathcal{E}_{vacuum} = \sqrt{\frac{\hbar\omega}{2\varepsilon_0 V}} \tag{2.64}$$

Because of Heisenberg uncertainty principle the amplitude of the vacuum field is non-zero; hence there are oscillations in the vacuum that can interact with the quantum emitter. The density of states of the vacuum can be calculated considering the same cavity with side of length L and volume $V = L^3$. The presence of the cavity has not effect on the field, but it is necessary as boundary condition for calculations. The electric field can be written as a superposition of propagating, time-dependent waves:

$$\mathcal{E}(r,t) = \sum_{\boldsymbol{k}} \mathcal{E}_{\boldsymbol{k}} e^{i(\boldsymbol{r}\cdot\boldsymbol{k} - \omega t)} = \sum_{\boldsymbol{k}} \mathcal{E}_{\boldsymbol{k}} e^{ik_x x} e^{ik_y y} e^{ik_z z} e^{-i\omega t} \tag{2.65}$$

The wave-vector $\boldsymbol{k}$ assumes discrete values according to the boundary conditions determined by the cavity of side $k_x L = 2\pi n_x$ (the same expression is valid also for y and z dimensions):

$$\boldsymbol{k} \equiv (k_x, k_y, k_z) = \frac{2\pi}{L}(n_x, n_y, n_z) \tag{2.66}$$

The number of states between $\boldsymbol{k}$ and $\boldsymbol{k} + d\boldsymbol{k}$ is given by the volume $4\pi k^2 dk$. The density of states can be derived dividing by the total volume of the k-space:

$$\rho^{3D}(k)dk = \frac{4\pi k^2}{\left(\frac{2\pi}{L}\right)^3}dk = \frac{k^2 V}{4\pi^2}dk \tag{2.67}$$

After normalization by the volume of the cavity, the general expression for the density of states becomes:

$$\rho^{3D}(k) = \frac{k^2}{4\pi^2} \tag{2.68}$$

The equation can also be written as a function of the angular frequency of the field, remembering that $\omega = ck$ and that for each frequency there are two polarizations possible $g(\omega)d\omega = 2 \times g(k)dk$:

$$\rho(\omega) = \frac{2 \times g(k)}{d\omega/_{dk}} = \frac{\omega^2}{\pi^2 c^3} \tag{2.69}$$

After calculating the energy of the vacuum field and its density of states, the rate of spontaneous emission can be derived from Fermi's golden rule, as seen in section 2.1.4:

$$\gamma_{if} = \frac{\omega^3}{3\pi\hbar c^3 \varepsilon_0}\mu_{if}^2 \tag{2.70}$$

Cavity effect and Purcell factor

As seen above, the emission rate depends on the density of states of the electromagnetic vacuum field. Logically, it follows that if the field surrounding the emitter is changed, it should affect its emission. This is the case for a quantum emitter placed in an optical cavity. Optical cavities can be described as entities where an electromagnetic field is trapped between two reflective surfaces. The electromagnetic waves in the cavity interact constructively at a certain frequency, called the resonance frequency (for more on optical cavities see "Quantum optics" by M. Fox[35] chapter 10). When an emitter is inside such a cavity, it interacts with the field (figure 2-13 emitter in cavity). This interaction can be described by three parameters:[27,56]

- The photon decay rate of the cavity, k, which is related with the width of the resonant mode of the cavity
- The non-resonant cavity decay, γ
- The atom-cavity coupling constant, g

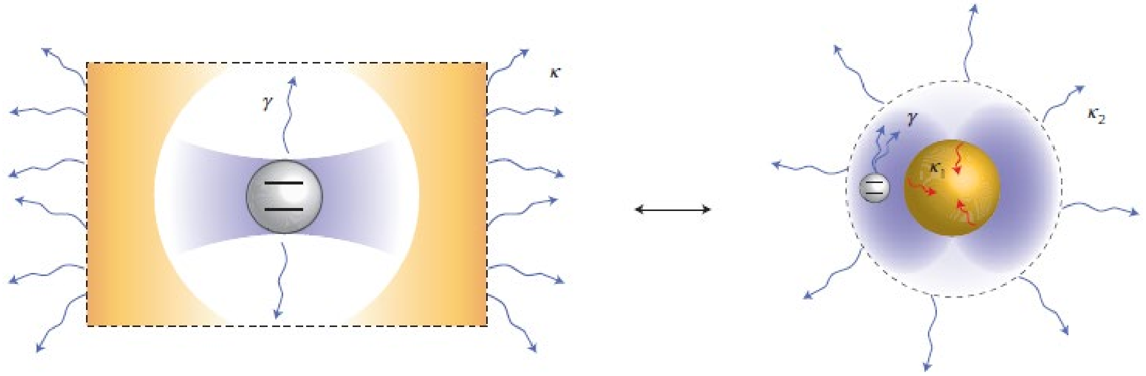

Figure 2-13 Scheme of quantum emitter-cavity interactions in the weak coupling regime. *A quantum emitter coupling to a cavity or in an analogous manner to a metallic NP is governed by* $\boldsymbol{\gamma}$*, the radiative rate of the emitter, and* $\boldsymbol{\kappa}$*, the radiative rate of the cavity. The relation of the rates and the coupling is discussed in the text. Reproduced with permission from Springer Nature, Nature Physics, from Ref. 56, copyright (2013).*

The coupling has two regimes depending on the relation between the three parameters. (i) If $g > (k, \gamma)$ the emitter-cavity photon exchange is faster than the time needed for a photon to get lost outside the cavity. Therefore, the photon can be coherently exchanged back and forth between the emitter and the cavity. This condition is known as strong coupling regime. (ii) If $g < (k, \gamma)$ the cavity and the emitter cannot exchange photons, but the radiation is lost into free space. This regime is called weak coupling. Since the emitter inside the cavity is surrounded by a different field, with a different density of states compared to the vacuum, the resulting effect is a change in the emission rate of the emitter. The focus of this section and of chapter 6 is to show how the radiation rate of the emitter can be changed by the cavity effect.

As seen in section 2.3.3 at the resonance condition MNPs can produce a very strong and confined electric field. If a quantum emitter is placed in the vicinity of a plasmonic particle, the particle acts as an optical cavity modifying the emission rate of the emitter.[57,58] The density of states of the field has a maximum at the plasmon resonance frequency. The density of states of the cavity can be expressed as a Lorenzian curve characterized by resonance frequency $\omega_c$and the full-width half maximum $\Delta\omega_c$:

$$\rho(\omega) = \frac{2}{\pi} \frac{\Delta\omega_c}{4(\omega - \omega_c)^2 + \Delta\omega_c^2} \tag{2.71}$$

The density of states has to be evaluated at the frequency of the quantum emitter ω_0. At the exact resonance condition between the emitter and the cavity, $\omega_c = \omega_0$ the density of states becomes:

$$\rho(\omega_0) = \frac{2}{\pi\Delta\omega_c} = \frac{2Q}{\pi\omega_0} \tag{2.72}$$

where $Q = \omega_c/\Delta\omega_c$ is the quality factor of the cavity. Using Fermi's golden rule, the emission rate of the emitter weakly coupled to the cavity can be calculated as:

$$\gamma_{cavity} = \frac{1}{\tau_{cavity}} = \frac{2\pi}{\hbar}\left|\boldsymbol{\mu}_{if} \cdot \mathcal{E}\right|^2 \rho(\omega) = \kappa^2 \frac{2\mu_{if}}{\varepsilon_0 \hbar}\frac{Q}{V} \tag{2.73}$$

κ^2 is the dipole orientation factor, which averages to $1/3$ when the dipole is freely rotating in space, and is equal to 1 when the dipole is oriented along the direction of the field. The change in emission rate is defined by the Purcell factor F_P, which can be calculated as the ratio between the emission rate of the emitter in the cavity and in free space. At the resonance condition, for a dipole oriented along the field the Purcell factor is:

$$F_P = \frac{\gamma_{cavity}}{\gamma_{free}} = \frac{3\lambda^3 Q}{4\pi^2 n^3 V} \tag{2.74}$$

A high enhancement of the emission rate by the cavity corresponds to a large Purcell factor. In the case of plasmonic structures the quality factor of the cavity is quite low, typically on the order of $Q = 10 - 100$. On the other hand MNPs have the ability to confine the electromagnetic field in a very small spatial region in close proximity to the surface. This field confinement gives rise to a very small mode volume, which can potentially lead to high enhancement factors.

2.4 DNA self-assembly to arrange optically active nanocomponents

The physical phenomena described so far are highly dependent upon the spatial arrangement of different components. For example FRET between two molecules is observable only if they are placed within a few nm of each other. Similarly the interaction between an emitter and a plasmonic NPs is determined by their reciprocal position and distance. This section describes how to create DNA nanostructures that can host components, such as fluorophores, QDs, and MNP, and how the properties of the DNA molecule can be exploited to achieve high spatial control over the arrangement of such components. First the physical characteristics and properties of the DNA molecule are introduced, with special attention to its spatial resolution. Then the general concepts about assembling nanostructures with DNA are explained, with a section dedicated to the DNA origami technique. The last part of this section provides an overview of the achievements in the field of photonics and plasmonics that were enabled by the DNA nanotechnology.

2.4.1 Top-down versus bottom-up

Arranging micro- and nanocomponents in a precise, custom, tailored manner is highly desirable in the field of electronics, communication technology, nano-optics and photonics. Huge progress in the semiconductor industry has been achieved in the last 40 year regarding the miniaturization of devices. Primarily the workhorse of the industry has been lithography; a top-down fabrication approach in which devices are fabricated with processes that require several steps, consisting of material deposition, pattering with masks, and progressive etching. All of these procedures require specialized labs such as clean-rooms, expensive machinery and harmful materials. Furthermore, despite the continuous push to improve the resolution of this technique, lithography has many limitations when it comes to the fabrication of features below ~10 nm.[59,60]

On the other hand bottom-up approaches, such as molecular self-assembly,[61,62] initiate the fabrication of the device from its fundamental nanocomponents, which are brought together by carefully tailoring the chemical and physical conditions of the assembly process. Moreover the assembly can be programmed by controlling specific interactions between components, for example molecular recognition, hydrophobicity and charge distribution. Among the many molecular self-assembly techniques, DNA nanotechnology has grown significantly in the past 30 years since it was originally conceptualized by Ned Seeman in 1982. In his seminal theoretical paper “Nucleic Acid Junctions and Lattices”, Seeman advanced the idea that the DNA molecule could be used to build complex, not naturally occurring 2D and 3D structures based on branched junctions of DNA strands.[63] His aim was to use such structures as a host to arrange other nanocomponents such as proteins into a crystalline lattice. In 1992, Seeman successfully built the first DNA nanostructure,[64] a cube consisting of 6 short DNA strands partially complementary to each other, which could form branched junctions in a three-dimensional manner (see figure 2-14). Since then, the field of structural DNA nanotechnology has expanded and flourished, with increasingly complex structures and lattices being made. Today, more than 200 research groups around the world mastered this technique, and use it in their everyday research.[65]

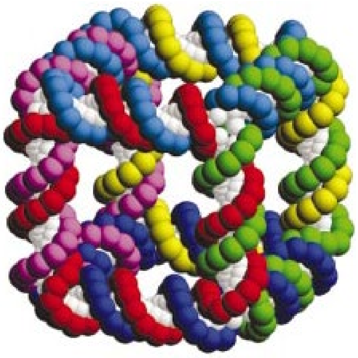

Figure 2-14 DNA cube. *First 3D DNA nanostructure artificially assembled. Each DNA single strand is colored differently. Reproduced with permission from Springer Nature, Nature, from Ref. 6, copyright (2003).*

2.4.2 The structure of the DNA molecule

The DNA molecule is formed by a chain of nucleotides consisting of three different chemical blocks covalently linked to each other: a phosphate backbone, a deoxyribose sugar, and an aromatic nucleobase (figure 2-15 A). In adjacent nucleotides, the phosphate group and the sugar are covalently linked to one another to form the DNA single strand (ss-DNA). The chain of nucleotides has a directionality, which goes from the phosphate groups of the first nucleotide, called the 5′ end, to the sugar of the last one, called the 3' end.[66,67] Two of these strands can come together *via* base-paring to form a double-stranded DNA molecule (ds-DNA), shown in figure 2-15 C. There are four different bases in a DNA strand: adenine (A) and guanine (G), classified as purines, cytosine (C) and thymine (T), classified as pyramidines (figure 2-15 B). The bases hybridize *via* hydrogen bonding in a specific manner, according to Watson-Crick base-paring,[68] where T only pairs with A, forming two bonds, and C only pairs with G, forming 3 bonds. This specificity is the basis of the molecular recognition abilities of the DNA strand. It is commonly attributed exclusively to the specific hydrogen bonding, but the molecular picture is a little more complicated. As shown by the existence of non Watson-Crick base paring, observed for example in G-quadruplexes, I-motifs, and AT-T base triples, other types of hydrogen bonding are indeed possible. Other factors such as the bases' size and the angle at which they are oriented play very important roles in maintaining the structure of ds-DNA. In fact the diameter of the molecule is determined by the two anti-parallel rails of the backbone, and this distance can be kept constant only if a small base, pyramidine, pairs with a large base, a purine. Furthermore the orientation of the bases inside the helix is fixed by the twist of the covalent bond between the sugar and the phosphate group. Since the angle of this bond is under 180°, the nucleotides are tilted inside the backbone rail. The tilt orients the bases in such a way that they can form the hydrogen bonds, and it also determines the major and minor groove of ds-DNA.[68] Since the phosphate groups on the backbone are negatively charged, the minor groove of the double strand has a high charge density. The concentration of negative charges affects the ionic conditions necessary for strand hybridization, with high relevance in structural DNA nanotechnology.

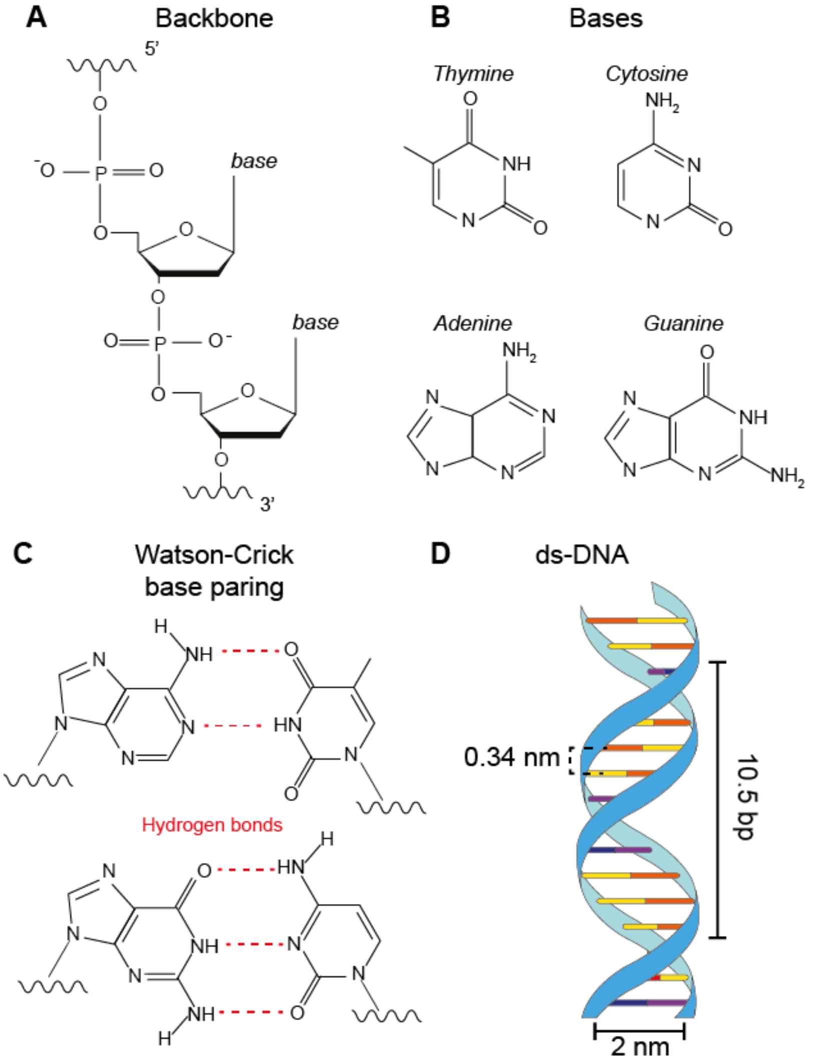

Figure 2-15 The DNA molecule. *Molecular scheme of (A) the DNA backbone consisting of the phosphate group and the sugar molecule, (B) the four DNA bases. (C) The Watson-Crick base-paring of the DNA bases, T pairs with A through two hydrogen bonds (marked in red), C pairs with G through three hydrogen bonds. (C) Scheme of the ds-DNA molecule with the indication of some of its spatial characteristics (see table 2-2).*

All of the geometrical characteristics of ds- and ss-DNA are summarized in table 2-2 and sketched in figure 2-15 D.[67] These numbers are very important when building nanostructures with DNA, because they determine the design principles, the size, and the spatial addressability of the structure, as explained later in this section.

	ds-DNA	*ss-DNA*
Pitch (nm)	3.36	
#base pairs/turn	10.5	
Base pair distance (nm)	0.336	
Persistence length (nm)	50	1.5-3

Table 2-2 Structural properties of the DNA molecule

2.4.3 Thermal stability and optical properties of DNA

As shown above, ds-DNA has a highly define structure dictated by the chemical bonds between its components. Instead the thermal stability of the double strand is affected by the interactions between bases, which are weaker than the covalent bonds. The two driving energies of the stability of ds-DNA arise from two sources: the hydrogen bonds of base-paring and the $\pi-$ stacking between adjacent base-pairs. DNA bases consist of hydrophobic aromatic rings, in which carbon atoms share electrons to form π-orbitals. When the bases are inside the DNA double helix they have a separation distance of only $0.33\ nm$, which allows the π-orbitals to overlap and give rise to stacking interaction.[69–71]

The parameter that reflects the thermal stability of the DNA molecule is the melting temperature T_m. DNA melting is the opposite process from DNA hybridization and it refers to the disassociation of the two DNA strands forming the double helix. Considering a solution of ds-DNA molecules, T_m is defined as the temperature at which half of the molecules in solution have melted into their single-stranded components. As the two forces driving the stability of the helix originate from the interaction between bases (hydrogen bonding and $\pi-$ stacking), it is evident that the melting temperature depends on both the sequence and the length of the strand. The melting temperature of a specific strand can be calculated considering the change in enthalpy, ΔH in $[cal/mol]$, and entropy, ΔS in $[cal/mol\cdot K]$, between adjacent bases according to the nearest-neighbor model:[72,73]

$$\frac{1}{T_m[K]}=\frac{R}{\Delta H}\ln C_s+\frac{(\Delta S-R\ln 4)}{\Delta H} \qquad (2.75)$$

where R is the gas constant in $[cal/mol\cdot K]$ and C_s is the strand concentration in $[mol/L]$. The stability of the DNA double helix also changes depending on solvent conditions. As mentioned above, the phosphate group on the backbone is negatively charged, and in the grooves the local density of charges increases upon DNA hybridization. The addition of salt in solution, such as sodium chloride (NaCl) or magnesium chloride ($MgCl_2$) helps the stabilization of the double helix. The positive ions can counteract the repulsive forces between the negative charges along the phosphate backbone that could prevent the formation or hinder the stability of ds-DNA. Therefore, the melting temperature increases with the addition of salt.[74]

When interacting with light the DNA molecule absorbs photons in the UV region of the spectrum, with the absorption peak at 260 nm. The absorption coefficient, $\varepsilon(\lambda)$, is different for ss- and ds-DNA due to the availability of π-stacking interaction in the double stranded form, and the lack of thereof in single stranded molecule. Due to this difference, the absorbance of the solution changes with the melting of DNA. The change can be monitored UV-Vis absorption spectroscopy and used to experimentally determine the melting temperature of a DNA strand. If the sequence, length and secondary structure of the DNA strands are known, the absorption at 260 nm can also be used to calculate the concentration of nucleic acids in the solution *via* Beer-Lambert law.[67]

2.4.4 DNA as a construction material

As described so far, DNA is a very well known biological polymer, with well defined dimensions at the nanometer (helix diameter $\sim 2nm$) and sub-nanometer (inter-base separation $\sim 0.33\ nm$) level. It can be easily dissolved and stored in aqueous solutions, and standard buffers can provide enough ionic strength for hybridization at room temperature. The double helix can be melted and re-hybridized at temperatures below the boiling point of water. Furthermore, DNA is a cost-effective material because relatively short sequences, up to a few hundreds of nucleotides, can be chemically synthesized, producing milligrams to grams of material.[65] In addition to its stability at room temperature, in its double-stranded form DNA is a stiff polymer with a persistence length of 50 nm.[6,75,76] If multiple helices are bundled together the stiffness can increase up to several hundreds of nm.[77] Last, but definitely not least, base-paring provides a molecular recognition system that makes DNA a pre-programmable material. This means that by designing the sequence the folding behavior of the polymer can be predicted. All of these characteristics make DNA a suitable material to build objects with nanometer dimensions.

2.4.5 Sticky and Branched DNA

One of the first examples of making an artificial DNA construct is represented by the technique of joining together different ds-DNA molecules for gene editing through the design of sticky ends. Sticky ends are ss-DNA sequences, usually few nucleotides in length, protruding from the double stranded portion of the molecule. These can be used to join different ds-DNA segments *via* hybridization with the complementary sequence (see figure 2-16 A). With only sticky ends in the toolbox, the ability to make complex objects with DNA is very limited, since they can only make linear ds-DNA molecules.[6,66] In 1982 Ned Seeman theorized the possibility of creating immobile and branched DNA junctions, which would allow the construction of 2D and 3D objects made of DNA. Most of his seminal work was based on a specific branched structure called Holliday junction (see figure 2-16 B). In nature, the Holliday junction is a natural branched motif occurring during the crossing-over process, where homologous chromosomes exchange part of their genetic material in germ cells. This process is fundamental for genetic recombination and for the transmission of genetic material to the next generations of a species. The Holliday junction consists of four DNA sequences that can partially hybridize to each other forming a central junction point surrounded by four ds-DNA arms. In nature, the junction is mobile due to the homology between chromosomes, but artificially it can be immobilized by sequence design.[63,78] Beyond the Holliday junction, other branched structures can be designed. The number of arms is variable but the concept is very similar: a central branched point surrounded by ds-DNA arms.

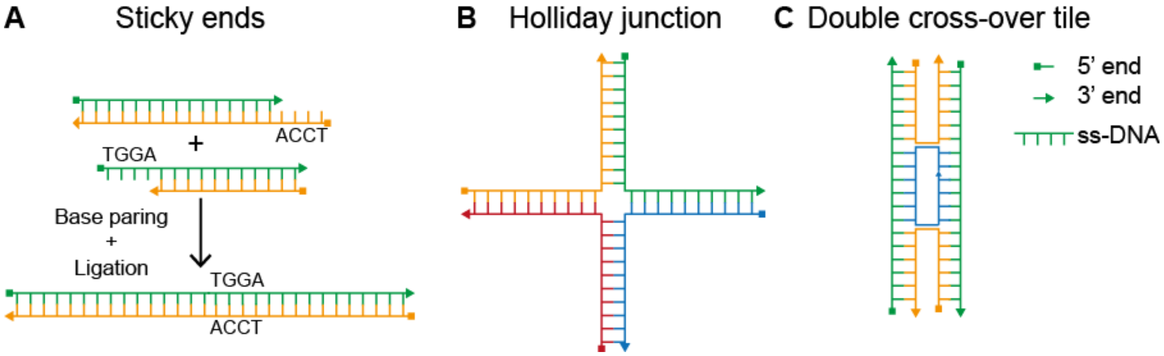

Figure 2-16 Scheme of DNA nanosctructures building blocks. *(A) Joining two ss-DNA molecules through sticky-end complementarity. (B) Holliday junction, a 4-way branching of four ss-DNA molecules partially complementary to each other. (C) DNA tile composed by five ss-DNA molecules arranged in to anti-parallel helixes. The strand marked in blue connects the two green strands through two cross-overs.*

The two basic motifs described above include one technique to make different DNA strands stick together (sticky ends) and another one to build branched DNA structures. The natural idea is to combine the two to build well-defined objects in 2D and 3D. Many structures have been built based on these principles, such as the first DNA cube[64] (figure 2-14), poyhedra and knots.[79] Despite the early success in constructing simple architectures, building larger structures and lattices, especially in 3D, with only ds-DNA frames proved difficult because of the lack of rigidity of an isolated, double-stranded DNA segment on size scales approaching its 50 nm persistence length. A new, more rigid design of DNA tiles is the double cross-over (DX), where two anti-parallel double-helices are connected to each other by two Holliday juction cross-over points.[80] As shown in figure 2-16 C, the basic tile is made of a central connecting strand (blue), that is linked twice with the external strands (green), and two other strands (orange) which have a single cross-over. This new design, combined with sticky ends, enabled the realization of bigger structures, such as large 2D arrays.[81]

2.4.6 DNA origami

A new way of assembling DNA nanostructures was introduced by Paul Rothemund in 2006, which he called DNA origami.[82] This technique is different from what illustrated so far because it is not based on DNA tiles or other small motifs being brought together by sticky ends to form the object of interest, but rather on folding a large (~7000 bases), circular ss-DNA molecule, called the scaffold, into desired shaped. A schematic of the assembly process is illustrated in figure 2-17. The scaffold molecule is held in a specific conformation by ~200 short DNA strands (15 to 50 bases long), called staples. Staples are designed to be partially complementary to different regions of the scaffold, according to the desired final shape. In the end, an origami structure consists of multiple, anti-parallel double helixes closely packed together to form a defined object made entirely of DNA, partially of viral (scaffold) and partially of synthetic origin (staples). In the design process[83] the routing of the circular single stranded scaffold is laid out to mirror the final shape of the origami object, and the staples are arranged to make the physical connections between different helixes. Similarly to the rigid DNA tiles, DNA origami utilizes the concept of the cross-over: staples traverse from one helix to the adjacent one by crossing over at specific points determined by the geometry and turns of the double helix. After the design process, the structure is folded by thermally annealing the mixture of scaffold and staples in a 1:10 ratio, *i.e.* the concentration of each staple is ten times larger than the scaffold, in a buffer solution containing typically 1 mM EDTA, 10 mM Tris and ~10 mM $MgCl_2$. The thermal annealing is necessary to enable DNA hybridization between scaffold and staples, and the magnesium is necessary for screening the charges of the negative phosphate backbone, thus allowing the DNA helixes to be packed in a close arrangement. The annealing ramp usually consists of heating the sample to 65°C to melt all the possible secondary structures of scaffold and staples, and slowly cooling down the mixture to room temperature. The precise cooling steps and the magnesium concentration must be optimized for each DNA origami structure. Typically 500 μL of solution contain $\sim 10^{12}$ folded origami structures, self-assembled in a highly parallel manner.[84] From the original 2D, flat structures[82] the field of DNA origami expanded rapidly to 3D,[85] followed by curved objects,[86] and now even arrays and crystals consisting of hundreds of origami structures.[87]

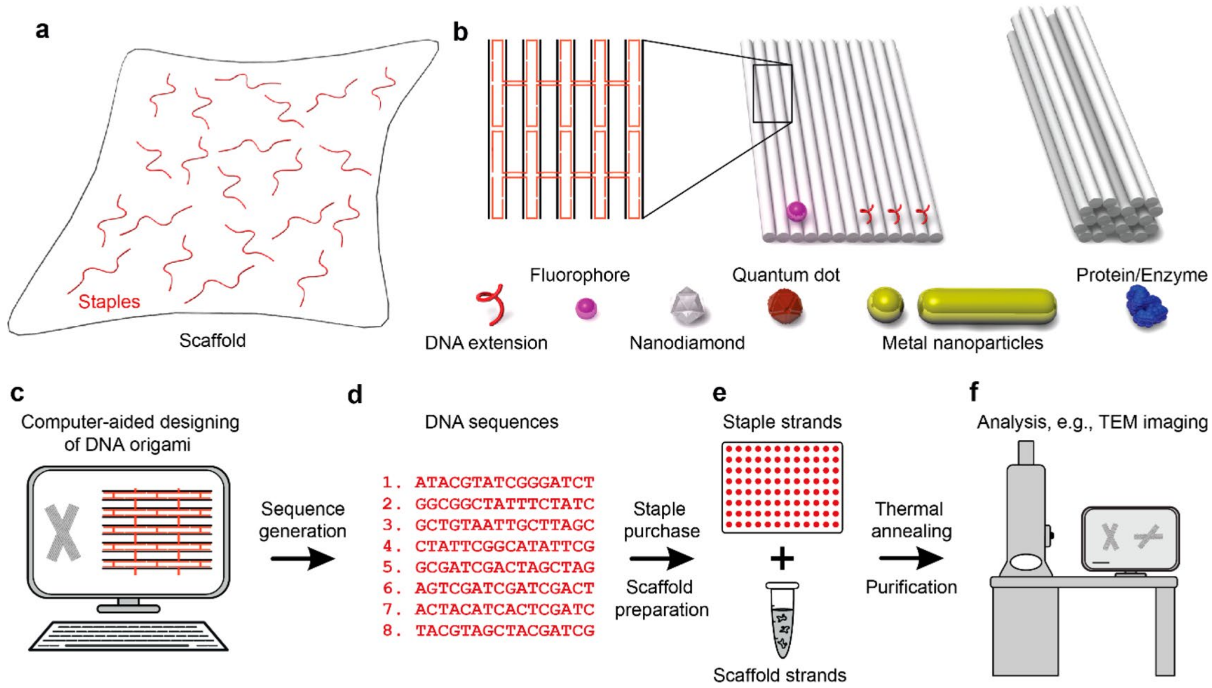

Figure 2-17 DNA origami. *(A) Components of a DNA origami structure, circular scaffold (black) and small ss-DNA staples (red). (B) Design scheme and 3D models of two DNA origami structures and possible molecules that can be integrated in the structure. (C) Design,(D) DNA sequences generation,(E) folding procedure, and (E) image analysis of a DNA origami structure. Reproduced with permission from Ref. 89 copyright (2018) American Chemical Society.*

2.4.7 Arranging nanocomponents on DNA nanostructures for photonics and plasmonics applications

The field of photonics and plasmonics deals with studying and manipulating light-matter interaction at the nanoscale. The molecules involved are usually fluorophores and nanoparticles, either made of metal or of semiconductor materials. As illustrated above, several interesting phenomena arise from the interaction of light with these components, such as energy transfer, light focusing in small hot-spots and plasmon-exciton coupling. The interactions typically occur at a distances of a few nm and result from specific arrangement of the nanocomponents, requirements that are challenging to meet for top-down fabrication approaches. On the other hand, DNA nanotechnology shows the ability to create precise nanoscale objects, which carry the addressability and the specificity of the DNA molecule. The integration of DNA nanotechnology with photonic and plasmonic components represents a great opportunity to achieve the precise spatial arrangement required to enable and finely control the phenomena of interest.[8–10,88,89]

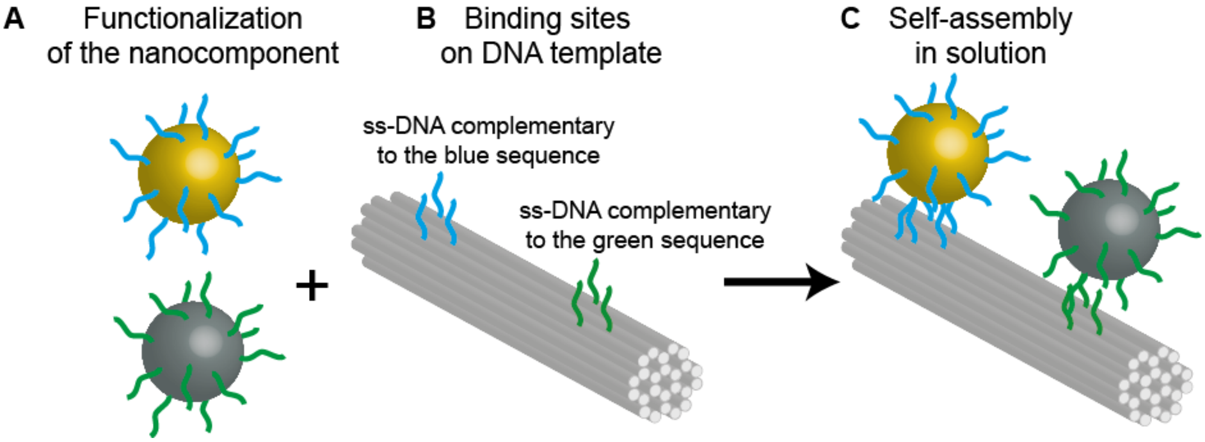

Figure 2-18 Arranging nanocomponents on DNA templates. *(A) The first requirement for integrating any nanocomponent with DNA structures is its functionalization with DNA strands. In case of NPs, the DNA stands can be linked to the surface. (B) The second step is the design of binding sites on the DNA template, which consist of ss-DNA extensions complementary to the strands on the component of interest. (C) The DNA nanostructure is mixed in solution with the functionalized components, which binds to the ss-DNA extensions.*

A DNA nanostructure, independently of its complexity, can be fully addressed with accessory molecules such as NPs and fluorophores, at the precision of a single nucleobase, because the location of each single strand and base is known *a priori*. Additionally DNA has a molecular recognition process that makes the interaction between strands very specific. Since DNA recognizes only other nucleic acids, in order to integrate any nanocomponent in a DNA structure it is necessary to link it to a DNA strand, *via* for example covalent bonding or surface functionalization. Once this requirement is met, the component can be placed virtually anywhere on the DNA template, either by direct incorporation, where the component is linked to one of the DNA oligos in the structure, or by subsequent hybridization to ss-DNA portions sticking out of the structure, called handles (see figure 2-18 for details on NPs assembly on origami). Since different components can be functionalized with, or linked to a different DNA sequence, DNA templates enable the assembly of hybrid devices, with exact composition, stoichiometry and nanometer precision, which is an unprecedented advantage over top-down fabrication methods where combining different materials and different chemical species remains challenging.[10,89]

Many photonic and plasmonic devices have been created using simple DNA complementarity, DNA tiles, and DNA origami. For example lattices of metallic NPs can be rationally programmed to assemble in 2D and 3D, either by hybridizing particles to a pre-made lattice of DNA, or by directly linking DNA-functionalized particles to each other by means of sticky ends.[88,90,91] DNA origami can be used to create complex geometries of NPs with tailored optical responses, like AuNPs helixes,[92] rings,[93] and chains.[94] Additionally dynamic devices that change spectral signature in response to an external stimulus can be fabricated.[95] In addition to metallic NPs, quantum emitters like QDs and fluorophores can also be arranged by DNA.[96] Arranging fluorophores on ds-DNA constructs to study dye-dye interaction, multi-step FRET, and energy transport in photonic wires (PWs) were some of the first application of DNA in the field of photonics.[97] Enabled by the growth of DNA nanotechnology, more complex arrangement of dyes can be realized with the aim of improving FRET efficiency,[21,98] light harvesting,[99,100] and creating excitonic circuits.[101] To incorporate the dyes in the structures, two methods are predominantly used: unspecific intercalation of the dye in the ds-DNA, or chemically linking the dye to DNA strands in the structure. Recently it has also been shown that the ability of DNA structures to localized fluorophores at very specific positions can be used for super-resolution microscopy.[101,102] Metallic NPs and quantum emitters can also be easily combined in the same nanostructure. For example on the same origami structure it is possible to arrange AuNPs, fluorophores, and QDs.[96] Using simple ds-DNA hybridization one can place fluorophores all around AuNPs[103] or in between the gap of a NP dimer.[104,105] This ability to easily combine different materials and chemical species in the same device puts DNA nanotechnology at a unique advantage point compared to other nanofabrication techniques.

3 Dye aggregation

In this chapter the phenomenon of fluorophores aggregation is discussed. First, a general description of the phenomenon of aggregation and the relevance of molecular aggregates in the context of light harvesting are presented. The system being considered in details here is the one of the simplest forms of aggregate *i.e.* a dimer. The underlying physics of exciton coupling in dimers and the resulting optical properties are briefly illustrated. The ability to create aggregates on DNA and recent work in the field will be discussed.

Part of this chapter is based on reference [20], reproduced with permission from Ref.[20] Copyright (2016) American Chemical Society

3.1 The phenomenon of dye aggregation and its importance in light harvesting

Organic dyes are mainly composed by carbon chains and aromatic rings, which are naturally hydrophobic. When dyes are in aqueous solution at low concentration they are mono-dispersed and the absorption and emission properties of the solution follow the physical description given in chapter 2. When the concentration of dyes in solution increases, or the polarity of the solvent is strengthened, the hydrophobic interaction causes dyes to stack on top of each other, leading to aggregation.[106] This phenomenon is interesting from the physical and optical point of view, because the stacking mechanism brings the molecules very close to each other (< 1 nm), and the close distance enables orbital overlap between different molecules. The overlap changes the optical properties of the ensemble, because the dyes do not display the same characteristics as their monomeric state; instead they show the creation of different energy states corresponding to the hybridized orbitals. Typically, such aggregates display a blue- or red-shift of their absorption peak along with a different emission behavior. These new properties depend on the reciprocal orientation of the monomer's dipole, controlled by the spatial arrangement of the aggregation.[107–110]

These molecular aggregates are of particular interest in the context of light harvesting. Being able to manipulate the absorption spectrum of molecules by controlling their spatial position and distance is similar to what photosynthetic organisms do. They can use exciton-exciton coupling to widen the wavelength range at which they can harvest light.[11–15,17,19,111,112] For example, Scholes and colleagues[12] calculated that the absorption band of a LHC II, composed by a dimer of Chlorophyll B850 and a monomer or Chlorophyll B800 (see figure 3-1 A), was significantly changed by considering the electronic coupling between the chromophores (see figure 3-1 B and C). Strongly-coupled, closely-spaced molecules also enable the delocalization of the exciton over the entire length of the aggregate. The delocalization is a crucial element in photosynthesis to extract electrons from the harvesting complexes, and direct them to the reaction center.[16–18,113–115] Large effort has been made to artificially control the spatial extent of the aggregate, the exact composition, and the coupling between the monomers. The aggregation of dyes can be controlled by tuning their concentration in solution, as shown for example by the first observation of a dye aggregation by Jelley.[116] Furthermore, dimerization of cyanine dyes can be partially controlled by tuning the dye concentration.[117] Other methods include the control over the ionic strength of the buffer, which promotes the hydrophobic effect driving the stacking of the dyes. [118–120] These approaches have shown the ability to form long polymer chains of molecular aggregates in solution,[121] but it is not possible to fine-tune their size and stacking dynamic. Furthermore they are limited regarding possible further integration with other nano-components.

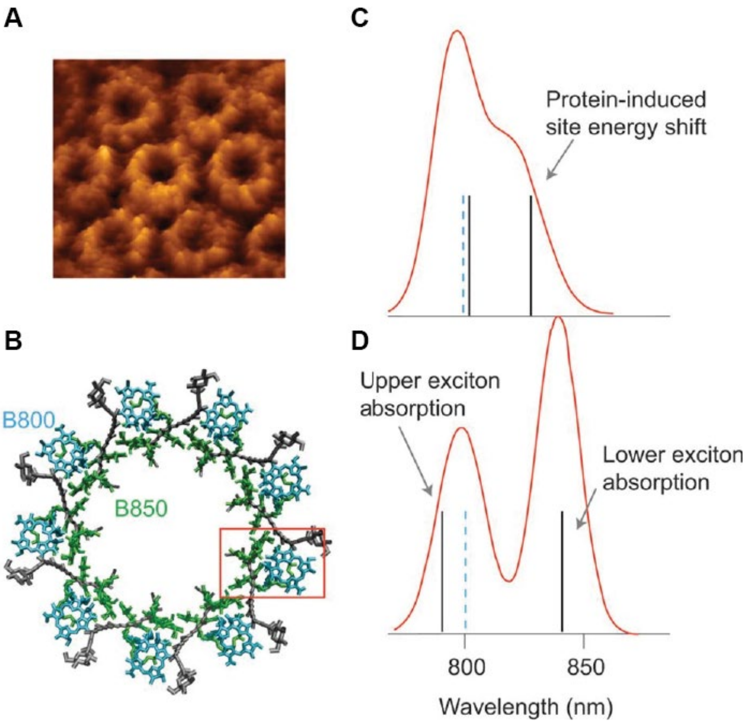

Figure 3-1 Coupling in LHCs. *(A) AFM imaging of LHCs. (B)Molecular structure and arrangements of chromophores in the LHC II of Rps. Acidophila. (C) Simulated absorption spectrum of the three dyes (two B850 and one B800) in highlighted in (B) considering no electronic coupling between the molecules. (D) Same as (C) but considering electronic coupling between the dyes. Reproduced with permission from Springer Nature, Nature Chemistry, from Ref 12, copyright (2011).*

3.2 Controlling dye aggregation with DNA

The DNA molecule is an ideal building block for the formation of aggregates of dyes with respect to control over size and interaction. Its high spatial resolution makes the DNA molecule a good candidate to achieve the necessary control over the dyes arrangement and its versatility for linking different components allows the construction of complex, optically active architectures. Due to these advantages, DNA has been in many cases the molecule of choice to arrange fluorophores to control their aggregation, exploiting both the intercalation of dyes into the groove of ds-DNA[122,123] and the chemical coupling of dyes with the DNA strand.[20,124–132] The first approach was exploited for example to induce the aggregation of cyanine dyes[122,123] and to create localized aggregates for mediating energy transfer between other fluorophores.[133–135] Even though the approach is promising, it does not allow a full control over the spatial distance and dipole arrangement between the dyes. The second approach of chemically linking the dyes to DNA truly enables full control over the number of fluorophores involved in the aggregation and their distance. There are two main approaches to linking a dye to the DNA molecule. The first requires the dye to be the "substitute" of a DNA base. In this case the dyes are fully incorporated in the DNA strand.[124,127–130,132] The second approach relies on the chemical modification of DNA bases or backbone by specific chemical groups, which can be then conjugated with the dye of interest. [20,125,126,136,137] Both methods showed the ability to enable dye-dye coupling.

3.2.1 Underlying physics of the minimal aggregate: a dimer

To describe the interaction of dye aggregates, one can consider the simplest form of aggregate, which is a dimer. The derivation in this section in manly based on Kasha *et al.*[138] Firstly, the interaction between the two monomers has to be strong enough to bring the two molecules together. Once the dimer is formed, the reciprocal arrangement and orientation of the monomers have to be taken into account to describe the aggregation type and the optical properties. Dye aggregates are classified with respect to the shift of their absorption spectrum; if the spectrum is red-shifted the dimer is called a J-aggregate, while if the spectrum is blue-shifted the dimer is called an H-aggregate. The final properties of the dimer reflect how the two monomers are arranged in space and how the angle between the dipoles is oriented. A general model for the aggregation is presented in figure 3-2 where the energy splitting of the dimer is shown. The coupling between the two molecules can be described with a combined Hamiltonian of the first molecule, H_1, the second molecule, H_2, and the interaction potential between the two monomers perturbing the system:

$$H = H_1 + H_2 + V_{12} \tag{3.1}$$

The energy of the ground state of the dimer is:

$$E^G_{dimer} = E_1 + E_2 + \iint \psi_1\psi_2 V_{12}\psi_1\psi_2 dt_1 dt_2 \tag{3.2}$$

Where E_1 and E_2 are the ground state energy of the two molecules and ψ_1 and ψ_2 their wave functions.

The energy of the excited state can be found by solving the system *via* perturbation theory and it results in (the star indicates the excited state):

$$\begin{aligned} E^*_{dimer} = E^*_1 + E_2 + \iint \psi^*_1\psi_2 V_{12}\psi^*_1\psi_2 dt_1 dt_2 \\ \mp \iint \psi^*_1\psi_2 V_{12}\psi_1\psi^*_2 dt_1 dt_2 \end{aligned} \tag{3.3}$$

The integral term of equation 3.2 and the third term of equation 3.3 correspond to the van der Waals interaction between the two monomers. To find the energy of the exciton of the molecular dimer, the difference in energy is calculated by subtracting equation 3.2, representing the ground state, from equation 3.3, representing the excited state. The resulting energy difference is:

$$\Delta E_{dimer} = \Delta E_{monomer} + \Delta D \mp \mathcal{E} \tag{3.4}$$

where ΔD is the difference in the van der Waals interaction between the ground and the excited state, and $\mathcal{E}$ is the coupling term and the origin of the energy splitting of the dimer excite state, it describes the energy interaction between the molecules. In a dipole approximation $\mathcal{E}$ can be calculated as the dipole-dipole coupling between the monomers, therefore it is clear that it depends on the angle between the transition dipoles. As illustrated in figure 3-2, the problem can be separated into two cases, one corresponding to a parallel orientation of the molecules (parallel dipole orientation), and the other one corresponding to a head-to-tail arrangement of the molecules. The description can be generalized by introducing an angular distribution of possible configurations (figure 3-2 C). The first case corresponds to a H-type of aggregation (blue shift of the absorption spectrum); the exciton of the dimer has a higher energy than the monomer. In this case the lower energy state of the dimer is transition-forbidden. The head-to-tail configuration describes the J-type of aggregation (red-shift of the absorption spectrum), the exciton of the dimer has lower energy than the monomer, and here the transition to the higher energy state is forbidden.

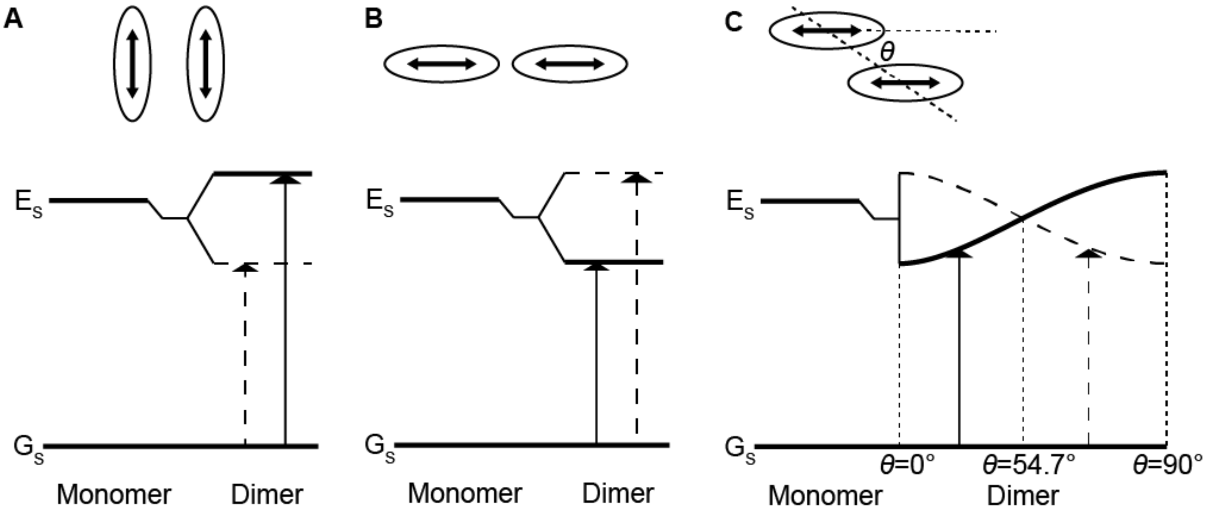

Figure 3-2 Dye dimerization scheme. *(A) Dimerization of two dyes with dipoles arranged parallel to each other. The allowed energy state (bold line) corresponds to a blue shift (higher energy) of the absorption spectrum (H-type of aggregation). (B) Dimerization of two dyes with dipoles arranged adjacent to each other. The allowed energy state (bold line) corresponds to a red shift (lower energy) of the absorption spectrum (J-type of aggregation). (C) Generalized scheme of the allowed energy level as a function of the angle between the dipoles of the dyes.*

3.2.2 H-aggregate of cyanine dyes on DNA

In this work I exploit this excellent addressability of DNA strands and in particular thymine bases to induce cyanine dye dimerization in a controlled manner and create new molecular excitonic states. With the ultimate goal of mimicking multi-dye coupling similar to that found in light harvesting complexes, here I am interested in studying interactions between pairs of Cy3 dyes brought into close proximity in synthetic DNA single- and double-strands. These DNA – dye hybrid structures are characterized by absorption spectroscopy and circular dichroism (CD).

3.2.3 Material and methods

The constructs used in this work consist of a synthetic DNA strand where one or two Cy3 molecules are linked to thymine bases through NHS coupling and the corresponding, unmodified, complementary sequence. The DNA strands were purchased from IBA GmbH (Gottingen, DE). DNA sequences can be found in appendix I.

To hybridize the modified strand with their complement, a mixture of both strands with a 1 to 1 ratio was mixed with buffer containing 1xTE (10 mM Tris, 1 mM EDTA) and 150 mM NaCl at pH 8.0. The solution was heated to 65°C for 5 min and slowly cooled to room temperature over 2h.

The absorption measurements were performed using a 10 mm optical path length quartz cuvette (Hellma-analytics) and a V-650 Spectrometer (Jasco) with 0.5 nm resolution and 1 s/point integration time. The CD signal was acquired with Chirascan-Plus Circular Dichroism Spectrometer (Applied Photo-physics Ltd) 1 nm resolution and 1 s/point integration time and the samples (DNA constructs concentration 10 μM in 1xTE and 150 mM NaCl buffer) placed in a 3 mm optical path length quartz cuvette (Hellma-analytics). Absorption and CD measurements were all performed at room temperature.

3.2.4 Absorption

The system of study is a short DNA duplex consisting of ss-DNA oligonucleotide carrying either one or two Cy3 molecules, which are covalently attached to selected thymine bases through EDC-NHS coupling and an unmodified complementary DNA sequence. I arranged the dyes in two different configurations: Dimer 1 (Cy3-G-Cy3) contains two Cy3 dyes coupled to a thymine with one unmodified guanine in between while Dimer 0 (Cy3-Cy3) has no separating base (Figure 3-B and Figure 3-C). A single labeled strand serves as a control sample (Figure 3-A).

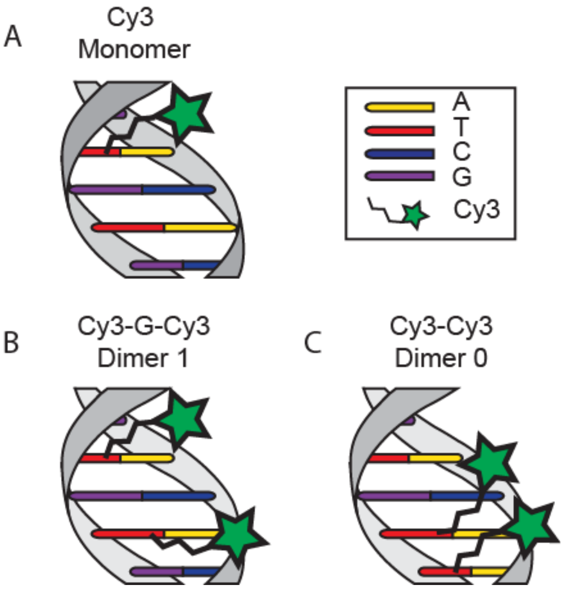

Figure 3-3 Schematic representations of experimental dye-DNA constructs with relative nomenclature and dye positions: *A) Cy3 monomer, only one thymine base is modified with the dye. B) Cy3 "dimer 1" with one base (guanine) separation between dyes. C) Cy3 "dimer 0" consisting of two Cy3 molecules linked to adjacent bases.*

To investigate the interactions between the dyes in their different configurations I performed absorption spectroscopy measurements on both the ss-DNA and the ds-DNA constructs. The results are summarized in figure 3-4. For the ss-DNA constructs (figure 3-4 A) the Cy3 monomer displays the expected absorption maximum at 550 nm with two small shoulders at 520 nm and at 480 nm (Absorption spectrum of free Cy3 is shown in figure 2-9 in Chapter 2). Constructs containing two Cy3 molecules display a new, blue-shifted peak around 512 nm (hypsochromic peak), which increases in intensity as the dyes get closer to each other. Additionally, the shoulder in the region around 480 nm becomes more pronounced in the 2-dye constructs. Similar trends are observed in the ds-DNA constructs (figure 3-4 B) but with an even more pronounced intensity increment of the blue-shifted hypsochromic peak. As the only structural difference compared to the ss-DNA constructs is the presence of the hybridized, unmodified complement, I conclude that the higher rigidity of the duplex (persistence length $P_{ds\text{-}DNA}$ ~50 nm) compared to ss-DNA ($P_{ss\text{-}DNA}$ ~1 nm) leads to a decreased orientation fluctuation of the two dyes and therefore to a modified spectrum.[76] Furthermore, the average distance between two bases in a single-stranded configuration is on the order of 6 Å while it is 3.4 Å in ds-DNA[139] also resulting in closer proximity of the dyes in the duplex configuration. The fact that the relative distance between dyes plays a crucial role in the strength of their interaction becomes obvious when comparing the increased intensity of the hypsochromic peak of the construct with 0 bases in between the dyes with that containing a spacer guanine. I attribute the formation of the hypsochromic peak to Cy3 – Cy3 interaction and not to interaction of the dyes with adjacent DNA bases, as the single-labeled control sample does not display any additional spectral peaks.

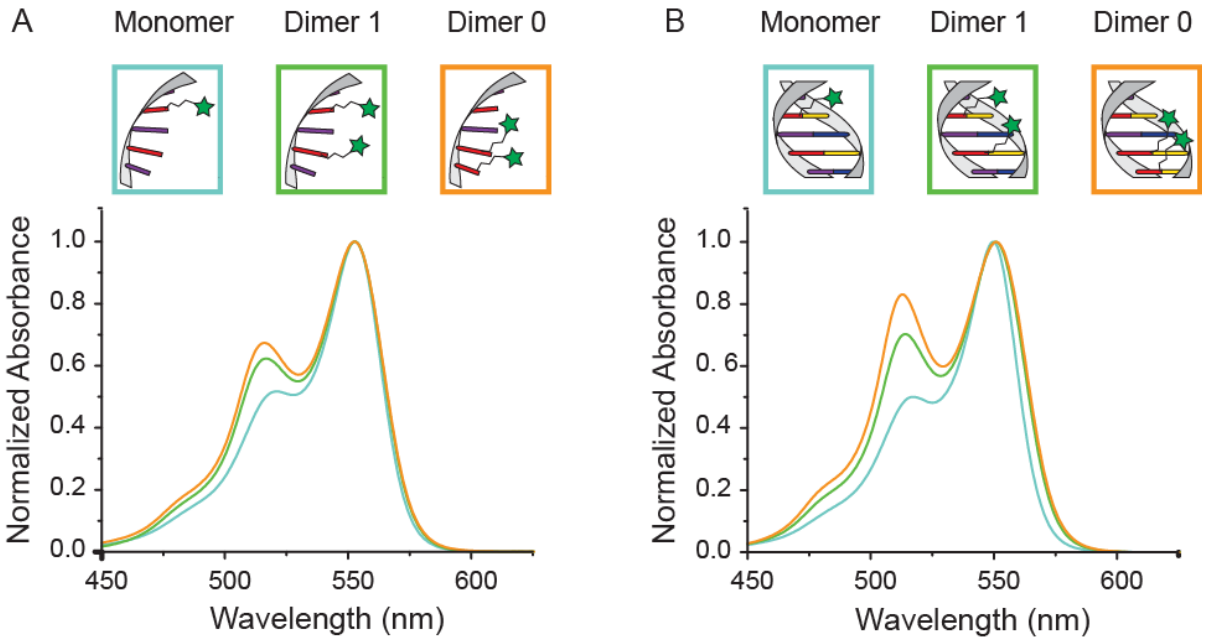

Figure 3-4 Absorption spectra of the dye-DNA constructs: *A) Normalized absorption of the ss-DNA and B) ds-DNA constructs. The light blue curves correspond to the Cy3 monomer, while the green and orange curves correspond to the Cy3 dimer with 1 base and 0 base distance respectively.*

3.2.5 Discussion and modeling

Cyanine dye molecules are known to interact with each other *via* π-orbital stacking, thereby forming H-aggregates in aqueous solutions.[120,121,140] The appearance of the blue-shifted peak in the experiments is consistent with this picture of H-aggregation of two polarized molecules with parallel dipoles.[108,109,138] To demonstrate that the dimer formation is the result of the controlled positioning of the dyes mediated by the DNA scaffold and not caused by spontaneous aggregation, I performed a series of control experiments: First, the observed spectra were not significantly affected by varying the concentration of the constructs (Figure 3-5).

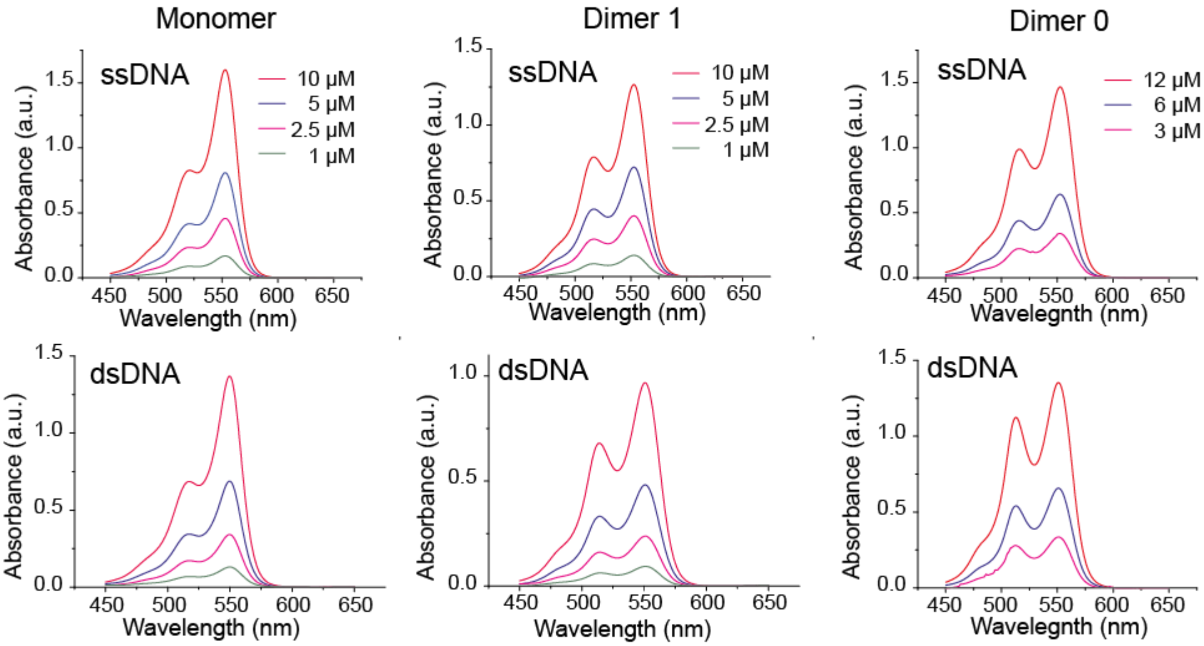

Figure 3-5 Absorbance measurements of all DNA constructs at different concentrations: *All the graphs in the upper panel, lower, refer to ss-DNA, ds-DNA, constructs respectively. The overall shape of the spectra does not change with concentration, indicating that the difference of the spectral shape is given by the type of DNA-dye construct (indicated on the top of the graphs).*

Simulated vibrational resolved absorption spectra were generated using Time-Dependent Density Functional Theory (TD-DFT) and a Polarizable Continuum Model (PCM) was applied.[141] This technique is wildly used to simulate the optical behavior of molecules by computing their spectrum. It is possible to model structures, energies, excited and vibrational states, and vertical electronic transitions. Figure 3-6 shows the simulated absorption spectrum for the strongly dipole-allowed S_1 state of the monomer and its excellent agreement with the experiments. The 0-0 band is located at 560 nm (2.61 eV) with a smaller peak at 523 nm, characteristic for cyanine dyes.[142,143] This transition corresponds to an excitation from the highest occupied molecular orbital (HOMO) to the lowest unoccupied molecular orbital (LUMO). To simulate the dimer structure two of these monomers were stacked on top of each other in a parallel dipole configuration with a distance of 3.4 Å, as by design in the “Dimer 0” construct. In this configuration, the HOMO and LUMO of the monomers combine resulting in four different orbitals and hence, four different excited states. The only transition contributing to the absorption spectrum, due to high oscillator strength, is blue-shifted towards 518 nm (2.80 eV). The resulting absorption spectrum is shown in Figure 3-6. Comparing this outcome to the monomer, I observe a blue shift of the absorption signal by 42 nm resulting from dimerization. The hypsochromic peak observed in the experimental spectrum is 38 nm shifted from the monomer absorption, which is very close to the difference displayed by the simulated spectra. The absolute simulated values of the vertical excitation of the monomer and dimer are shifted bathochromatically with respect to the experimental peaks by 0.04 and 0.03 eV, respectively, which constitutes very good agreement for an *ab initio* method such as TD-DFT.[141] This overall agreement between experimental data and theory strengthens the hypothesis of controlled H-aggregation.

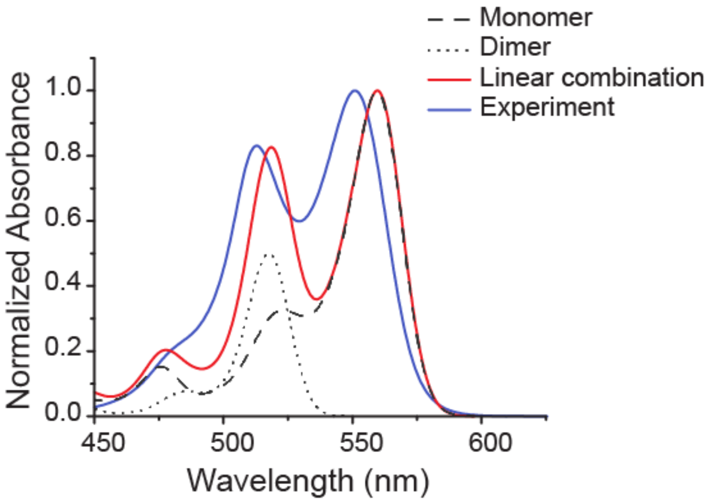

Figure 3-6 Experimental and simulated absorption: *Comparison of weighted linear combination of TD-DFT simulated spectra (solid red line) and experimentally obtained spectra from the construct "dimer 0" on ds-DNA (solid blue line). Simulated spectra of monomer and dimer are shown in black (dashed and dotted lines corresponding to monomer and dimer, respectively). The intensities of the experimental spectra were fitted best when assuming one-third of dimer and two-third of monomer contribution.* ***(TD-DFT simulations were performed by Matthias K. Ross as part of a collaborative project)***

3.2.6 Circular dichroism

In the simulations, the dyes are stacked one above the other in a parallel dipole configuration, where the energy level of the excited state corresponds to the main absorption peak of the dimer spectrum. To test for chiral arrangements of the dyes I also conducted circular dichroism (CD) measurements. All constructs containing two cyanines in close proximity exhibited a measureable CD signal (see Figure 3-7). In contrast, all samples with only a single dye did not exhibit chiral signatures, indicating that CD transfer, *i.e.* coupling between the chiral ds-DNA and the achiral individual dyes, is not the origin of the recorded CD.[144] In accordance with this observation, the Cy3 dimer with dyes in closest proximity displays the strongest CD signal. The same behavior has been reported for DNA-porphyrin constructs.[125,136] The MD simulations further confirm that the measured signal is not a result of Cy3 - DNA intercalation but a result of chiral stacking of the dyes. Generally, CD spectroscopy cannot be used to gather full structural information and additional modeling would be required to quantitatively understand the recorded spectra.[145] Nevertheless, I can infer that all the constructs showing the hypsochromic shift also exhibit chiral arrangements of dyes and that different strategies of linking the same dyes to DNA duplexes lead to structural and spectral variations.

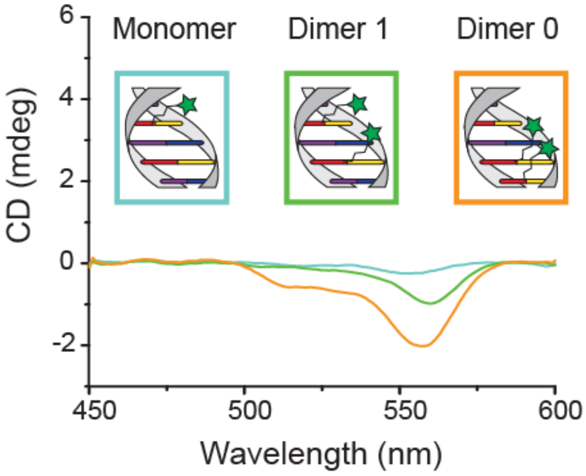

Figure 3-7 CD measurements of all ds-DNA constructs: *Spectra of Cy3-ds-DNA constructs, showing an increasing CD signal as the distance between dyes decreases*

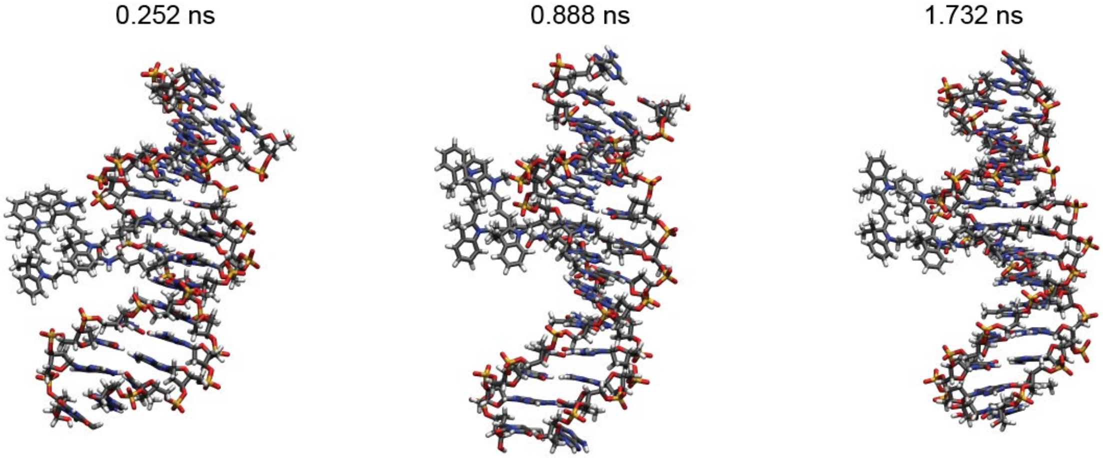

Figure 3-8 Snapshots of MD simulations at the specified time frames: *The Cy3 molecules are visible on the left and they are located, throughout the whole simulation, close to the DNA backbone. No intercalation is observed during the observation time of 2 ns. The molecules show a non-prefect parallel alignment and a fluctuating reciprocal position, which is consistent with the experimental observations of CD and the co-existence of monomer and dimer peaks.* ***(MD Simulations were performed by Matthias K. Ross as part of a collaborative project)***

Molecular dynamics simulations of the Cy3-Cy3 construct including a 14-base pair DNA sequence were used to investigate the dynamics of the system. The experimental Cy3 molecule with the original $C(CH_3)_2$ groups was considered here. Time snapshots shown in figure 3-8 reveal that the dyes stay in close proximity throughout the simulation (2 nsec). Furthermore, as the bulky $C(CH_3)_2$ groups prevent the molecule from aligning perfectly, the dye molecules rotate slightly against each other, forming an average angle of 11.1°, confirming the results of the CD spectroscopy.

3.2.7 Conclusion

In conclusion this work demonstrated that, with the relatively simple system of cyanine dyes covalently attached to DNA backbones, molecular excitonic states can artificially created by deterministically changing the reciprocal distance of the dyes and the rigidity of the scaffolding constructs. This pre-programmable DNA-based approach demonstrates excellent control over dye assembly and designed dimer interaction strengths, thus allowing optical tuning and theoretical modeling of dye aggregates. Furthermore, the use of DNA as the underlying scaffolding material opens the possibility for complex integrated nanostructures, thereby widening the toolbox of nano-optical components available for photonics and nano-optics.

4 Homo-Energy transfer studies on a DNA origami platform

In this section the concept of energy transfer is extended to multi-fluooropore systems. Multi-step FRET and homo-FRET are illustrated. The physics governing these phenomena is expanded from chapter 1, with a special focus on the case of homo-FRET. The relevance of extended energy transfer and efficient light transport is considered in the context of light harvesting. Current work on DNA nanostructures is discussed. In the last section, work on a homo-FRET mediated energy transfer chain built on a DNA origami will be presented.

Part of this chapter is based on reference [21], reproduced with permission from Ref. [21] Copyright (2017) American Chemical Society

4.1 Importance of multi-step FRET in light harvesting

Photosynthetic organisms exploit the phenomenon of energy transfer to efficiently utilize the light harvested from the sun to fuel chemical reactions. The general working principle behind photosynthesis starts with the ability of the organism to collect light. This task is performed by chromophores, typically chlorophylls and carotenoids, in LHC I and LHC II. In LHC I, chromphores surround the reaction center (RC), where all of the energy harvested from the sum is collected to perform chemical reactions that fuel the photosynthetic processes (see Figure 4-1).[11–14,18]

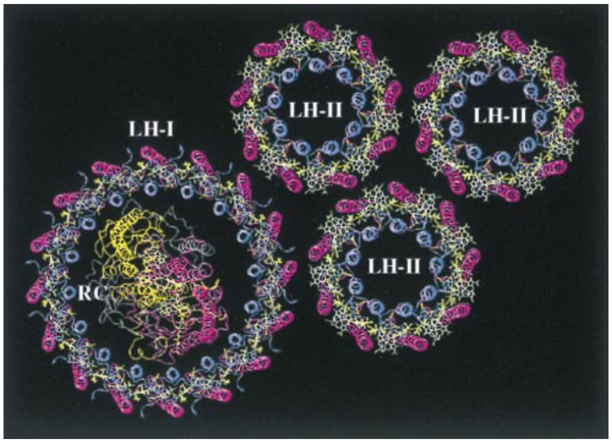

Figure 4-1 Overview of LHCs spatial arrangement. *Schematic representation of many LH II complexes surrounding one LHC I and the reaction center. Reproduced with permission from Ref. 18 copyright (1998) National Academy of Sciences, U.S.A.*

Since the amount of energy that can be processed by the reaction center is two orders of magnitude larger than what can be collected by the chromophores in the LHC I alone, other complexes, called LHC II, aid the light collection in the photosynthetic apparatus. Their only function is to collect a large number of photons and funnel them towards the LHC I and the reaction center. The energy landscape of LHCs is so that the energy can be collected over a wide spectral range and can be transferred, both between different- and same-kind chromophores (see figure 4-2 for a schematic representation of energy transfer pathways in LHCs). Furthermore, the energy can be held by certain types of chromophores before it is transferred, giving time for the accepting molecule to be freed from its exciton. Also the short distance (2 – 1 nm) between molecules in the LHC favors fast and efficient transfer.[11,14,113]

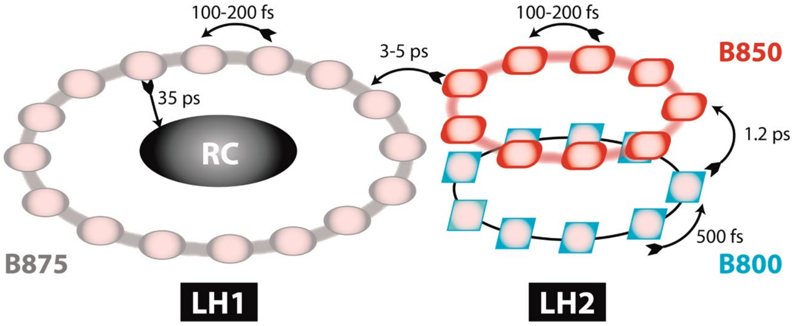

Figure 4-2 Energy transfer rates in LHCs of purple bacteria. *Scheme of the energy transfer occurring within each complex and between the LHC II and LHC I of purple bacteria. The transfer rate is different for each pair of chromophores, depending also on their distance. Reproduced with permission from Ref. 11 Copyright (2016) American Chemical Society.*

4.2 Extending energy transfer distances: multi-step hetero-FRET and homo-FRET

As illustrated in chapter 1, the phenomenon of resonance energy transfer between a donor and an acceptor molecule can occur if the conditions of resonance (*i.e.* spectral overlap), spatial separation, and dipole orientation are met by the system. Usually FRET is studied in isolated pairs of fluorophores, but is not limited to just a donor and acceptor pair. In fact, in a chain of several fluorophores the energy can take multiple steps from the primary donor (dye with the highest energy) to the final acceptor (dye with the lowest energy). If all the dyes in the chain are different, the phenomenon is called *multi-step hetero-FRET*. A scheme of hetero-FRET among three different dyes is shown in figure 4-3. Here the emission spectrum of the blue dye (alexa488) partially overlaps with the absorption of the green dye (Cy3), so the energy transfer can take place. The green dye is now excited, and since its emission overlaps with the absorption of the red dye (Cy5), the energy can take a further step and be transferred to the final acceptor. In multi-step hetero-FRET, since each fluorophore in the chain is different, the excitation can only travel from a higher to a lower energy dye, the transfer process is therefore directional. This loss of energy limits the extent of the hetero-FRET system. The transfer efficiency to the final acceptor, E_R, can be estimated multiplying the efficiency of the energy transfer from the blue to the green dye, E_{BG}, the efficiency from the green to the red dye, E_{GR}, and adding the efficiency of direct transfer from blue to red, E_{BR}, if any is present:

$$E_R = E_{BG} \times E_{GR} + E_{BR} \tag{4.1}$$

The estimation of the overall transfer efficiency can be calculated from emission because each dye has a distinct spectral range. This separation allows the selective excitation of only one of the dyes in the chain, and the distinction of the emission coming from different dyes. Both characteristics carry important information regarding the transfer efficiency among the chain.

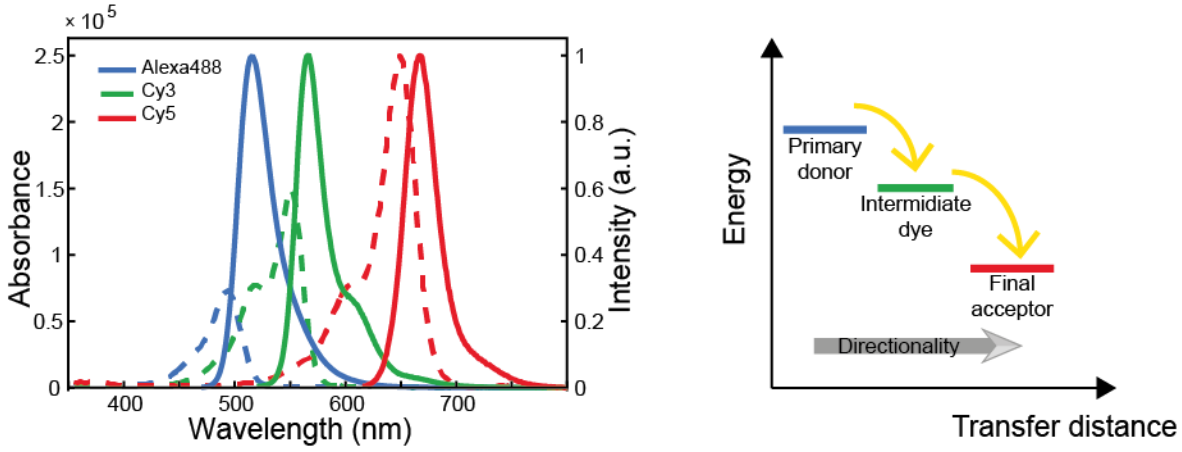

Figure 4-3 Multi-step hetero-FRET. *(A) Spectral overlap of three dyes (Alexa488, Cy3, and Cy5) constructing the FRET cascade. Full lines represent the emission spectra and dashed lines represent the absorption spectra. (B) Schematic representation of the energy cascade and the directionality of the transfer when the energy goes from the blue to the red dye.*

In the case of a system containing multiple fluorophores of the same kind the energy can still be transferred among the dyes if they fulfill the resonance requirement. The phenomenon is called *homo-FRET* and it is allowed in fluorophores that display a small Stoke-shift, which means the emission and absorption spectra have a significant overlap. A schematic representation of homo-FRET is shown in figure 4-4. Since all dyes have the same energy, the excitation can travel to any component of the chain. Opposed to hetero-FRET, homo-FRET is a not a unidirectional process and it is not limited to a certain number of fluorophores. Additionally because there is no spectral distinction in the chain, selective excitation and detection are impossible, which means that at any dye of the chain could be excited, transfer energy to any other dye and when photons are emitted it cannot be established from which fluorophore they originated. To describe the excitation rate of a dye n, which is part of the homo-FRET system consisting of m dyes, the direct excitation of the fluorophore, $\varepsilon_n(\lambda_{ex})L(t)$, and the unbiased transfer to any other dye have to be considered:

$$\frac{dI_n}{dt} = \varepsilon_n(\lambda_{ex})L(t) + \sum_{i\neq n}^{m} k_{in}I_i - (k_n + k_{ni})I_n \tag{4.2}$$

Where k_{in} is the transfer rate from florophore i to fluorophore n (k_{ni} vice versa) and I is the integrated excited state life time of the fluorophore. For the reason of indistinguishable transfer and emission conventional measurements methods that focus on recording radiative emission alone cannot give meaningful information about the system.

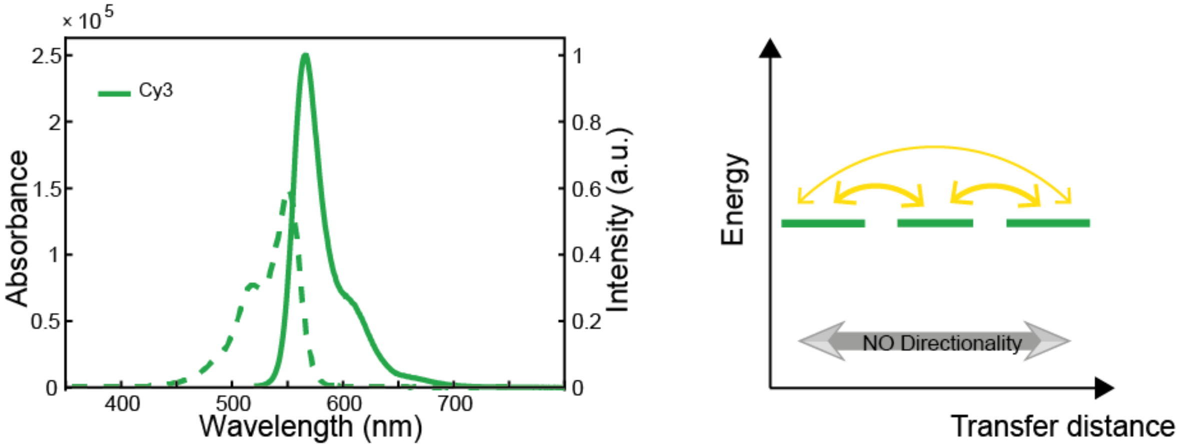

Figure 4-4 Homo-FRET scheme. *(A) Spectral overlap, given by a small Stoke shift, of the dye (Cy3) undergoing homo-FRET. Full lines represent the emission spectrum and dashed lines represent the absorption spectrum. (B) Schematic representation of the energy delocalization in a chain of homo-FRET dyes.*

One technique that provides insights in the homo-FRET phenomenon is fluorescence anisotropy, which records the polarization of the emitted photons. Each time fluorophores are excited by a polarized beam they re-emit photons with a different polarization, depending on their orientation in solution. The polarization of the emitted photons can be determined by measuring the emission with two polarizers perpendicular to each other:

$$A = \frac{I_{\parallel} - I_{\perp}}{I_{\parallel} + 2I_{\perp}} \tag{4.3}$$

where A is the anisotropy, $I_{\parallel}$ and $I_{\perp}$ are the measured parallel and perpendicular intensities for which the direction is defined by the polarization of the exciting beam. When fluorophores are randomly oriented and not interacting, their average anisotropy value is 0.4. FRET causes a depolarization of the emission and therefore a decrease in anisotropy. When fluorophores undergo FRET, part of their energy is emitted by the donor and part by the acceptor, each of which haave a different orientation. Given the wide angles of relative donor/acceptor orientations allowed, the resulting emitted photons show a decrease in polarization. In the case of homo-FRET the more steps the energy takes *i.e.* the larger is the extent of the system, the higher the decreases in the polarization of emitted photons will be.

4.3 DNA nanostructures to mediate multi-step FRET and mimic light harvesting

A clear take-home message from both FRET theory and LHCs is that spatial organization of chromophores is important for directing the energy transfer and controlling its efficiency. Having scaffolding molecules where the arrangement of fluorophores can be controlled can enable the construction of artificial light harvesting devices inspired by photosynthetic organisms and the realization of photonic wires that can transport energy at the nanoscale. Since the length scale involved in energy transfer is on the order of ~nm, scaffolding molecules such as proteins and DNA can provide the necessary spatial resolution to construct these devices. In this respect, DNA has been the material of choice in many cases, due to the ease of chemically linking it to fluorophores and the possibility of controlling the shape of the nanostructures extremely well. Extensive work has been carried out using small structures assembled from individual synthetic DNA oligos. Photonic wires consisting of multiple fluorophores have been built on ds-DNA,[135,146–148] as well as on more complicated branched structures.[133,134,149] Such wires usually consist of different fluorophores that can perform multi-step hetero-FRET (see figure 4-5), and their spectra range goes from blue (~450 nm) to the near infra-red (~700 nm).

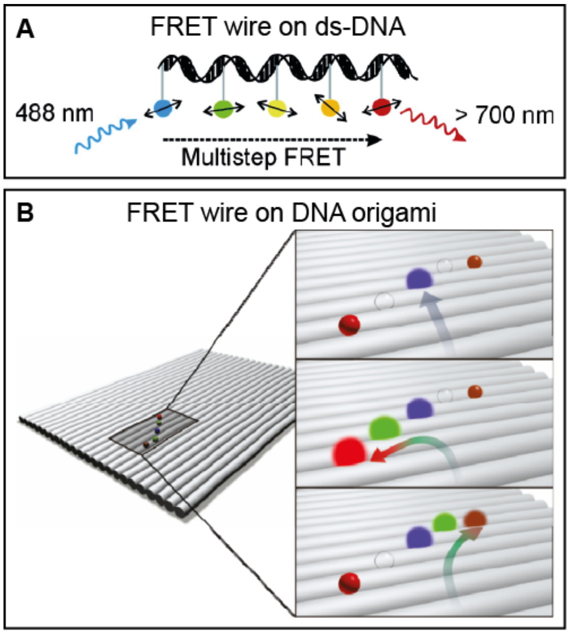

Figure 4-5 Multi-step FRET wires on DNA nanostructures. *(A) Wire constructed on ds-DNA. Adapted with permission from Ref. 146 copyright (2004) American Chemical Society. (B) Wire constructed on a DNA origami sheet. Adapted with permission from Ref. 150 copyright (2011) American Chemical Society.*

Branched DNA assemblies have been exploited to more closely imitate the structure of natural LHCs (see figure 4-6). In these systems, multiple fluorophores are arranged in a circular fashion around a centrally located final acceptor, to where all the collected energy is funneled. This behavior is related to the collection ability of antennas, so their performance regarding light funneling is usually determined by the "antenna effect". This quantity compares the emission of the final acceptor beings directly excited to its emission arising from the energy transferred by the surrounding fluorphores. In addition to the work done on small DNA constructs, similar achievements were obtained on DNA origami platforms.[99,100,150,151] The use of DNA origami has many advantages, for example the nanostructures are more rigid allowing a more precise placement of fluorophores, they are modular by design, meaning that each molecule can be linked to a different DNA staple strand, and they can be easily purified from the excess of fluorophores and misfolded structures. These two last characteristics are very important because they allow the complexity of the FRET cascade to be broken down in its fundamental components, and precisely analyzed thanks to high purity.

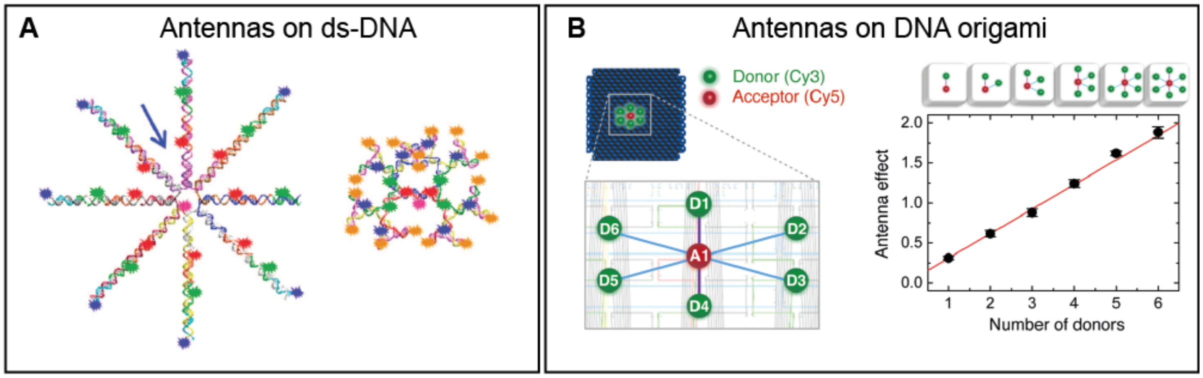

Figure 4-6 Circular arrangements of dyes surrounding a central acceptor imitating the structure of natural LHCs. *Assembly built on (A) ds-DNA nanostructures and (B) a DNA origami sheet. (A) Adapted with permission from Ref. 149 under Creative Common Attribution international license (2014). (B) Adapted with permission from Ref. 100 under Creative Common Attribution international license (2016).*

Similarly to LHCs, these systems artificially assembled by DNA can indeed spatially organized fluorpohores in a precise manner, which controls the light collection capabilities of the device. One of their main limitations is that the energy cascade can only extend to few tens of nm, because it relies on a large variety of fluorophores that caused a decrease in energy every transfer step. On the contrary, natural LHCs contain very few different molecules, typically two types of chlorophyll and carotenoids spread over larger areas. Despite the low variety of chromophores, and the spatial spread, photosynthetic organisms can still achieve very high light collection efficiency. As illustrated above, the energy can be transferred from all the LHCs II surrounding the LCH I in such an efficient manner because in chromophores the energy cannot only be funneled to lower energy state, but also can also be shared among equal energy molecules.[11,14,15] This process is very similar to what is described by the concept of homo-FRET illustrated in the previous section.

Inspired by natural LHCs, homo-FRET started to be incorporated in DNA-based photonic wires and antenna-mimicking arrangements. In the former structures, the chain of homo-FRET dyes is used mainly to extend the length of the wire,[98] while in the latter, homo-FRET is used to limit the energy lost in the transfer.[152] These studies involving homo-FRET chains are carried out on simple DNA nanostructures, which limit the ability of de-convolving the contribution of single dyes to the overall transfer. As discussed in the previous paragraph, homo-FRET is per se very difficult to study due to lack of directionality and selectivity. To this aim the modularity of DNA origami structures can be extensively exploited to shine light in the phenomenon of homo-FRET and on its effect in fluorophores assemblies.

4.4 DNA origami for homo-FRET studies

In this work I present a comprehensive study of the homo-FRET phenomenon on a DNA origami structure. I assembled a combination of a three-color cascade and a homo-FRET-based photonic wire (PW), achieving energy transfer over a distance of 16 nm from a blue donor dye to a red acceptor dye through three green fluorophores. The main focus of the study is on the effects of homo-FRET on the overall energy transfer. Specifically, by breaking down the complex dye cascade into its individual components and by systematically analyzing the partial contributions of each dye to the system, I show that the overall energy migration is enhanced by homo-FRET between the donors, as compared to expected transfer efficiency in the absence of homo-FRET. I carried out bulk fluorescence spectroscopy experiments to measure the FRET efficiency. To obtain a consistent picture of the energy transfer processes, my results are supported by single-molecule (SM) experiments and Monte Carlo (MC) simulations performed within the collaboration of the project.

4.4.1 Material and methods

Dyes and DNA origami - The DNA origami structure used in these experiments is a square lattice 3-layer, brick-like structure (for origami design, DNA sequences and folding conditions see appendix II). The dyes were incorporated into the DNA structure during folding by adding the desired dye-labeled DNA strands in the mixture of ss-DNA scaffold, staples and buffer. All the samples were purified with PEG precipitation [153,154] before performing fluorescence measurements.

The dye functionalized DNA strands were purchased from IBA GmbH, Göttingen, Germany. Both internal (on thymine base) and terminal (on 5’-end) functionalizations were carried out through NHS ester coupling. For details on dye-labeled DNA strands see appendix II.

Bulk fluorescence spectroscopy - Bulk fluorescence measurements were carried out with a modular spectrofluorometer Fluorolog®3, Horiba scientific. For the measurements, the sample was transferred into a cuvette 2x10mm optical path (Hellma Analytics). The samples consist of 100 uL of 10 nM DNA origami carrying different dyes combinations in a buffer solution (10 mM Tris, 1 mM EDTA and 20 mM $MgCl_2$).

Each construct was independently assembled and measured at least six times. Fluorescence emission spectra were recorded and the FRET efficiency calculated from the relative intensities of the donor and acceptor fluorescence. To avoid direct excitation of Cy5, Cy3 was excited at 520 nm instead of its absorbance maximum at 555 nm. The emission spectra were normalized with respect to the Cy5 emission after excitation at 640 nm in order to correct for different sample concentrations.

4.4.2 Homo-FRET Wires on DNA Origami

A schematic drawing of the DNA-origami supported PW is shown in Figure 1 A. The full PW consists of five dyes: one blue donor (Alexa488) with the highest excitation and emission energies, three green dyes (Cy3) of intermediate energies, and one acceptor (Cy5) exhibiting the lowest energies. The dyes are positioned in a quasi-linear arrangement on the upper surface of a three-layered DNA origami block, resembling a 1D-wire. The different labeling positions for Cy3 are indicated with a "G_1", "G_2" or "G_3" when the respective dye is present, while an "X" indicates the absence of any dye in that position (see table 4-1 for the complete list of all constructs). As the blue and red fluorophore are separated by 16 ± 0.6 nm (the distances and corresponding errors are based on the well-known structure of DNA origami objects[155,156] and the flexibility of the linker molecule), energy absorbed from the blue donor to the red acceptor must travel through a multi-step energy transfer process *via* one or more intermediate green dyes. Of the multiple possible energy pathways, the most important ones are shown in Figure 1 B.

Green to Red FRET Constructs	Name	Blue to Red FRET Constructs	Name
★☆☆ ★	G_1XXR	★ ★☆☆ ★	BG_1XXR
☆★☆ ★	XG_2XR	★ ☆★☆ ★	BXG_2XR
☆☆★ ★	XXG_3R	★ ☆☆★ ★	$BXXG_3R$
☆★★ ★	XG_2G_3R	★ ☆★★ ★	BXG_2G_3R
★☆★ ★	G_1XG_3R	★ ★☆★ ★	BG_1XG_3R
★★☆ ★	G_1G_2XR	★ ★★☆ ★	BG_1G_2XR
★★★ ★	$G_1G_2G_3R$	★ ★★★ ★	$BG_1G_2G_3R$

Table 4-1 Nomenclature of all FRET constructs

The spectral characteristics of the dyes are illustrated in figure 4-3 and their FRET properties are summarized in table 4-2. The quantum yield (QY) values reported in Table 4-2 are taken from the referenced literature, while the overlap integral $J(\lambda)$ is calculated according to the measured absorption and emission spectra in figure 4-3. The corresponding Förster radius is then calculated from equation 2.42. For the homo-FRET system, I determined a Förster radius of 4.6 nm, resulting in expected transfer efficiencies in an isolated system of 90% (G_2G_3), 50% (G_1G_2) and 27% (G_1G_3) between Cy3s in the PW. The dipole-dipole interaction regime was assumed, as the minimum separation between the fluorophores is larger than 3 nm.

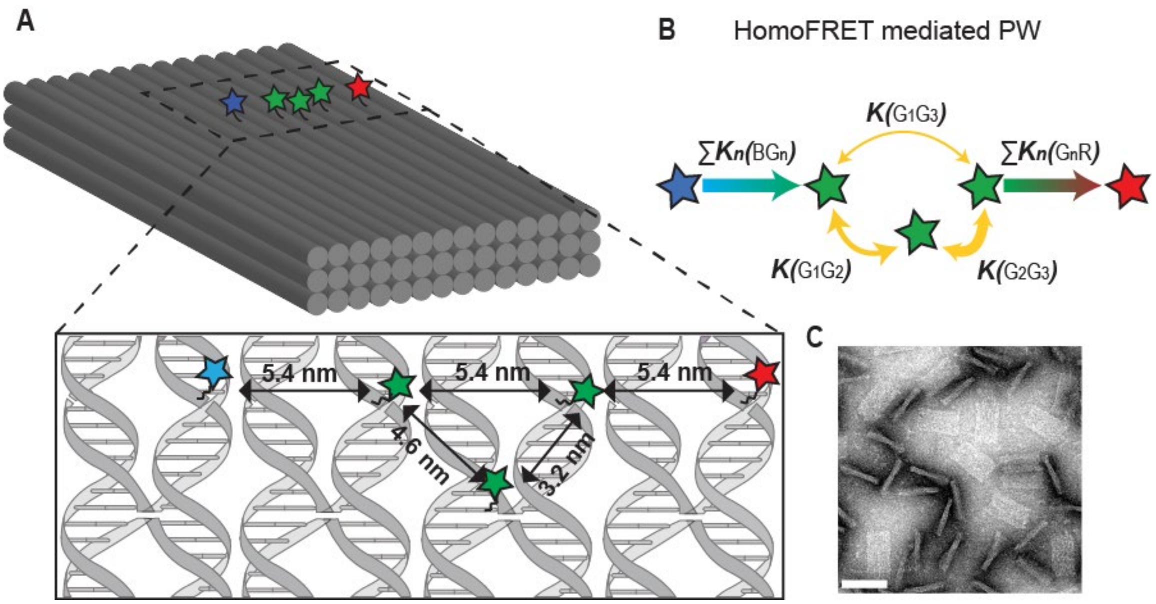

Figure 4-7 Homo-FRET-mediated photonic wire. *(A) Schematic representation of the three-layered DNA origami block. (B) Possible energy pathways of the photonic wire and their corresponding transfer rates. The thickness of the yellow arrows is proportional to the calculated efficiency of the homo-FRET between the two green dyes. (C) TEM image of origami blocks, some of which are lying flat and others standing on their sides (scale bar: 80 nm). In the enlarged region, the scheme indicates the designed locations of the dye molecules with respect to the DNA strands.*

To estimate the dye-dye distance on the DNA origami structure, inter-helical distance was assumed to be of 2.7 nm, as taken from Fischer *et al*[156] where the same DNA structure used in this work was measured by means of SAXS (small angle x-ray scattering). The error arising from those measurements is of the order of 0.02 Å, so the main source of error here is assumed to be the fluctuations of the dyes on the DNA origami. All the fluorophores are linked to the DNA *via* NHS-Ester coupling *via* a 6-Carbon chain with an estimated length of about ~0.4 nm.[157] Therefore, I calculate the dye-dye distance error to be $\sigma_d = \sqrt{2 * 0.4^2}\ \text{nm} = 0.57\ \text{nm}$

FRET pair	Overlap Integral J ($nm^4/(M\ cm)$)	R_0 (nm)	Donor QY
Alexa488-Cy3	$6.60x10^{15}$	6.9	0.9[158]
Cy3-Cy3	$3.71\ x10^{15}$	4.7	0.15[159,160]
Cy3-Cy5	$7.86\ x10^{15}$	5.3	0.15[159,160]

Table 4-2 Spectral properties of FRET pairs. *The overlap integral and R_0 are calculated from spectra in figure 4-3, for quantum yield values refer to the cited literature.*

4.4.3 Ensemble FRET Experiments.

I first investigate the system with a single acceptor dye and no blue dye, a condition inspired by the energy migration in the LHC from multiple donors to a single acceptor acting as an energy sink, meaning that the chromophore actively depletes the system. To determine the overall energy transfer in this system, I measured bulk fluorescence emission spectra after excitation of the Cy3 fluorophores. Figure 2 shows the spectrum of the construct $G_1G_2G_3R$ with the three homo-FRET green dyes and the red acceptor and the corresponding assembly without acceptor. Clearly the former spectrum exhibits two emission peaks, one from Cy3 around 560 nm and the second one from Cy5 around 660 nm, indicating the occurrence of FRET, while for the latter construct no red emission is detected. To assess the amount of the direct excitation of Cy5 upon 520 nm incident light, I performed a control where the fluorescently labeled DNA staples were mixed in a 3 to 1 ratio corresponding to the three green and the one red staple and measured the resulting emission spectrum. The distance between Cy3 and Cy5 in solution is large and does not allow energy transfer between the green and red dyes. Hence, the emission spectrum gives an estimation of the direct excitation of Cy5 after Cy3 excitation when no FRET occurs. A negligible amount of red fluorescence is detected (see inset in Figure 2). Furthermore, the absorption of Cy5 at 520 nm is estimated to be less than $0.02\varepsilon_{cy5}$, where ε_{cy5} is the extinction coefficient of the dye (see figure 4-3 dashed red line).

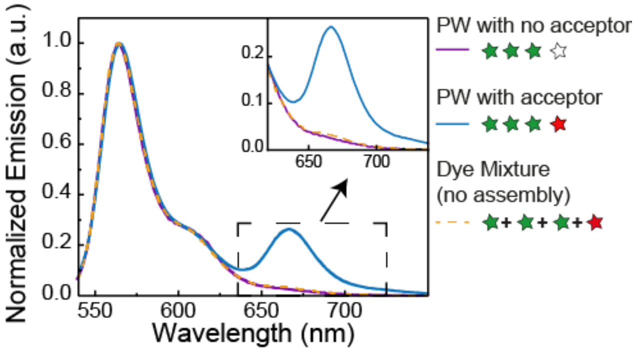

Figure 4-8 FRET vs. non-FRET emission spectra. *Bulk emission spectra of the homo-FRET photonic wire with (blue line) and without (purple line) acceptor dye and the mixture of Cy3/Cy5 labeled DNA staples, which constitute the photonic wire (orange dashed line), upon 520 nm incident light.*

To investigate the effect of homo-FRET on the energy transfer, I measured the emission from the single Cy3/Cy5 hetero-FRET pairs (G_1XXR, XG_2XR and XXG_3R) and compared $G_1G_2G_3R$. This assembly shows a significant increase in Cy5 fluorescence compared to the constructs with only one donor. The measured increase in absolute fluorescence is expected in hetero-FRET systems from the contribution of multiple donors.[99,100] To quantify the contribution of multiple donor dyes on the energy transfer, I compared the sum of the individual Cy3/Cy5 pairs to the full construct (Figure 3 A grey spectrum). Overall, I found that this energy delocalization results in a small increase of Cy5 emission compared to the sum of the single contributions of G_1, G_2 and G_3. When calculating the corresponding energy transfer efficiency, I find that the three-donor construct leads to an increase of $\Delta E = 0.01$, compared to the averaged contribution of single hetero-FRET pairs. This increase corresponds to an enhancement of 7.5% (see Table 4-3). Due to heterogeneity of samples this increase falls within variability, but it is consistently present in every sample batch measured. It should be noted that while $G_1G_2G_3R$ has an overall lower FRET efficiency than XXG_3R due to the increasingly larger distance between the additional donors G_1 and G_2 from the acceptor, the overall transfer to the acceptor is enhanced as is evident from the increased Cy5 emission.

	G_1XXR	***XG_2XR***	***XXG_3R***	***G_1G_2XR***	***G_1XG_3R***	***XG_2G_3R***	***$G_1G_2G_3R$***
E_{Bulk}	0.05 ±0.004	0.12 ±0.009	0.36 ±0.02	0.07 ±0.004	0.21 ±0.009	0.29 ±0.01	0.19 ±0.001
ΔE				-0.015 ±0.011	0.000 ±0.025	0.040 ±0.027	0.011 ±0.028
E_{SM}	0.06 ±0.002	0.13 ±0.002	0.45 ±0.002	0.09 ±0.002	0.33 ±0.002	0.4 ±0.001	0.28 ±0.002
ΔE				-0.01 ±0.003	0.07 ±0.003	0.11 ±0.003	0.06 ±0.004
E_{MC}	0.03	0.10	0.28	0.07	0.15	0.22	0.15
ΔE				0.005	-0.005	0.025	0.014

Table 4-3 FRET efficiencies with their absolute error from bulk and SM measurements as well as MC calculations. *The efficiency increment ΔE is calculated as the difference between the averaged efficiency of single hetero-FRET pairs and their corresponding homo-FRET construct.*

FRET efficiency and enhancement calculations

Bulk steady-state fluorescence spectroscopy measurements provide information about the average emission of the sample under consideration. In this case it is impossible to calculate the exact energy transfer efficiency, because one cannot account for the fluorescence coming from structures that contain a different number of dyes than the target construct. To estimate the energy transfer, I simply consider the ratio-metric FRET efficiency, defined as the donor emission (I_{Cy3}), divided by the total emission of donor and acceptor (I_{Cy5}) at their maximum.

$$E_{Bulk} = \frac{I_{Cy3}}{I_{Cy3} + I_{Cy5}}$$

For constructs with Cy3 and Cy5 dyes only, since Cy3 is excited at 520 nm I assume the direct excitation of Cy5 to be negligible and correct the Cy5 emission only with respect to its spectral overlap with Cy3. The resulting spectrum was considered as the linear sum of Cy3 and Cy5 emission; the spectral overlap is corrected by subtracting 3% of the Cy3 emission signal at its maximum from the acceptor channel measured at 667 nm $I_{Cy5} = I^*_{Cy5} - 0.03 * I_{Cy3}$, where I^*_{Cy5} represents the uncorrected acceptor emission counts. In the calculations, it is assumed that if homo-FRET dyes were transferring energy to the acceptor independently, the green to red energy transfer of the constructs carrying multiple Cy3 dyes, E_{tot}, should be equal to the average of the hetero-FRET efficiency of each Cy3/cy5 pair:

$$E_{aver} = \frac{\sum_0^n E_i}{n} \lesseqgtr E_{tot}$$

FRET efficiency enhancement, ΔE, is calculated as the difference between the efficiency of the multiple Cy3 labeled structure and the average efficiency of the single constructs $\Delta E = E_{tot} - E_{aver}$

Breaking down the homo-FRET chain

To analyze all the possible energy transfer pathways, I assembled a series of partial constructs with two green dyes (Figure 3 B-D). For the G_1G_2XR construct, a slight decrease in red emission was observed, compared to the sum of G_1XXR and XG_2XR, while the difference of green emission falls within the sample variability, indicating a slight reduction of the energy transfer efficiency. No consistent difference in energy transfer is observed for G_1XG_3R when compared to the sum of XXG_3R and G_1XXR. The construct XG_2G_3R, on the other hand, shows an energy transfer increase of $\Delta E = 0.04$ as compared to the average contribution of XXG_3R and XG_2XR. This result indicates an enhancement of the energy transfer of about 18%, where both hetero- and homo-FRET occur with the highest efficiency.

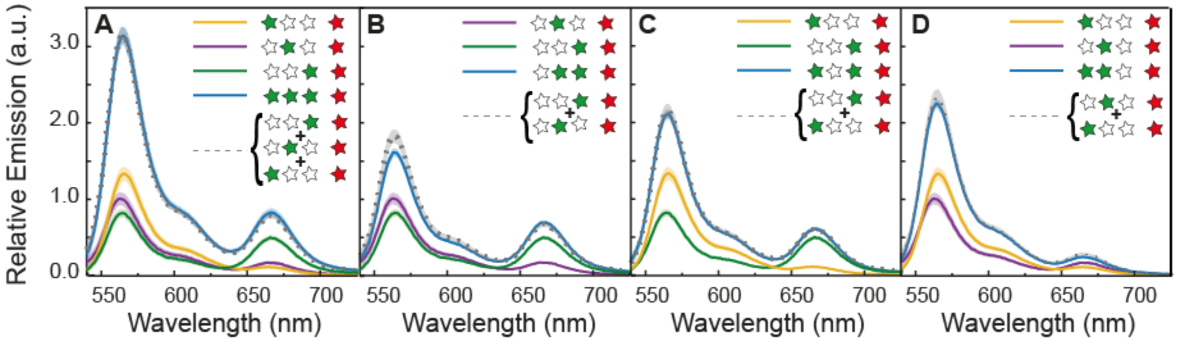

Figure 4-9 Two-color cascade: *(A-D) bulk emission spectra of constructs carrying a variable number of Cy3 dyes and a single Cy5 acceptor. The recorded emission intensities are normalized by the intensity of the Cy5 emission after Cy5 excitation in order to account for differences in sample concentration. The shading around the plotted lines indicates the error of the mean (the final spectra are the result of an average of multiple measurements on at least 6 different sample batches). The comparison between the spectra of the constructs containing two Cy3 dyes (blue lines) and the mathematical sum of the spectra of the respective partial constructs with only one Cy3 (gray lines) is shown for* XG_2G_3R *(A),* G_1XG_3R *(B),* G_1G_2XR *(C) and* $G_1G_2G_3R$ *(D).*

However, in ensemble experiments, an average value is measured and errors arising from variations in dye-DNA labeling efficiencies and incomplete incorporation of DNA staples[161] cannot be easily corrected, limiting the understanding of the system. To address these limitations and to obtain complementary data, in-solution single-molecule FRET measurements were also performed by burst analysis. These measurements were performed by others within the collaboration of the project. In burst analysis experiments, single molecules are measured at picomolar concentration as they diffuse through the femtoliter-sized observation volume of a confocal microscope on the timescale of a few milliseconds. When diffusing each single origami is excited by both a laser pulse in resonance with the donor and a following pulse in resonance with the acceptor. The single-molecule FRET results are thus not biased by the efficiency of acceptor strand incorporation into the origami. It was found that the fraction of constructs missing an active acceptor fluorophore varies between 7 and 23 %, which affects the ensemble results. The FRET efficiencies of all the constructs obtained by single molecule measurements are summarized in table 4-3. From these values I calculated the enhancement obtained for the different homo-FRET wires following the same approach as for the bulk spectroscopy. The same trend as for the ensemble measurement is observed (see table 4-3 and figure 4-10).

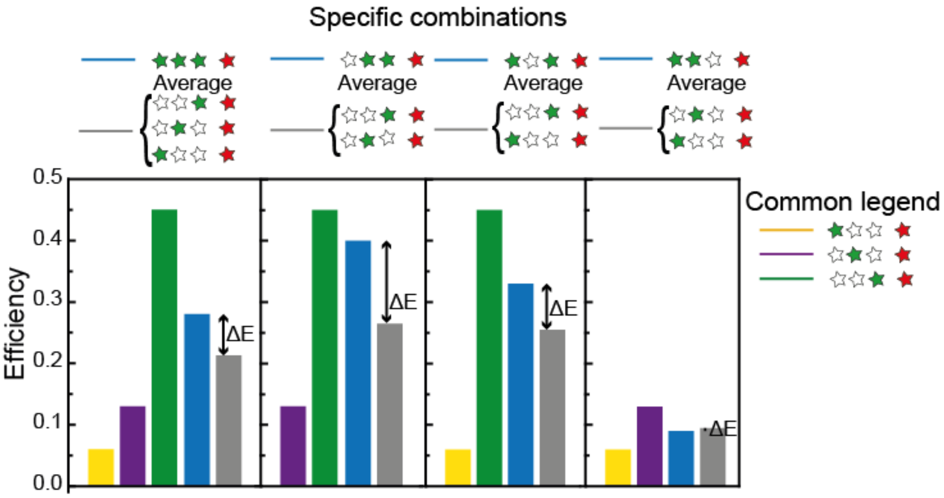

Figure 4-10 Two-color cascade: *Single molecule FRET efficiency of constructs carrying a variable number of Cy3 dyes and a single Cy5 acceptor. The comparison between the efficiency of the constructs containing two Cy3 dyes (blue lines) and the mathematical average of the efficiency of the respective partial constructs with only one Cy3 (gray lines) is shown for* $G_1G_2G_3R$, XG_2G_3R, G_1XG_3R, *and* G_1G_2XR *(from left to right). Errors in determining the efficiency are stated in table 4-3.*

4.4.4 Discussion

Since homo-FRET can be interpreted as a diffusive process between molecules without preferential direction,[133,135,162] in theory no change in the overall transfer efficiency is expected. If the green fluorophores were acting as independent molecules, the emission of the full construct should be equivalent to the sum of the single components, *i.e.* the ensemble of independent energy pathways should be equal to the sum of the parts. The observations of enhanced energy transfer in the constructs XG_2G_3R and $G_1G_2G_3R$, however, indicate that the dyes are not acting independently but instead that homo-FRET is contributing to the increase of energy transfer. Given the experimental conditions, saturation effects are precluded and only one green dye is excited at any time. Previous studies showed that cyanine dyes linked to DNA exhibit Förster behavior down to a distance of ~8 base pairs and hetero-dimer formation was only observed at distances of < 6 base pairs.[20,163,164] Thus the eventuality of contact quenching and dye-dye strong interactions can be ruled out, and the role played by homo-FRET in the energy transfer process can be solely considered. The short distance between the green dyes promotes an efficient energy exchange among them, while the proximity of G_3 to the acceptor dye, which acts as an energy sink, depletes the energy from the homo-FRET system. Here, the hetero-FRET process creates an energy hole on G_3, which can subsequently accept more energy from G_1 and G_2 and again transfer it to the final acceptor. This mechanism of efficient migration of energy from G_3 to R could explain the increased energy transfer of these constructs. In the G_1XG_3R assembly, only a small enhancement was observed in the ensemble experiments, but a clear enhancement is evident from the single-molecule results. Here, the homo-FRET distance is larger than in the construct $G_1G_2G_3R$ and XG_2G_3R, resulting in a reduced homo-FRET transfer efficiency. In spite of the reduced delocalization of energy over the homo-FRET system, the results indicate that the depletion by G_3 still results in an enhancement of energy transfer. On the other hand, for G_1G_2XR, the lower efficiency of hetero-FRET diminishes the depletion of the homo-FRET system by the energy sink, resulting in no net enhancement for this construct.

As the contribution of a homo-FRET system to energy transfer is not intuitive, the enhancement was confirmed by modeling the photonic wire with Monte Carlo (MC) simulations. The MC simulations were performed using standard theory of Förster-type energy transfer. To better simulate the system, the limited rotational freedom of the fluorophores on the origami platform has to be taken into consideration in the calculation. Often, the dipole moments of fluorophores are assumed to rotate freely so that the orientation factor, κ^2, for the FRET efficiency averages to 2/3. However, the attachment of the fluorophores to the flat surface of the DNA construct limits the accessible volume of the dyes. Additionally, the rotational freedom can be partially hindered by the interaction between the dyes and the DNA.[159,163,165] These considerations can be implemented by sampling different angular configurations for each energy transfer step in the system. Here, each of the partial and the full homo-FRET constructs were modeled assuming isotropic dipole orientations within a half-sphere for the different dyes, and no preferential directionality for the energy transfer in the homo-FRET part of the wire. FRET efficiency values from fluorescence bulk measurements of single hetero-FRET pairs were used to establish the simulations parameters. In case of homo-FRET, since the efficiency cannot be measured directly, values calculated from the overlap integral and the distance between the green dyes had to be used. The overall transfer efficiencies obtained from the simulations are in very good agreement with the bulk experimental values (see table 4-3). Importantly, the FRET efficiencies from the MC calculation of homo-FRET constructs also show an increased energy transfer of 16% for XG_2G_3R and 10% for $G_1G_2G_3R$ and a negligible change for G_1XG_3R and G_1G_2XR ($\Delta E < 0.01$).

Anisotropy measurements

As previously illustrated, homo-FRET cannot be calculated *via* spectral shifts. The method of choice to gain information about the system is to measure anisotropy. Fortunately, anisotropy data is also available from the aforementioned single-molecule experiments, with the values for each homo-FRET construct summarized in table 4-4. The triple-labeled construct, $G_1G_2G_3$, showed the largest change in the residual anisotropy ($\Delta r_\infty = 0.052$), a clear indication of efficient homo-FRET. All double-labeled constructs also exhibited a reduced residual anisotropy as compared to the single-labeled constructs. The highest difference is observed for the construct XG_2G_3 ($\Delta r_\infty = 0.032$), and the lowest for G_1G_2X ($\Delta r_\infty = 0.014$). Surprisingly, G_1XG_3 ($\Delta r_\infty = 0.023$) shows a higher change in residual anisotropy, and thus a higher homo-FRET efficiency, than G_1G_2X, even though the distance between the dyes is larger (5.4 nm vs. 4.6 nm). The influence of the dipole-dipole orientation is an important factor in FRET.[166] For the single-labeled constructs, the measured anisotropies of $r_\infty \approx 0.22$ for donor and acceptor in the case of homo-FRET indicate a possible effect of the orientation on the transfer efficiency. Furthermore, the interdependence of the quantum yield and steric hindrance for Cy3 introduces a correlation between the rotational flexibility and the Förster radius. Thus, differences in the local environment or unfavorable orientation of the dipoles of the dyes could explain the higher efficiencies of homo-FRET for construct G_1XG_3 as compared to G_1G_2X.

	G_1XX	XG_2X	XXG_3	$G_1G_2G_3$	G_1G_2X	G_1XG_3	XG_2G_3
r_∞	0.219 ± 0.007	0.216 ± 0.009	0.223 ± 0.006	0.167 ± 0.004	0.203 ± 0.007	0.198 ± 0.004	0.188 ± 0.006
Δr_∞				0.052 ± 0.006	0.014 ± 0.009	0.023 ± 0.006	0.032 ± 0.008

Table 4-4: Residual fluorescence anisotropy (r_∞) of single- and triple-labeled Cy3 constructs. *Δr_∞ indicates the differences of these values for the multi-dye constructs with respect to the average value of the single-dye constructs. Errors are given as 95% confidence intervals.*

As a control, a construct with large separation between the three Cy3 dyes was measured. In this configuration there is not homo-FRET transfer among the dyes (see figure 4-11). The anisotropy of this system ($r_\infty = 0.226$) is comparable to the one of the single dyes.

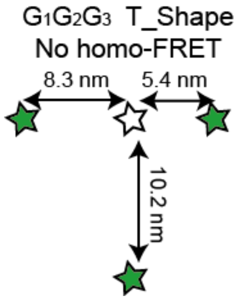

Figure 4-11 Scheme of control construct. *In this arrangement of dyes on the DNA origami the distances between Cy3 dyes are all* $> 2R_0$*, therfore no homo-FRET is allowed.*

4.4.5 Three-Color Photonic Wire with Localized Excitation

This work so far demonstrated that the intermediate dyes can perform homo-FRET and that this phenomenon does lead to higher energy transfer over the 10.5 nm distance of the dye assembly compared to the single FRET pairs. However, any one of the three green dyes can be initially excited in the system. To localize the excitation and study directed energy transfer through the homo-FRET system, I investigated the full three-color cascade PW, where a blue primary donor is placed 5.4 nm from G_1 (figure 4-7). First I verified that no energy transfer can occur between the blue donor and the red acceptor without intermediate green dyes (Figure 4-12). When exciting the construct BXXXR at 490 nm, no emission from the 660-670 nm region of the spectrum was observed (blue curve), indicating that neither the energy is directly transferred nor is the partial excitation of Cy5 taking place. Subsequently, to confirm the presence of the acceptor dye the same sample was excited at 640 nm, leading to detection of Cy5 emission (red curve).

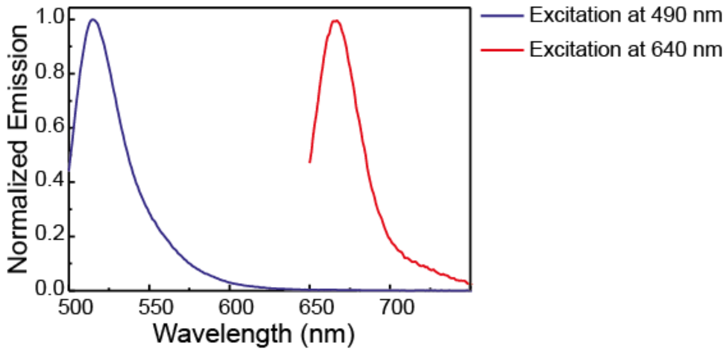

Figure 4-12: *spectra of the construct BR, containing only Alexa488 and Cy5. The sample was excited at two different wavelengths, 490 nm (blue line) and 640 nm (red line). The blue spectrum shows emission from Alexa488 only, indicating that no transfer to Cy5 is occurring, even though the presence of the acceptor is confirmed by the red spectrum.*

After this control, I separately measured the previous constructs in the presence of the blue fluorophore. To estimate the energy transfer efficiency from the blue donor to the red acceptor dye, the percentage of red signal after excitation of the blue dye was used. In case of three-color FRET, the emission spectrum is complex, since it results from the convolution of the superposition of three different spectra, partially overlapping with each other. To estimate the emission from each single dye component, a correction for spectral cross-talk has to be performed. I performed a linear decomposition of the three spectra, Alexa488, Cy3 and Cy5. By varying the weight of each spectrum, it is possible to extract the relative emission of all the components (Figure 4-13).

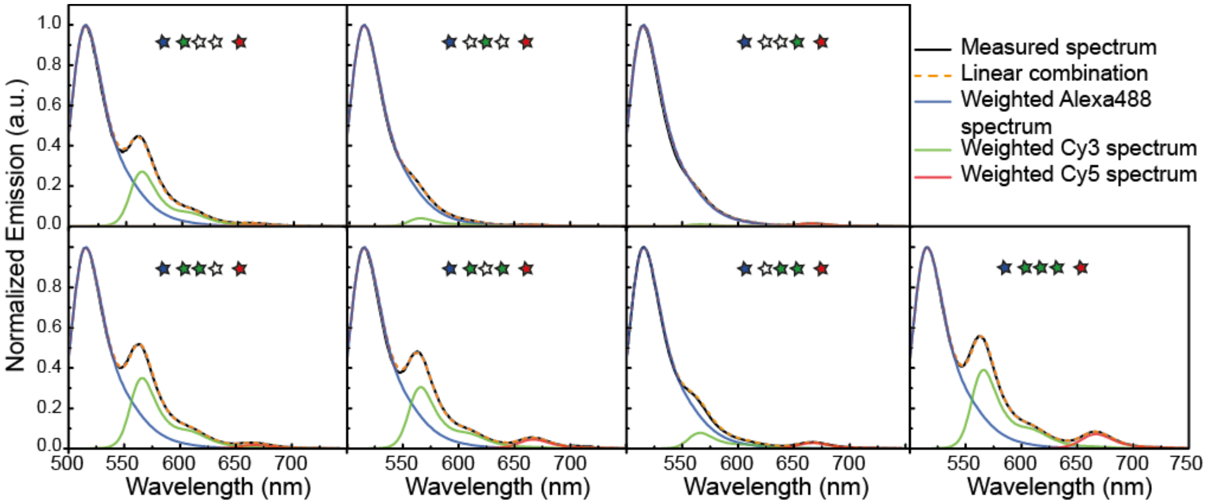

Figure 4-13 Three-color FRET cascades. *All the spectra are normalized by the Alexa488 emission. The contribution of each dye to the total spectrum is evaluated through a linear combination of the emission of each cascade dye (dashed orange line). Each weighted spectrum is also represented, Alexa488 (blue), Cy3 (green), Cy5 (red).*

Furthermore, in order to efficiently excite Alexa488, at 490 nm, there is non-negligible amount of direct excitation of Cy3. It is possible to shift the excitation wavelength further into the blue region of the spectrum, but only for constructs with an efficient blue to red transfer. In fact, in the energy cascades with only one intermediate dye, the blue to red transfer is very inefficient and the signal of Cy5 becomes comparable with the noise of the instrument. Therefore, for excitation at 490 nm, I estimate the apparent energy transfer efficiency of the constructs as the ratio between the red intensity peak ($I_{Peak\ (Cy5)}$) and the sum of the intensity peak of blue ($I_{Peak\ (Alexa488)}$), green ($I_{Peak\ (Cy3)}$) and red fluorophore. The intensity values are corrected for cross-talk between dyes (see linear decomposition of spectra figure 4-13), but not for the partial direct excitation of Cy3.

$$E = \frac{I_{Peak\ (Cy5)}}{I_{Peak\ (Alexa488)} + I_{Peak\ (Cy3)} + I_{Peak\ (Cy5)}}$$

To prove that the energy in the PW is indeed transferred through the homo-FRET chain, the focus is on the comparison between different numbers of intermediate dyes. The presence of only one intermediate green dye results in very low or undetectable emission from the red acceptor ranging from 0.6% to 1.3% in bulk measurements (Table 4-5). For constructs with two green dyes, the observed increase in the apparent transfer efficiency from the blue dye to the red fluorophore ranges from 1.3% to 3.3%. The full photonic wire with all three Cy3s produces an increase in energy transfer efficiency to 5% as measured in bulk.

	BG$_1$XXR	***BXG$_2$XR***	***BXXG$_3$R***	***BG$_1$G$_2$XR***	***BG$_1$XG$_3$R***	***BXG$_2$G$_3$R***	***BG$_1$G$_2$G$_3$R***
E_{Bulk}	0.006 ±0.008	0.006 ±0.003	0.013 ±0.007	0.013 ±0.01	0.025 ±0.012	0.033 ±0.004	0.049 ±0.012
E_{SM}	0.051 ±0.02	0.028 ±0.0019	0.037 ±0.022	0.056 ±0.022	0.095 ±0.032	0.048 ±0.027	0.098 ±0.037
E_{MC}	0.006	0.004	0.01				0.044

Table 4-5 Blue to red transfer efficiency. *Values are from bulk emission spectroscopy. SM and MC calculations. The errors are the standard deviation of the mean (bulk) and the FRET efficiency distribution standard deviation (SM).*

To visualize this increase, I compared the sum of the red emissions of all single-Cy3 dye wires, BXXG$_3$R, BXG$_2$XR and BG$_1$XXR, with the complete wire BG$_1$G$_2$G$_3$R (Figure 4-14 A). Since exciting the blue donor at 490 nm results in partial excitation of Cy3, I also performed bulk measurements with 460 nm excitation. In this case the signal and the signal-to-noise significantly decrease, but the emission from the red dye can still be detected (see Figure 4-14 B). The results are fully consistent with the spectra obtained with excitation at 490 nm. As for the green/red wires, SM FRET and MC simulations were performed on the constructs carrying the blue dye. The results are summarized in table 4-5 and show the same trend as in the bulk measurements.

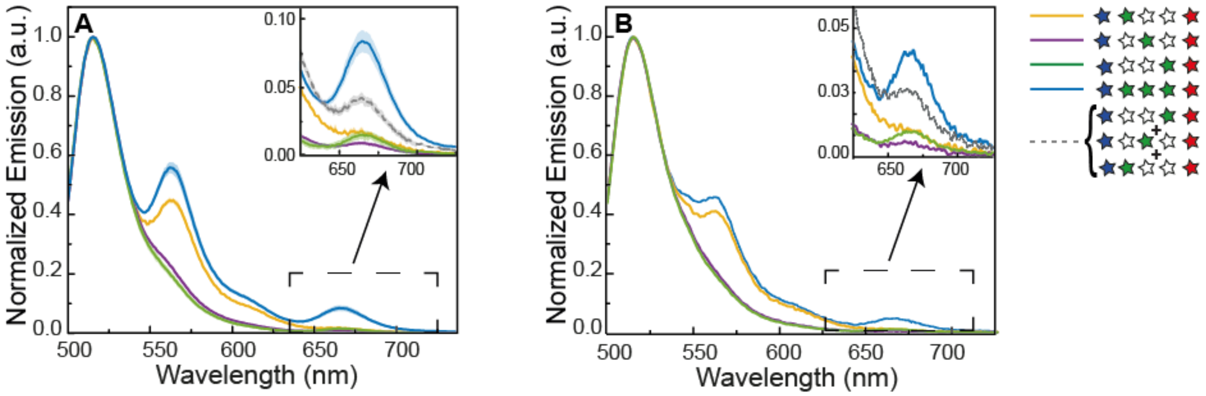

Figure 4-14 Three-color cascade. *Normalized emission spectra of the three-color cascade after Alexa488 excitation (A)at 490 nm and (B) at 460 nm. Due to spectral overlap between Alexa488 and Cy3, the green emission peak around 550 nm only becomes apparent for constructs where the closest dye to the blue donor is present. Inset: Zoom into the Cy5 emission spectral region. Wires with only one green dye do not show a significant emission of the red acceptor. Cy5 emission appears when all three Cy3 dyes are present. The gray line represents the arithmetic sum of the red signals from BG$_1$XXR, BXG$_2$XR and BXXG$_3$R, which is significantly lower than the red emission from BG$_1$G$_2$G$_3$R.*

4.4.6 Conclusion

In this work, I demonstrated a photonic wire mediated by a homo-FRET chain consisting of three Cy3 fluorophores. The observations show that homo-FRET amongst the Cy3 dyes can have an enhancing effect on the overall energy transfer to the acceptor fluorophore. The occurrence of homo-FRET between all Cy3 dyes was confirmed by a decrease of the fluorescence anisotropy. Lastly, it was shown that energy can be transferred through the homo-FRET system from a blue donor dye to a red acceptor dye over a distance of 16 nm. In summary, the energy transfer enhancement and the insights about the homo-FRET process investigated in this work can be utilized as a guide to extract design principles for complex light-harvesting assemblies on biological platforms, such as DNA, protein capsids and lipid membranes as well as on artificial systems such as dye-sensitized solar cells.

5 DNA functionalization of CdSeS/ZnS quantum dots

DNA self-assembly has been proven to be a powerful and useful technique for arranging nano-components in custom-tailored configurations. In order to integrate such components with DNA structures, one has to be able to link the object of interest, for example metallic NPs, fluorophores, and semiconductor nanocrystals, with one or multiple DNA strands. In this chapter a novel method for the functionalization of QDs with DNA is presented. Compared to pre-existing protocols, the presented approach is very simple and does not rely on any chemical modification of the DNA molecule.

Part of this chapter is based on reference [31]. Reproduced with permission from ref. 31, Journal of American Chemical Society, under review.* Unpublished work copyright 2018, American Chemical Society. *As submission date of this work

5.1 The importance of functionalization

As described in chapter 2, it is possible to incorporate nano-components within a DNA structure, such as DNA tiles or DNA origami, at a specific position. To achieve this goal one has to perform three main steps: functionalization of the object with the DNA strands, design of binding sites on the DNA template, and adjustment of the experimental conditions for the assembly process.[10,89] The first step, functionalization, is of great importance because it determines if and with what specificity a component can be bound to a DNA template. Next to this fundamental characteristic, in the case of metallic and semiconductor NPs, DNA functionalization also fulfills another critical role; stabilizing its surface in buffer solutions of high ionic strength.[167–169] While fluorphores are relatively small molecules and can be chemically linked to one DNA strand, NPs have a large (relative to their size) surface area that is usually passivated by either a chemical group or a polymer to guarantee their mono-dispersity in aqueous solution. DNA nanosctuctures must be surrounded by a high ionic strength solution (typically several mM of $MgCl_2$) to maintain their structural integrity, therefore any component that will be combined with them also has to be stable, *i.e.* monodisperse, in such conditions. DNA functionalization can lead to the stabilization of NPs in solutions of high ionic strength if the coverage of the surface by the DNA strands is dense enough to prevent aggregation. Such functionalization can be routinely achieved in the case of AuNPs,[169] but has remained challenging for QDs.[170]

5.2 The surface of QDs

Colloidal QDs are typically synthesized in solution through a bottom-up assembly process. First, the small core, which determines the optical properties of the QD, is grown. Since the size for achieving quantum confinement of the charge carriers is usually around a few nm, the particles have a very high surface area compared to their limited size, which means that surface defects and interactions with the surrounding medium become important effects.[37,40] In the case of QDs, defects and impurities at the surface, and oxidation from the environment can compromise the optical properties of the nanocrystal, creating trap states for the charges and quenching the fluorescence, respectively. To avoid these drawbacks, the surface of QDs is capped by a shell of another semiconductor material to improve quantum yield and surface passivation. There are different types of QDs, classified depending on the bad-gap difference between the core and the shell.[42,43] The QDs studied in this work have a CdSeS/ZnS structure and belong to the *type I* category, where the material of the shell, ZnS in this case, has a higher band-gap than the CdSeS core (see figure 5-1).

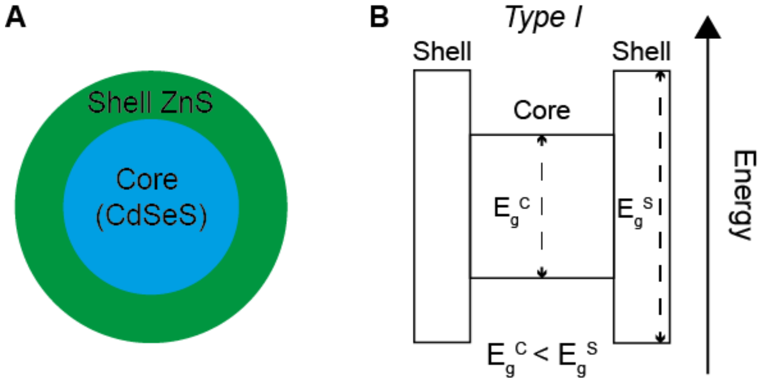

Figure 5-1 CdSeS/ZnS QDs band structure. *(A) Scheme of QDs structure. (B)Diagram of the band structure of a type I QD, such as CdSeS/ZnS.* E_g *indicate the energy of the bangap of core and shell materials.*

Usually, QDs are synthesized in an organic solvent and their surface is passivated by adding hydrophobic ligands, therefore they are not directly soluble in polar solutions. Consequently, to dissolve them in water a ligand exchange has to be performed. Common hydrophilic surface ligands often contain carboxyl or amine groups (e.g. mercaptopropionic acid (MPA) or functional amphiphilic polymers such as poly(maleic anhydride *alt*-1-ocatdecene). When functionalizing the NPs with DNA, to achieve a high surface density it is important that these surface groups are displaced by the DNA, thus allowing it to bind directly to the surface.[171]

5.3 Previous functionalization methods

Several methods have been developed in the past two decades to functionalize QDs with ss-DNA. These methods can be generally classified based on the different approaches in targeting the QD surface. The first approach relies on chemically modified DNA, which can bind directly to the QD surface by displacing the ligands. Similarly to the functionalization of AuNPs, thiolated DNA can bind directly to the ZnS QD surface, as shown by Mitchell *et al*.[172] This method has several limitations, including a poor DNA packing density on the surface, which presents the QD from being stable in high ionic strength buffers, and a lack of long term stability, as the bond between the thiol group and the surface is weaker than the thiol-gold bond. This results in the DNA strands progressively detaching from the surface. An alternative binding moiety is polyhistidine, a chain of histidine amino acids which has affinity to ZnS surface. QDs can be functionalized by DNA strands that are chemically linked to a histidine chain, with the peptide anchors on the NP surface leaving the DNA sequence free for hybridization.[173]

The second approach relies on covalently linking the ligands to the QD surface with a DNA strand. The DNA strand is chemically modified with a specific molecule that can react with the specific ligand. One common method to link molecules in solution is EDC-NHS coupling (commonly used for example in fluorophores-DNA functionalization). EDC is known to activate carboxyl groups for the reaction with primary amines to form amide bonds. As mentioned above, carboxyl-containing ligands are indeed commonly used for capping QDs, therefore EDC-NHS coupling is a relatively common procedure to link amine-terminated DNA strands to carboxyl-terminated QDs.[171] Nevertheless the method has drawbacks, including high concentrations of un-reacted chemical groups and reaction by-products in solution, poor DNA loading, and low yields. To improve the method Sun *et al*[170] integrated EDC-NHS coupling with a common protocol for DNA functionalization of AuNPs known as salt aging. They were able to load up to 20 DNA strands with a yield $> 70\%$. The QDs were stable in buffers containing up to 300 mM NaCl.

A approach similar to covalent linking is to utilize the high affinity between two biomolecules, biotin and steptavidin. Their strong bond is widely exploited in biochemistry, for example for the preparation of binding assays and for surface functionalization. The latter was successfully extended to QD-DNA conjugation. Streptavidin-coated QDs are readily commercially available, as are biotinylated DNA strands. The method is very simple, it consists of simply mixing the QDs and the DNA in solution, followed by a purification step where the excess unbound DNA is removed. This approach was also proven successful in combination with DNA nanostructures such as tiles and DNA origami.[174,175]

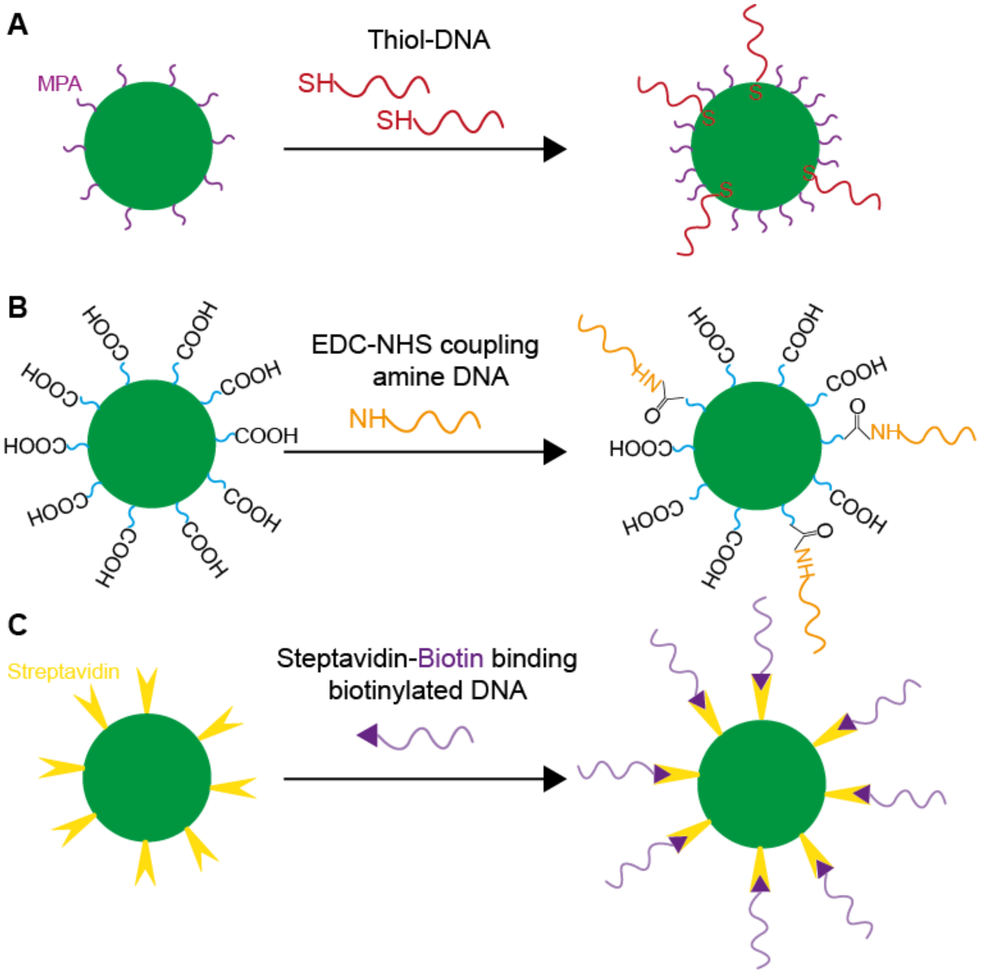

Figure 5-2 Overview of QDs functionalization methods. *(A) Direct link of a thiol modified DNA strand to the QD surface. (B) Scheme of a EDC-HNS coupling between an ammine modified DNA strand and the carboxyl groups capping the QD. (C) Streptavidin coated QDs can be functionalized with DNA strands carrying a biotin molecule through high-affinity streptavidin-biotin binding.*

The third and final approach for functionalization of QDs with DNA relies on making the conjugation during QDs synthesis. With this strategy a binding block of DNA strands is designed to be embedded into the QD during the NP growth in solution. To this purpose both thiolated DNA and strands with a phosphothiolated modified backbone (PTO-DNA) were used. DNA can be used directly as a capping agent during the synthesis of the core, or can be embedded into the shell during the growth process along with the primary surface ligand.[176–178] Utilizing the former method, Den *et al*[177] were able to arrange DNA functionalized QDs on a DNA origami template. Recently it has also been shown that long segments of PTO modified DNA can be anchored to the surface of QDs to control the number of strands surrounding the particles.[179,180]

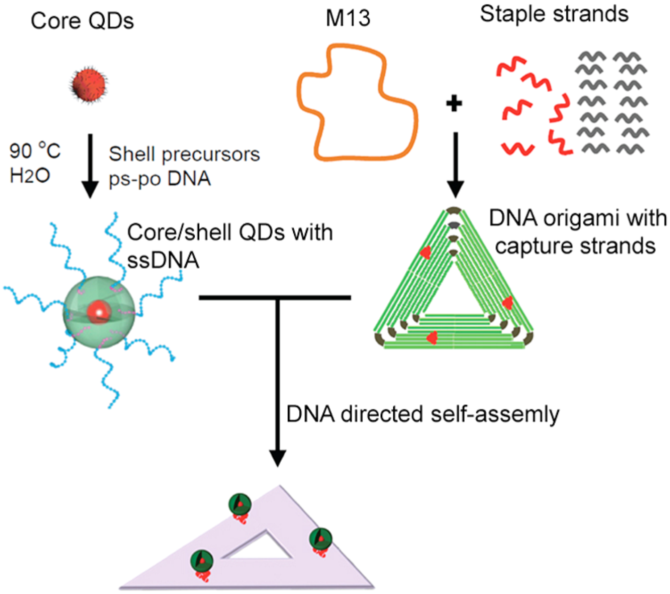

Figure 5-3 QDs functionalization by embedding DNA in the shell. *Scheme of the DNA-QD conjugation and the integration of such QDs with DNA nanostructures. Reproduced with permission from Ref. 177 copyright (2012) American Chemical Society.*

5.4 DNA base-affinity functionalization of ZnS-shelled QDs

Although successful in linking DNA strands to QDs surfaces, the above mentioned protocols present drawbacks of poor DNA loading, poor stability in buffers with high ionic strength, thus making it difficult to integrate them with DNA nanostructures. Some of the more promising methods require extensive knowledge of QD synthesis and specialized equipment, which makes them less accessible to researchers lacking an expertise in chemical synthesis, working outside of highly equipped chemistry laboratories. Furthermore, the overall size of QDs linked to DNA *via* long molecules or *via* biotin-streptavidin binding becomes significantly larger, which inhibits potential applications of these construct in the field of photonics and nano-optics, where it is extremely important to control the position and the distance between optically active components. In this work a facile and fast DNA-QD conjugation method is developed for QDs with a ZnS shell using modification-free DNA strands. The technique does not rely on complex chemical synthesis, but takes advantage of the affinity between ZnS and the unmodified (native) purine DNA bases, Guanine and Adenine. With an approach that is similar to poly-A binding to gold nanoparticle surface,[181,182] one can design a segment within the DNA sequence to contain only purine bases, serving as the functional QD ligand, and a segment to be rich in T or C bases, serving as handle for further specific hybridization (Figure 5-4 A). Importantly, the purine-ZnS affinity for DNA without PTO modification has to be accounted for even when using other functionalization methods. The efficient functionalization process is carried out in water and can be completed at room temperature in as little as 15 min. To further test the conjugation method, I assembled hetero-dimers consisting of a ~ 5 nm gold nanoparticle and a single QD on ss-DNA templates as well as QDs on DNA origami structures.

5.4.1 Affinity of DNA bases to the ZnS shell

The four DNA nucleobases, Adenine (A), Guanine (G), Thymine (T), and Cytosine (C) can be divided into two chemically distinct subgroups: purine bases (A and G) and pyrimidine bases (T and C). In comparison to pyrimidines, purines are composed of two fused heterocyclic aromatic rings of which one is an imidazole and the other a pyridine. The imidazole- and pyridine-type nitrogens are well-suited for binding to metal ions. Aiming to test the affinity of each nucleotide to the ZnS shell of commercially obtained QDs and to find an optimized DNA sequence with high affinity to QDs surfaces, diblock oligonucleotides were designed containing an anchor block of poly-G, poly-A, poly-C or poly-T and a poly-T hybridization block. In the experiments, the water soluble CdSeS/ZnS QDs with carboxyl moieties on their surface were used as received from the manufacturer (Cytodiagnostics). The affinity of each anchor block – with either PTO-modified or native phosphate DNA oligonucleotides – to QDs was tested, with agarose gel electrophoresis (1 mM EDTA, 10 mM Tris buffer, pH 8.2). A single and sharp band indicates a monodisperse QD sample with good colloidal stability.

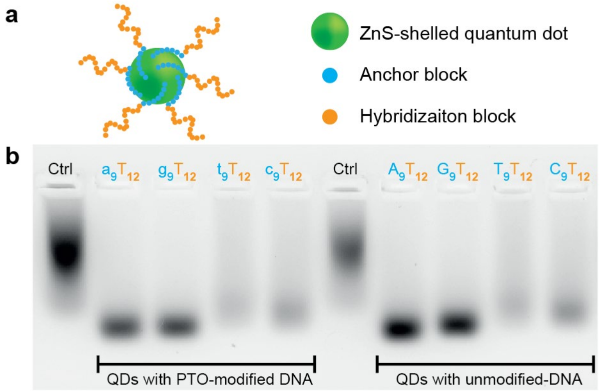

Figure 5-4. Purine-specific QD functionalization. *(a) Purine DNA bases interact with ZnS-shelled QDs. The anchor block (blue dots) consists of purine-bases (A or G) while the hybridization block (orange dots) is composed of pyrimidine bases (T or C). (b) Gel electrophoresis screening of the affinity of DNA bases to ZnS-shelled QDs. Functionalization sequences with PTO-modified DNA (indicated by lower case letters) and DNA with native phosphate backbone (indicated by upper case letter). Ctrl: QDs without DNA.*

In contrast, clusters of the QDs remaining in the loading pocket or smeared migrating bands indicate the lack of uniform and stable surface coverage, leading to aggregation of the particles. When QDs were functionalized with poly-G and poly-A anchor blocks, regardless of having PTO modifications or not, a single, clean fluorescent band was observed **(**figure 5-4 B). On the contrary, bare QDs and QDs functionalized with poly-T and poly-C anchor blocks – even with PTO modifications – smeared in the gel or aggregated in the loading pockets. It is noteworthy that the latter samples aggregated less than the bare QDs, a hint of unspecific interactions with DNA.

5.4.2 Optimization of the functionalization protocol

To further optimize the functionalization method, other candidate sequences were examined, consisting of n G bases (G_n, n = 1, 3, 5, 7, 9, 20 and 40), which bind to the ZnS surface (anchor block) followed by 12 T bases (T_{12}) which have less affinity with the shell, serving as hybridization handles (hybridization block). By screening with the help of electrophoresis, a series of parameters such as temperature, incubation time, amount of functional bases, and the ratio of DNA to QDs, a robust conjugation protocol was established. The experimental results are summarized in figure 5-5. Unless stated otherwise, all samples loaded onto the gel (1 mM EDTA, 10 mM Tris and 5.5 mM $MgCl_2$ running buffer) were incubated with DNA strands of the sequence G_nT_{12} , and subsequently purified from excess DNA using a centrifugal filter with a 100 kD MWCO (see material and methods). Here, guanine was chosen as the DNA base for anchoring to the QD surface, but similar results were obtained with adenine (figure 5-4 B).

Neither, varying the temperature range nor the incubation time had any influence the conjugation efficiency (Figure 5-5- A and B). However, QDs incubated at lower temperatures appeared brighter, which suggests that the high temperature treatment reduced their quantum yield. The minimum length of the anchor block was found to be 7 nucleotides of guanine or adenine (Figure 5-5 C) and a molar ratio of DNA/QDs > 200:1 was required (Figure 5-5 D) for successful binding. Although DNA strands containing fewer G bases are believed to increase the graft density, short functional segments such G_3 bases cannot provide enough binding energy to achieve stable DNA-QD conjugates at room temperature (figure 5-5 C). DNA strands containing G_{20} or G_{40} are long enough to wrap around the QD, thus passivating its surface. The wrapping of a long poly-G (> 20G) could potentially be used to fine-tune the number of DNA strands around the QD, as shown by other similar conjugation methods.[179,180] This method can be applied to any size of QD thus covering the full optical spectrum (figure 5-5 E).

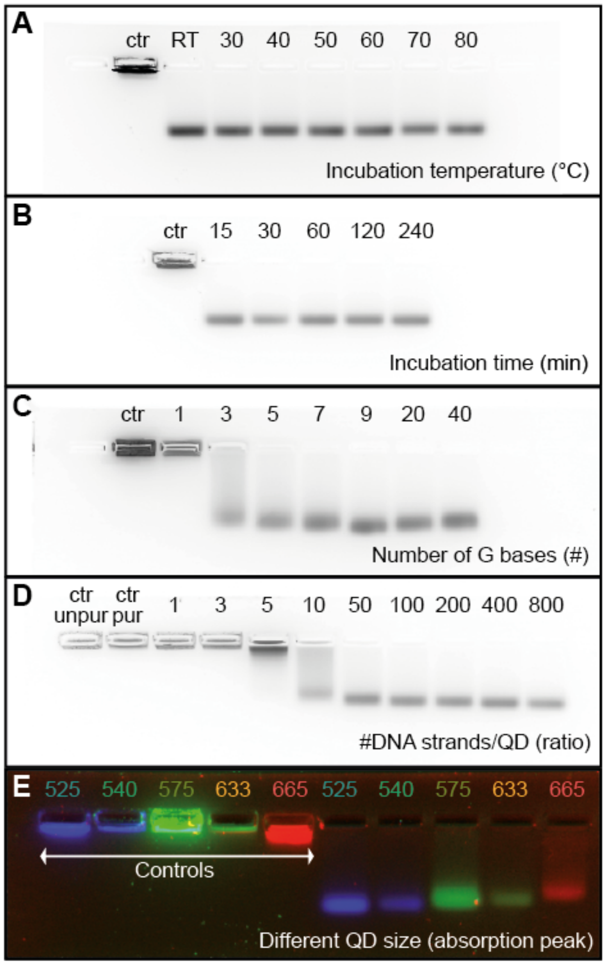

Figure 5-5. Probing functionalization parameters. *QDs incubated with (A) sequence* G_9T_{12} *at different temperatures (RT: room temperature), (B) sequence* G_9T_{12} *at RT for different amount of time(C) sequences* G_nT_9 *containing different numbers n of G bases, and (D) different amounts of DNA using the sequence* G_9T_{12}*(numbers indicate the molar ratio of DNA:QDs). (E) DNA functionalized QDs of different emissions wavelength with optimized parameters (numbers indicate emission peak wavelength in nm). The multichannel image was acquired with BioRad ChemiDoc MP gel imager, excitation at 302 nm and band-pass emission filters at 518–546 nm, 577–613 nm and 675–725 nm, respectively false-colored in blue, green and red. Ctrl: QDs without DNA.*

I measured the bulk optical properties of 540 QDs (emission at 540 nm) before and after DNA conjugation. Absorption and emission spectra do not show significant peak shifts (Figure 5-6 A). DNA functionalized QDs were deposited on carbon-film-coated grids (300 mesh Cu; TED Pella, Inc; prod no. 01753 – f) and characterized under TEM. The QDs appeared monodisperse, both before and after DNA conjugation (Figure 5-6 B).

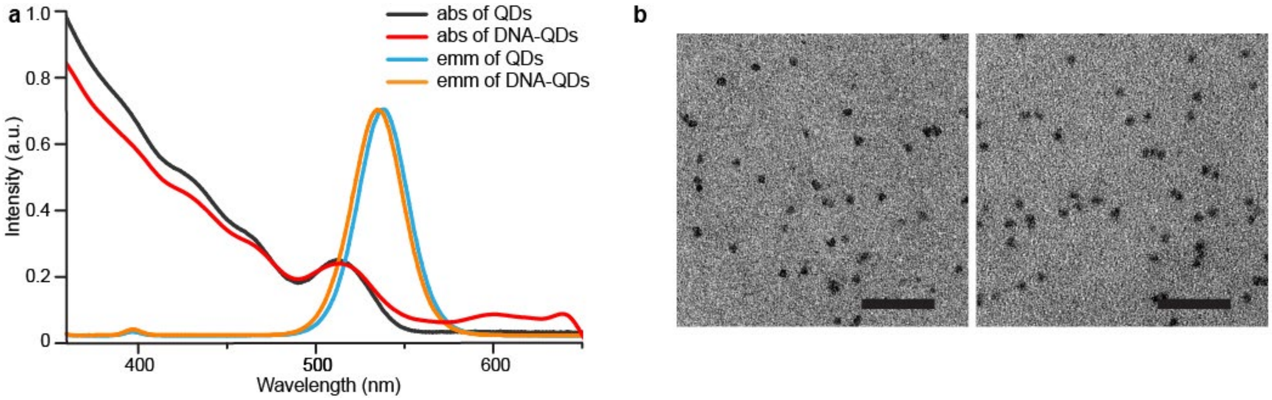

Figure 5-6 Optical properties and mono-disperity of QDs after DNA functionalization. *(A) Bulk measurement of absorption and emission spectra of QDs (emission at 540 nm) before and after DNA functionalization. (B) TEM images of QDs before (left) and after (right) DNA functionalization (scale bar 50 nm). Colloidal dispersity was unaffected after DNA functionalization.*

5.4.3 Discussion

Previous reports have established phosphorothioate DNA as a crucial and sufficient agent for DNA-QD conjugation.[177–180] Nevertheless, unsuccessful conjugation was observed with strands containing poly-T or poly-C segments of PTO-modified DNA; successful conjugation was instead achieved with poly-A or poly-G segments of DNA with a native phosphate backbone. These results suggest that the thiol groups of the PTO backbone are not the essential ligands, even though thiol groups have a higher binding energy towards ZnS than nitrogen and oxygen.[177] In guanine or adenine, the N7 nitrogen is believed to be the strongest intrinsic binding site for Zn^{2+} and Cd^{2+}.[161] If there are no free zinc ions in solution, the zinc atoms located at the QD surfaces may serve as similarly attractive binding sites to be chelated by DNA ligands. The other groups such as O6 oxygen in guanine and the phosphodiester bridge can participate with multiple purine bases (at least 7 as described above) to provide sufficient binding energy to displace the existing carboxyl ligands and coordinately stabilize the DNA-QD conjugates.

5.4.4 QD-Au heterodimers

To verify the accessibility of the hybridization block of the DNA functionalized on the QDs, the site-specific assembly of QDs was tested on ss-DNA templates and on DNA origami structures (figure 5-7 A). QDs functionalized with the sequence G_9-ATG TAG GTG GTA GAG were added together with 5 nm gold nanoparticles (AuNPs) previously functionalized with a thiolated T_{19} sequence and a template ss-DNA (A_{19} CTC TAC CAC CTA CAT), which is complementary to the DNA on the AuNPs and the QDs. The components were mixed in a ratio of 5:5:1 (AuNPs : QDs : ss-DNA) and incubated at room temperature overnight. The target assemblies were purified *via* agarose electrophoresis to separate them from the excessive amounts of QDs and AuNPs, and from higher order aggregates. Due to the low color contrast of the QD-AuNP construct, I ran a Au-Au construct and used it as a reference to cut “the gel band” of Au-QD dimer. Since the QDs have a similar size to 5 nm AuNPs and a comparable surface charge due to the presence of DNA, Au-Au and QD-Au constructs are expected to ran at a similar speed. Gel electrophoresis and TEM imaging confirmed the successful assembly of the dimer heterostructures comprised of one QD and one AuNP (Figure 5-7 B and C).

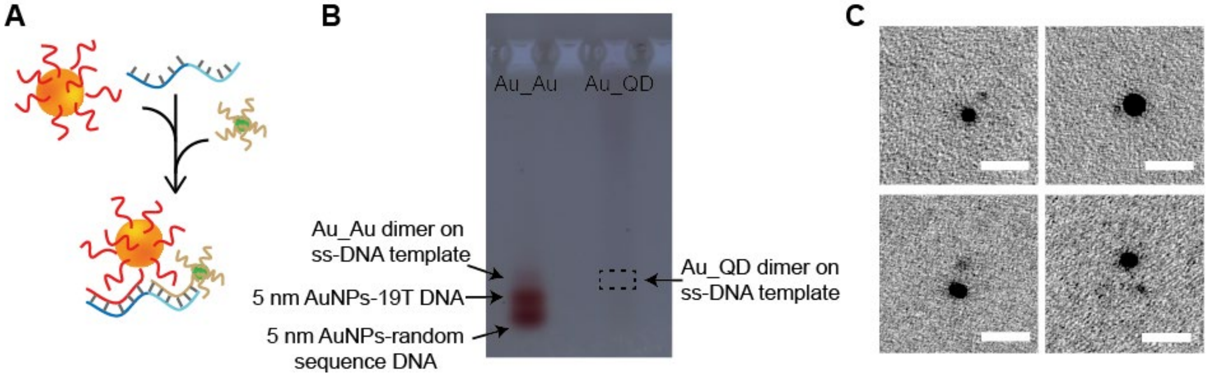

Figure 5-7 Assembly of QDS-Au heterodimers. *(A) Schematic figure of the assembly of a gold nanoparticle and a quantum dot on a single-stranded DNA template. (B) Gel purification, the gel band position of the Au-QD construct was determined from the referential position of the Au-Au dimer construct. (C) TEM images of QDs-AU heterodimers extracted from the gel in (B), scale bar 20 nm.*

5.4.5 QDs assembly on DNA origami

To further validate the method, QDs modified with G_9T_{15} sequence were assembled on a ring-shaped DNA origami to test site-specific attachment (see scheme in figure 5-8 A). The structure exhibits four binding sites, each one consisting of three identical single-stranded staple extensions. The attachment to three different origami structures was tested: one with poly-A handles to which QDs should bind, one with poly-T handles to which QDs should not bind, and the last one without any binding sites. Typically, G_9T_{15} modified QDs were mixed with ring origami structures in a molar ratio of 5x excess per binging site and incubated overnight in 1x TE, 11 mM $MgCl_2$. Samples were run in a 1% agarose gel (Figure 5-8 B). All three structures, DNA(G_9T_{15})-QDs mixed with origami with ploy-A, origami with poly-T handles and origami with no handles, show a clear fluorescent band indicating the presence of QDs on the origami, as later verified by TEM (Figure 5-8 C). Poor sequence specificity of the DNA-QD conjugates was observed when binding to the origami structures. In addition, QDs can attach to single-stranded scaffold regions due to missing staples,[161] which can explain the attachment of QDs also to structures without handles. I speculate that the unspecific attachment could be due to the low DNA grafting density on the ZnS-shelled QDs surface, allowing purine nucleotides to occupy areas free of ligands.

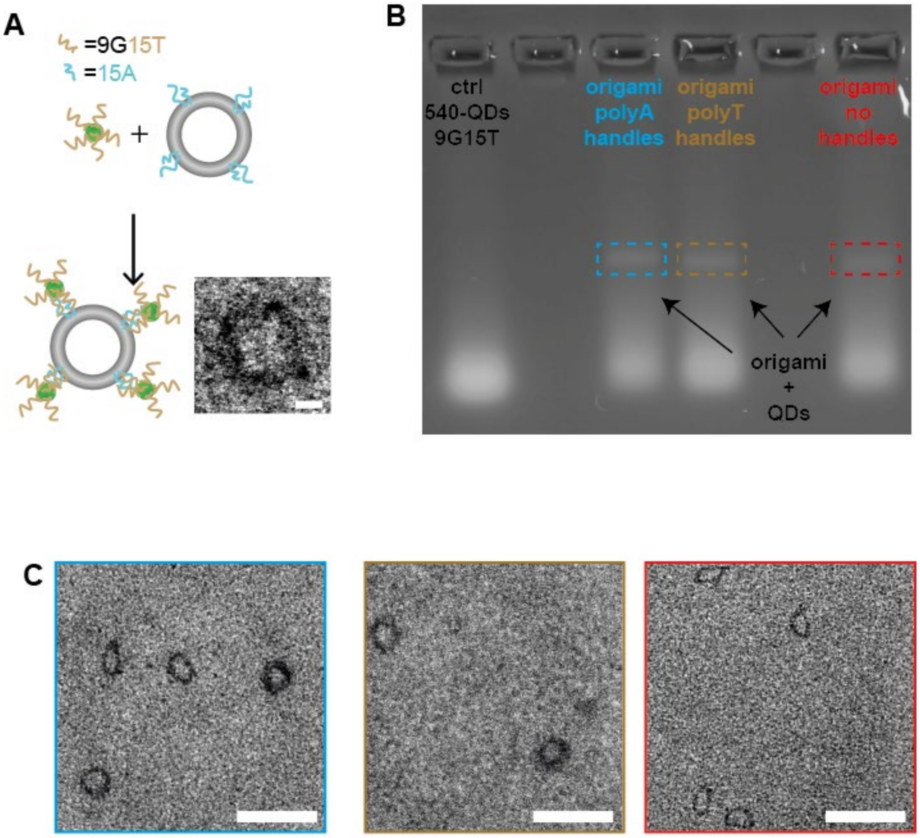

Figure 5-8 QDs assembly on origami: *(A) Scheme of the ideal assembly of QDs on the origami ring structure with corresponding hand-picked TEM picture (scale bar 20 nm) to show that the target assembly is possible, but not predominant. (B) Gel purification of the origami ring structure and QDs. Three mixtures are loaded in the gel: G_9T_{15} modified QDs mixed with origami containing, from left to right, poly-A, poly-T and no handles. The gel is not stained; the fluorescence originates from the QDs emission. (C) TEM images corresponding to the sample extracted from the gel in (B). From left to right: origami with polyA handles, origami with polyT handles, and origami without handles. The structures are not stained to facilitate the imaging of QDs. For all three samples, I saw the attachment of DNA-QDs. Scale bar 100 nm.*

5.4.6 Conclusion

This work demonstrates a facile and fast method for DNA-QD functionalization using native phosphate DNA strands containing poly-G or poly-A segments as anchor blocks. In contrast to commonly employed methods, which rely on additional surface chemistry or on PTO-modified DNA, this efficient functionalization process can be completed at room temperature, in water and within only 15 minutes. The accessibility of the DNA hybridization block was verified *via* site-specific assembly of the modified QDs on ss-DNA templates, proving that this method can be used to fabricate complex hybrid structures for future studies of, for example, QD-QD and QD-metal nanoparticle interactions.

6 DNA self-assembled antennas

In this chapter a novel method to assemble MNP nanoantennas with a single QD in the gap is presented. First, a general overview about the importance of building plasmonic nanoantennas with a single quantum emitter in their vicinity is discussed. The hybrid system consisting of QEs coupled with plasmonic NPs must meet two important fabrication requirements: i) control over the physical size of the field confinement and ii) control over the reciprocal arrangement of the field and the emitter. The advantages of assembling QE-MNP systems with DNA self-assembly over conventional nanofabrication methods are then illustrated. Finally, the method developed in this work of placing a single QD in between the gap of two MNPs will be explained. The functionality of the devices for harnessing QE-Plasmon interaction is confirmed by measurements of plasmon resonance, fluorescence, and SEM imaging.

Part of this chapter is based on reference [32]. Reproduced with permission from ref. 32, ACS Nano, under review.* Unpublished work copyright 2018, American Chemical Society. *As submission date of this work

6.1 Plasmonic nanoantennas

When incident radiation is coupled longitudinally to two metallic nanoparticles (NPs) that are in close proximity, oscillating electrons, or plasmons, produce a localized region with a strongly enhanced field. The increased field strength of such "hot-spots" has enabled several applications including optical trapping of small objects,[52] fluorescence enhancement for sensing molecules at low concentrations,[53] and Raman spectroscopy.[54,183] In the case of quantum emitters (QEs) located in a hot-spot, the plasmonic enhancement increases the absorption. In addition, the spatially confined field in such a plasmonic cavity exhibits quantized modes that promote spontaneous emission, the so-called Purcell enhancement.[184] Both plasmonic enhancement and emitter-cavity interactions depend on the relative arrangement and proximity between the QE and the metallic NPs.[30,56,185] These interactions can be exploited to achieve integrated opto-plasmonics devices,[5] such as tunable single-photon emission sources with high photon yield and transition rates.[58,105,186,187] More interestingly, plasmon control over individual QEs provides many of the requirements demanded by quantum information,[56,184] including Purcell emission enhancement with directional routing,[58,186,187] the creation of superimposed plasmon-exciton quantum states, and non-linear optical effects for photonic switches.[188,189] Great efforts have been undertaken on controlling the Purcell enhancement in plasmonic cavities. It is known that the quality factor (Q) of a plasmonic antenna is usually only on the order of a few tens.[190] Therefore, a small mode volume (V) is desired in order to obtain a high plasmonic-mediated Purcell factor ($P \sim Q/V$).[51,56] To this end, gaps between two closely spaced metallic NPs are ideal to place single QEs with the goal of achieving deterministic, modular, and high throughput assembly of QE-antenna complexes.

6.2 Advantages of DNA self-assembly in the fabrication of nanoantennas

Top-down fabrication approaches, and in particular photolithography have been the workhorse behind the progresses made in nanotechnology. Despite huge improvements in the capabilities of these techniques, they have intrinsic technical limitations on the resolution achievable in the fabrication of small features dictated by the diffraction limit.[59] In particular it is very challenging to realize metallic structures with small gaps < 10 nm, and also to create devices where different materials and nanocomponents are integrated. In addition to these physical restrictions, lithography requires very specialized laboratories and expensive equipment, which are a practical limit in many circumstances.[60,191,192]

As already illustrated in chapter 2 DNA self-assembly is a valid alternative to current fabrication methods to arrange nano-coponents, such as MNPs, fluorophores, QDs, nanodiamonds, and proteins, in a nanometer precise manner. This control over the spatial resolution is accompanied by the ability to integrate different components and different materials on the same DNA template structure. This versatility of DNA self-assembly represents an unprecedented opportunity for the construction of nanoantennas and hybrid QE-MNPs devices.

Many nanoantennas were already successfully fabricated with DNA self-assembly, either by exploiting DNA strands as direct linkers between the particles[54,104,105,193] or by using rigid DNA templates such as DNA origami.[194–197] Such devices have been exploited for sensing, fluorescence enhancement of fluorophores[194] and QDs,[193] and to promote strong coupling between the excitons of

J-aggregate and the plasmons of a nanoantenna.[197] Two main distinctions regarding the placement of the exciton with respect to the hot-spot have to be made. In some of these examples of DNA self-assembled antennas, the MNPs' reciprocal position and distance were always controlled by design of the DNA template and the DNA strands, but the placement of the components of interest, either a flurophore, QD, or Raman reporter molecule, was not always precisely controlled. For example in Thacker *et al*[195] the molecules providing enhanced Raman signal are not linked to the DNA structure, but rather are detected when they flow through the hot-spot. In Roller *et al*[197] the J-aggregate solution was randomly deposited on top of antenna structures immobilized on a surface and not placed, by design, directly in the hot-spot. This somewhat unspecific approach is very efficient in the case of sensing, either through SERS or fluorescence, but it is too uncontrolled for studies on specific plasmon-exciton interactions, because the number of QEs in the hot-spot has to be controlled. In fact one of the highly desired aims of the nano-optics field is to be able to place a single QE at the center of the cavity, because such a device could be a true single-photon source.

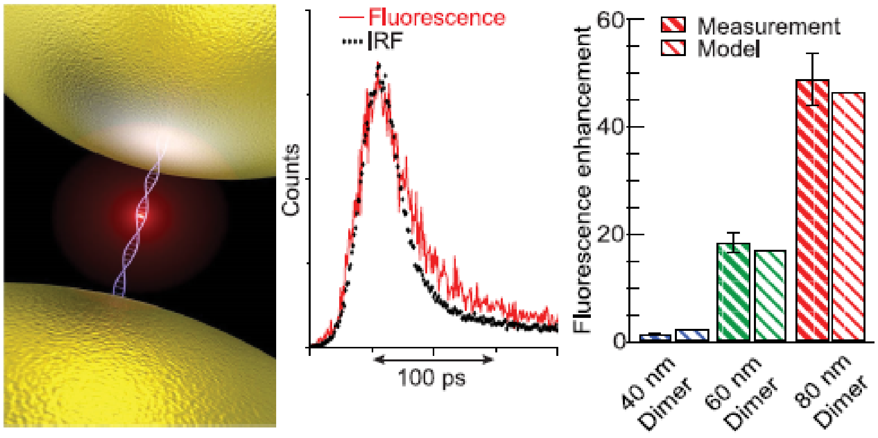

Figure 6-1 Antennas linked by one DNA strand. *(Left) Schematic of the DNA link between the AuNPs and fluorophore location. (Right) Fluorescence enhancement and lifetime shortening measured with this antenna. . Reproduced with permission from Ref. 104 copyright (2016) American Chemical Society.*

A great potential toward this direction has been shown by a nanoantenna consisting of two MNPs linked *via* a DNA strands carrying a single fluorophore (see figure 6-1) presented by Bidault *et al*[104] and a QD positioned in the gap of AuNPs by Cohen *et al.*[193] Despite these approaches' success in exploring and pushing the limit of fluorescence enhancement, the gap-size between the AuNPs is still >10 nm and the NPs are not fully covered by DNA but mono-functionalized, which is a laborious process and does not stabilize the NPs in high ionic strength conditions.

6.3 DNA-Mediated Self-Assembly of Plasmonic Antennas with a Single Quantum Dot in the Hot-Spot

Here, DNA is used to build plasmonic structures with small gaps. Employing DNA strand complementarity in combination with stoichiometric tuning and steric-hindrance, I assemble plasmonic antennas, consisting of two 40 nm metallic NPs (MNPs) with a single colloidal QD positioned in between. It is shown that this method is easy to implement, no complex DNA mono-functionalization[105,198] or protein coverage[193] of the NPs is required, and that it provides high fabrication yield of antennas with a single quantum emitter in a small gap (~6 nm).

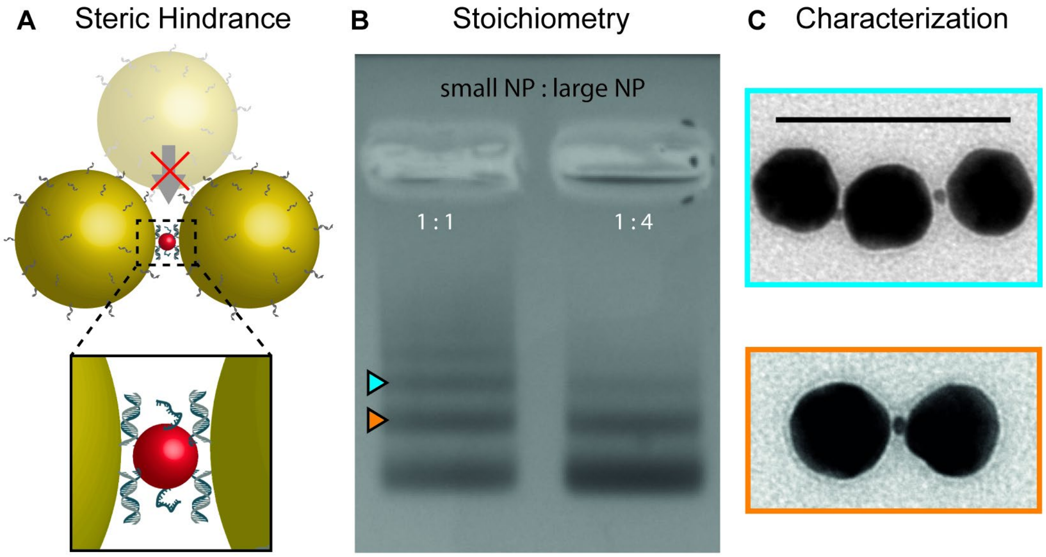

Figure 6-2 Assembly and characterization of the plasmonic antenna with a single small nanoparticle in the gap. *(A) Scheme of the assembly principle based on steric-hindrance and controlled stoichiometry. Zoom-in shows the DNA hybridization scheme ("zipper" conformation). (B) Purification process (gel electrophoresis, 1% agarose in 1x TAE and 5.5 mM* $MgCl_2$*) of the target structures, 1:1 and 1:4 refer to the stoichiometric ratio between 5 nm and 40 nm AuNPs. (C) Subsequent TEM characterization of structures extracted from the gel. Scale bar 100 nm.*

Moreover, compared to its lithographically produced counterparts, self-assembled structures made of colloidal NPs possess better crystallinity and are more versatile, as they can be readily deposited on any substrate, representing a great advantage over the nanoparticle-on-mirror approach. To assess the modularity of the assembly process, I fabricated antennas with different MNPs (gold and silver) and measured their plasmon resonance. I then characterized the fluorescence emission enhancement of individual QDs placed in the hot-spot of the antenna by using wide-field epifluorescence, laser illuminated microscopy. Post SEM-mapping is performed to ensure that all reported emissions correspond to well-formed Au-QD-Au complexes. It is observed that depending on the antenna configuration, the fluorescence emission can be enhanced up to 30-fold compared to single QDs without an antenna.

6.3.1 Assembly principles

The antenna assemblies consists of one ~5 nm small NP (either a colloidal QD or a MNP), positioned between two 40 nm MNPs. Each species is separately functionalized with 15-nucleotide (nt) long DNA strands that are complementary to each other and mixed in solution in a ~1:5 small NP : large NP ratio. The disproportionate size difference and molar excess favor the formation of large NP – small NP – large NP assemblies. When two large NPs have docked *via* DNA hybridization to two sides of a small NP, the resulting excluded volume prevents the attachment of further large NPs (see assembly scheme in Figure 1a). The relative excess of large NPs over small NPs further inhibits the formation of long chains. Using this simple assembling strategy, a high yield of antennas was produced with an individual QD located at the center of the plasmonic cavity.

I explored the effects of varying stoichiometry and relative size between the two species. When reducing the stoichiometric ratio (N_{small_NP}:N_{large_NP}), the likelihood of obtaining higher order chains of nanocomponents increases, as free, small NPs in solution can bridge already formed antennas to additional large NPs. This process results in the formation of linear arrays of the type $large\ NP - \left(small\ NP - large\ NP\right)_n$ as seen in Figure 1c. Electrostatic repulsion of the charged particles maximizes their separation, leading to rather stretched conformations of the chains. If the reciprocal size of the particles becomes comparable ($r_{small\_NP} \sim r_{large\_NP}$), other assembly configurations such as non-linear structures can occur (figure 6-4). The different species assembled in solution can be purified through gel electrophoresis. In the unstained gels, multiple bands corresponding to different structures are visible (figure 6-2 B). Owing to the slower mobility of the higher order chains in the gel, there is a clear separation between the individual species, which allowed us to isolate and extract the structure of interest. After purification, the assembly yield of correctly formed -antennas within the extracted target band was estimated by TEM inspection (figure 6-2 C).

Quantification of the Yield and Proof of the Assembly Principle Using Steric-Hindrance

To quantify the yield of correctly assembled structures, I examined TEM images of ~100 constructs for each sample. Due to high contrast of the 40 nm AuNPs on TEM images, it is challenging to determine the presence of QDs in the gap. To avoid miscounts, I analyzed the analogue assembly of the antennas but with a 5 nm AuNP in the gap, which is clearly visible and further validates the generality of the assembly methodology. Depending on the initial ratio of 5 nm Au to 40 nm AuNPs, the number of structures without the small particle or with one or two small particles in the gap varies as reported in table 6-1 and in the histogram in figure 6-3.

Yield Analysis		
	Large NPs : Small NPs	
	1:1	**4:1**
2 Small NPs	**8.5%**	**3.8%**
1 Small NP	**84%**	**74.3%**
0 Small NP	**7.5%**	**21.9%**

Table 6-1 Assembly yield. *Statistics assembled structures as measured by TEM inspection*

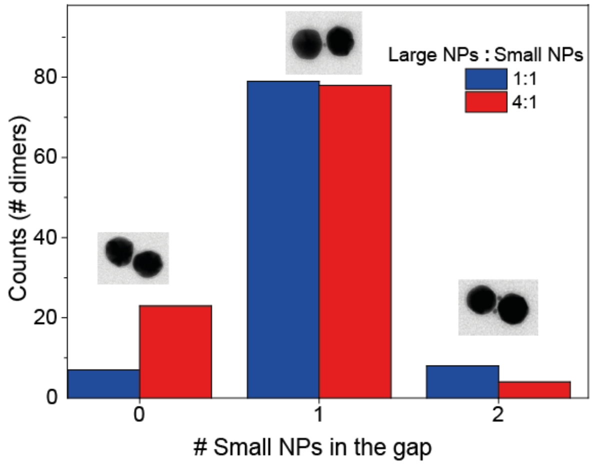

Figure 6-3 Frequency histogram quantifying the yield of correctly assembled structures. *For each AuNPs:QD ratio,* $\sim\mathbf{100}$ *dimers in TEM images were classified according to the number of QDs in the structure. TEM insets are visual representations of the assembly type*

It was found that depending on the N_{small_NP}:N_{large_NP} ratio, 74% to 84% of the structures correspond to the antenna assembly with a single small NP in the gap.

To test the steric hindrance principle limits on which the antenna assembly is based, I built structures with smaller AuNPs (10 nm and 15 nm). As the radius of the NPs gets closer to that of the QD (~5 nm), non-linear conformations become predominant such as conformations displaying angles (α) smaller than 180 degrees (figure 6-4 A) or structures where steric-hindrance no longer dominates, thus resulting on three or more AuNPs assembled around the QD (figure 6-4 B and C).

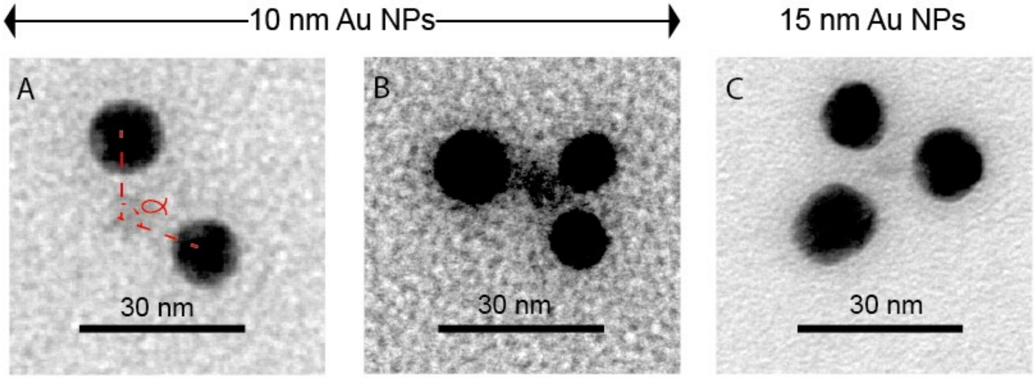

Figure 6-4 AuNPs-QD constructs with 10 and 15 nm AuNPs displaying non-linear conformations. *TEM imaging of A) exemplary Au-QD-Au structure displaying a large opening angle (*$\boldsymbol{\alpha < 180°}$*), and B) 10 nm and C) 15 nm AuNPs constructs where steric-hindrance no longer applies. QD is* $\sim \boldsymbol{5\ nm}$*.*

6.3.2 Assembly with different NPs

To demonstrate the versatility of this method, I assembled four distinct structures with different materials and characterized their plasmon resonance. I constructed one "all gold" structure where a single 5 nm AuNPs was placed in between two 40 nm AuNPs (figure 6-5 A), and three structures where a CdSeS/ZnS QD was placed in between two 40 nm MNPs (figure 6-5 B, C and D). For the QD antennas, I used either conventional available AuNPs which possess multiple crystal facets, ultrasmooth highly spherical AuNPs,[199,200] which are generally desired to obtain a narrower plasmonic resonance distribution of the assembled structures, or two silver NPs (AgNPs), which exhibit sharper resonances than their gold counterparts.[201]

I characterized the plasmon resonance of the Au-QD-Au antennas assembled with conventional particles and with ultrasmooth spherical particles. For the former, I obtained a spread in the plasmon resonance between 2.05 eV and 2.25 eV (figure 6-6 A). The spread is attributed to the variability of size and shape of AuNPs (see TEM image in figure 6-6 A), to the different conformations that the assemblies acquire during absorption and subsequent drying on the substrate, and to varying orientations of crystal facets, edges, and vertices of the not perfectly round NPs. In turn, antennas fabricated with ultrasmooth AuNPs show a more uniform plasmon resonance between 2.13 eV and 2.25 eV (figure 6-5 B).

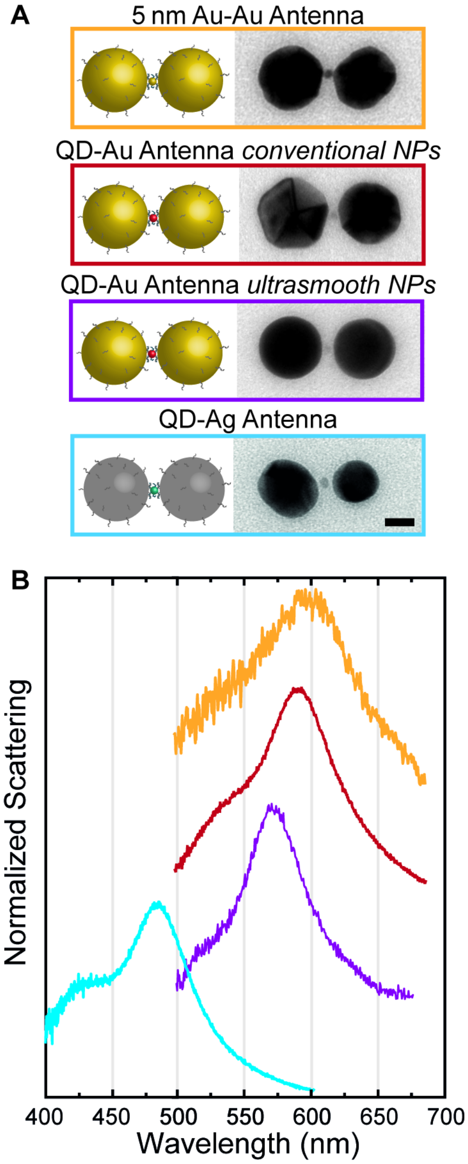

Figure 6-5 Assembly of the plasmonic antennas with different materials and characterization of the plasmon resonance. ***(a)*** *Scheme, TEM imaging, and* ***(b)*** *plasmon resonance of antennas made of all Au (orange), Au-QD with conventional AuNPs (dark red), Au-QD with ultrasmooth spherical AuNPs (purple), and Ag-QD (light blue). Scale bar 20 nm.*

The fluorescence emission of semiconductor QDs arises from electron-hole recombination processes at the band-gap of the particle and therefore exhibits a defined energy. QD absorption, in contrast, is continuous from the ultraviolet part of the spectrum all the way to the energy corresponding to the level difference of the first electron transition, where a peak arises (see appendix III for absorption and emission spectra of QDs). In the experiments, the plasmon of the antenna overlaps with a region of the absorption in such a way that the emission is only slightly shifted from the plasmon by 0.12 eV. Consequently, quenching by the AuNPs is expected.[202]

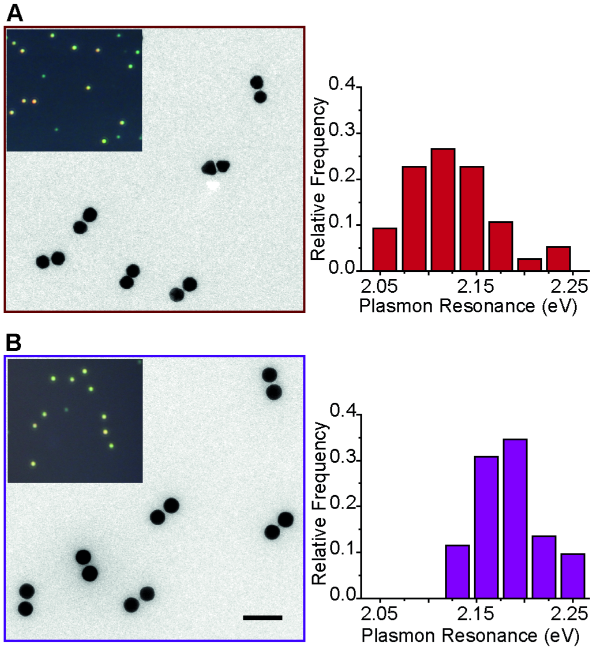

6-6 TEM images and plasmon resonance spread of Au-QD antennas. *Antennas fabricated with A) conventional and B) ultrasmooth AuNPs. TEM images show less variability of the ultrasmooth NP assemblies, displayed also in more uniform colors of the dark-field images. Also, the histograms of the respective plasmon resonances (> 50 spectra acquired for each assembly type) show a narrower spread for ultrasmooth NP assemblies. Scale bar is 100 nm.*

6.3.3 Fluorescence enhancement measurements

Finally, I studied the fluorescence emission properties of the structures immobilized on a glass surface in dry conditions. The emission was recorded with a single-photon sensitive camera in the emission pathway of an epifluorescence microscope[102] (see Material and Methods for the detailed description of the setup). Upon excitation with a circularly polarized laser at 561 nm, I monitor fluorescence from the area of interest by recording the emission intensity as a time series with a band-pass detection filter (570-620 nm). Subsequently, the same area was analyzed with a dark-field (DF) microscope and the resulting map was overlaid with the fluorescence image, as shown in Figure S5a. This procedure established a spatial correlation between spots exhibiting fluorescence and the scattering signals of the antennas. The matching of fluorescence and DF measurements allows the selective analysis of only those emission spots corresponding to the targeted structures while discarding any potential fluorescent contaminants.[203–205] From the series of frames obtained in the epifluorescence measurements, an intensity time trace was extracted for each fluorescent spot (figure

6-7 A). The emission traces were then correlated with the specific plasmon resonance spectrum (see figure 6-7 B) of each individual antenna (see appendix III for more details on the analysis). This procedure was performed on various areas of different samples and it helped to establish a solid correspondence between the fluorescence emission intensities and the plasmon resonances. Finally, to ensure the correct assembly of the analyzed structures, each antenna was imaged under SEM using the corresponding DF map as a reference (see figure 6-7 inset).

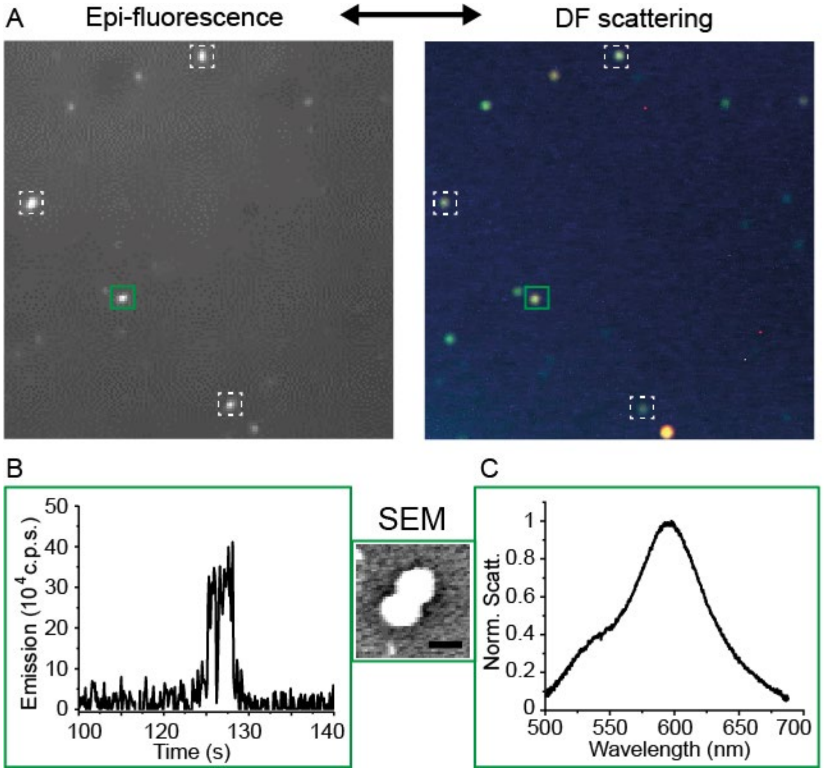

Figure 6-7 Mapping of the sample. *Overlapping (A) epifluorescence (left) and dark-field (right) images of the same area. Exemplary (B) fluorescence trace and (C) scattering spectrum of the spot highlighted in green. The inset shows the SEM image of the corresponding antenna (scale bar 50 nm).*

To determine the effect of the plasmonic hotspot on the QD emission behavior, I compared the fluorescence of single DNA-functionalized QDs with the emission from Au-QD-Au assemblies with conventional AuNPs and assemblies with ultrasmooth spherical NPs. Exemplary fluorescence traces of QDs and antennas are shown in Figure 4a, 4b and 4c, respectively. The single QDs traces display a relatively uniform behavior with an on-state emission intensity of $12.3\ (\pm 1.5) * 10^3\ c.p.s.$The individual QDs in the experiments started emitting immediately upon illumination and bleached after a short time. In contrast, the fluorescence emission of all analyzed QD-antenna structures is of greater intensity compared to that of the individual emitters. However, the intensity traces show different behavior from one structure to the other and range over two orders of magnitude. The on-states often display heterogeneous bursts, displaying multi-level emission intensities, as well as different on-state times.[206,207] Some antennas fluoresced as soon as they were illuminated, while others emitted photons only after some seconds of irradiation. The close proximity between the QDs and the metallic NPs could provide pathways that prevent surface charging, which directly affects the duration and intensity of individual on-states.

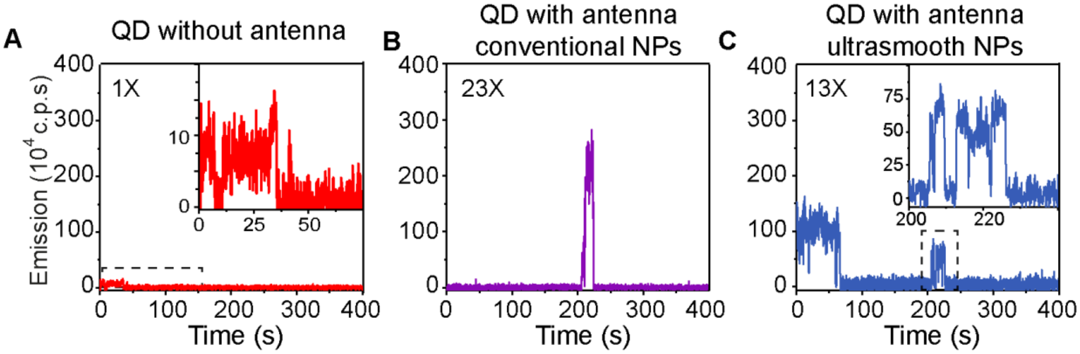

Figure 6-8 Time traces and antenna enhancement. *Exemplary fluorescence emission time-traces of (A) QDs and antennas made of (B) conventional and (C) ultrasmooth AuNPs. The antennas display enhanced bursts up to 30x compared to individual QDs. The enhancement of the displayed antennas is indicated by the number in the upper left corner. Acquisition binning is 100 ms. All antennas time-traces can be found in appendix III.*

Two physical processes are influenced by the presence of the antennas: absorption and emission rates (see appendix III for a theoretical description).[57,186,202] Changes in absorption rate depend on the overlap between the plasmon resonance and the strength of the field, while spontaneous emission is modified by the interaction between the emitter and the vacuum modes. To quantify the fluorescence emission enhancement of QDs positioned in the plasmonic antenna, I normalized each on-state by the average emission of single QDs without the antenna and obtained a maximum burst enhancement of ~30x. Although only 10-15% of the antennas lack a QD in the middle, only a fraction of the measured antennas display fluorescence within the acquisition time (400 s). This behavior is attributed to the quenching effect of the metal due to the overlap between the emission of the QD and the plasmon resonance of the antenna. Interestingly, antennas assembled with ultrasmooth spherical NPs display fewer bursts than the ones assembled with conventional AuNPs. I speculate that the high variability of the enhancement depends on the precise location of the QD within the gap, as corroborated by full-wave simulations (appendix III). In addition, the sharp edged of the NP facets of conventional particles can provide additional field enhancement, thereby counteracting the quenching by the metal. The yield of emitting antennas could be improved by using QDs of higher quality or by significantly detuning the QD emission from the plasmon resonance.

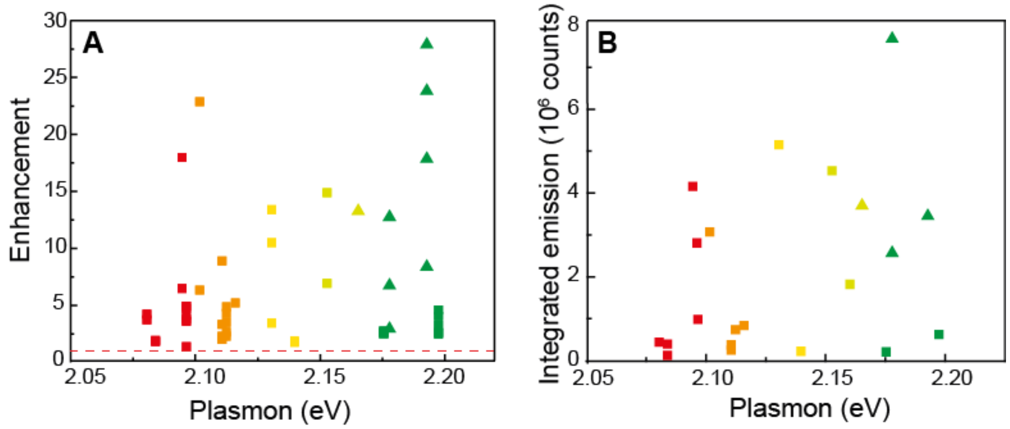

Figure 6-9 Correlation of fluorescence with plasmon resonance. *(A) Fluorescence enhancement and (B) integrated emission of several antennas as a function of each antenna plasmon resonance. Squares and triangles correspond to antennas made with conventional and ultrasmooth spherical AuNPs, respectively. The enhancement is normalized to the average QD emission (red dashed line), points of the same color correspond to different bursts of the same antenna. Time-traces of all points shown in the graph can be found in appendix III.*

Since the total emission enhancement depends on the plasmon coupling, the emission enhancement (maximum fluorescence) and the total emission (emission integrated over time) was correlated with the plasmon resonance of the respective antenna. The spread shown in the plots (figure 6-9) reflects both the intrinsic variability in the emission of QDs and their different locations with respect to the gap. As shown by TEM imaging, I observe multiple conformations of the antenna when the QD is located at the center of the gap, ranging from "stretched", "compressed" and "squeezed" conformations. Since the samples are dried after substrate deposition, initial landing and subsequent drying of the antennas on the TEM grid or substrate interactions do affect the ultimate dried conformation. During surface deposition, a droplet of sample is incubated for a few minutes, followed by droplet removal using an absorbing paper, and subsequent drying at room temperature (TEM grid deposition) or blow drying by a stream of nitrogen gas (glass slide deposition). During the drying process, any remaining liquid in the vicinity of the structures slowly evaporate, which leads to shrinking of the liquid meniscus around the particles and capillary forces acting on the particles.[208,209] Antennas assembled using ultrasmooth NPs display less variability with a preferred "compressed" conformation.

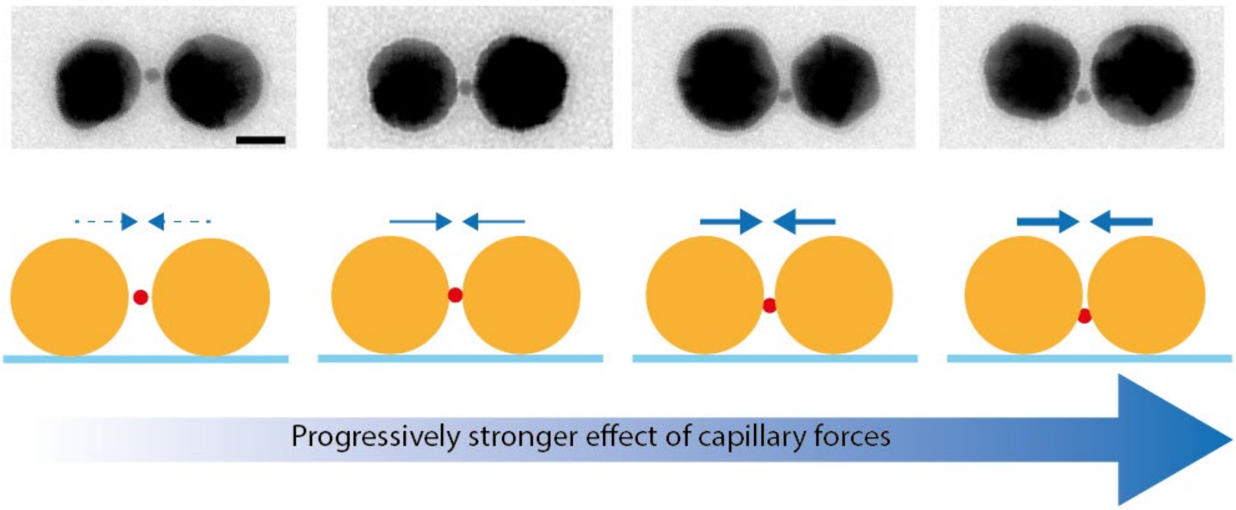

Figure 6-10 Antenna conformations. *Upper panel: exemplary TEM images of different conformations of the antenna constructs when deposited on a surface and dried. Lower panel: schemes corresponding to the conformation of the antennas observed in the TEM images. The small blue arrows indicate the progressively stronger effect of capillary forces due to drying effects (depicted with the big blue arrow).*

6.3.4 Control Experiment: AuNPs Dimer Mediated by DNA Origami

To further ensure that the fluorescence observed in the antennas originates from individual QDs and not from potential contaminants (*e.g.* DNA, buffer contaminants)[204,205] as a control I assembled structures consisting of two 40 nm AuNPs spaced by 5 nm without any central particle. The assembly of the this AuNPs dimer control is mediated by a DNA origami structure consisting of a 2-layer sheet with capture DNA strands located at the center of the structure on both sides of the block, so that one NP can dock on each side. The DNA origami is sandwiched between the particles, therefore serving as a gap spacer, as described in detail by Roller *et al*.[197] The estimated gap size is ~ 5 nm, which is a distance comparable to the QD diameter and gap size of the QD-antenna structures. The sample was gel purified, the correct assembly verified by TEM imaging (figure 6-11 A), and subsequently deposited onto a glass slide. The fluorescence and DF measurements were carried out as described for the QD-antenna constructs (figure 6-11 B and C). No emission from gold or potential buffer contaminants was observed. Nevertheless the counts from the dimers are not zero, as shown by several examples in figure 6-11 B (extra data are available in appendix III), but rather display a constant scattering baseline. This scattering is also accounted for when performing the antenna analysis by subtracting the scattering baseline from the emission traces.

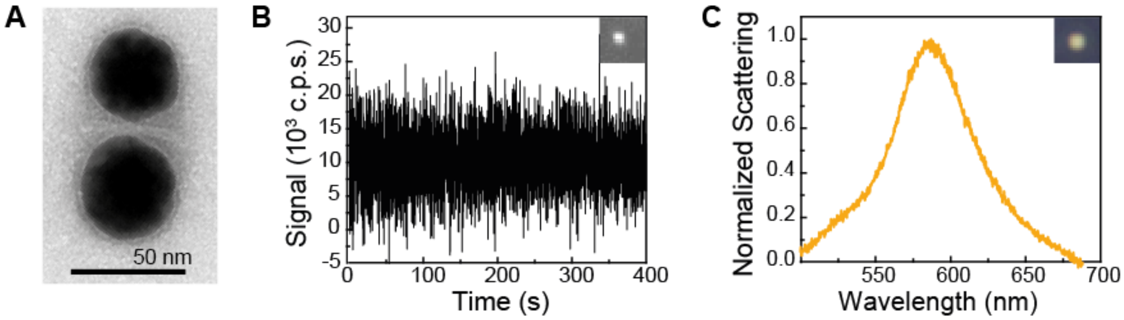

Figure 6-11 Dimer on 2LS origami. *(A) TEM imaging of the control structure, consisting of two 40 nm AuNPs docked one on each side of a 2-layer DNA origami block. (B) Epi-fluorescence time trace (inset fluorescent spot). (C) Scattering spectrum of representative AuNP-origami control structures (inset DF image).*

6.3.5 Conclusion

In this work, I presented a simple strategy to build plasmonic antennas with a single QD located at the center of the gap with high yields using DNA-mediated self-assembly. I demonstrate the functionality of these antennas by measuring fluorescence enhancement of the QDs up to 30-fold. Due to the fine tuning of this fabrication technique, which is based on steric-hindrance and controlled stoichiometry of the species, two fundamental requirements of nanoantennas were fulfilled: i) a very small gap combined with ii) a single quantum emitter positioned at the center of a plasmonic cavity. These two factors are important for the realization of single-photon sources and for the control over exciton-plasmon interactions. The presented simple self-assembly approach is scalable, as trillions of QD-antennas were fabricated in a few simple steps. This methodology can be extended to any other plasmonic material and any quantum emitter functionalized with DNA. Furthermore, these structures can be deposited and measured on different substrates, which implies advantages over small gap antennas fabricated *via* a mirror geometry.

7 Conclusion and outlook

In this work, I demonstrated how DNA nanostructures can be used to control light-matter interaction. From simple strands to more complex origami, the complete addressability of DNA molecules can be successfully used to precisely tailor the arrangement of optically active molecules and NPs at the nano- and sub-nanometer scale. The spatial resolution of DNA nanostructures represents an unprecedented improvement over the current state-of-the-art top-down fabrication techniques. Moreover, since different materials such as metals, semiconductors, and organic molecules can be integrated in the same device with ease, DNA-mediated assemblies can be used to explore physical interactions that were not possible to deterministically control using other fabrication techniques. Finally, their self-assembly properties simplify the fabrication protocols and allow for the realization and simultaneous creation of trillions of identical devices in a parallel manner.

In chapters 3 and 4, I demonstrated how arrangements of dyes mediated by DNA can mimic the natural light harvesting principles of photosynthetic organisms. Two different coupling regimes could be achieved in the interaction of fluorophores: strong electronic coupling and a long-range energy transport. The former required sub-nanometer control over the distance between two Cy3 molecules, which was achieved by exploiting the inter-base separation of a ds-DNA molecule. The fluorophores were arranged so that the formation of a dimer would be controlled by their distance, rather than by their hydrophobic π −stacking interactions driven by the condition of the solution. The new excitonic states rising from the dimerization were confirmed by absorption spectroscopy, theoretical modeling, and circular dichroism measurements. In the case of long-range energy transport I assembled a homo-FRET-mediated photonic wire on a rigid DNA origami block. The 16 nm long wire can transport energy from a primary donor to a final acceptor through a row of intermediate energy dyes, which can perform homo-FRET. Given the indistinguishable and non-directional nature of homo-FRET, I relied on the addressability of DNA origami to break down the complexity of the cascade and assess the contribution of each single dye to the transfer efficiency separately. The study demonstrated the emergent effect that the collective effect of the homo-transfer results in an enhanced efficiency, as opposed to the simple sum of the contribution from each single dye in the chain.

Both of these light harvesting mimic projects pave the way for the design and realization of devices for efficient light collection and transportation at the nanoscale. Further work in this direction will involve studies of exciton formation, charge separation and energy migration in artificial assemblies of dyes, similarly to what occurs in the case of natural LHCs. These phenomena occur on a very short timescale, from femto- to pico-seconds, so techniques measuring only fluorescence emission are not able to uncover their dynamics. To this purpose, advanced spectroscopy measurements such as transient absorption spectroscopy and 2D electronic spectroscopy would truly enable a direct comparison to the performance of LHCs, and enable improvements in the design of these artificial systems. Once again, DNA nanostructures are very good candidates for these types of measurements, since they can be easily measured both in bulk and at the single-molecule level, either in solution or immobilized on surfaces.

In chapters 5 and 6, I built a DNA-mediated plasmonic antenna with a single small QD positioned precisely in the gap. First, a new method for DNA-QD conjugation was developed. As opposed to commonly used protocols, this functionalization does not require any complicated chemical synthesis steps and furthermore does not rely on chemically modified DNA. I showed that by only using the affinity between specific DNA bases and the zinc shell of the QD, one can efficiently attach the desired DNA strands to the particle surface. The method makes the particles remain stable in buffers with high ionic strength, conditions that are needed in the field of DNA nanotechnology. I then used such DNA-QD conjugates to build a plasmonic antenna consisting of two 40 nm MNPs. With the demonstrated assembly method, I could construct antennas made of gold and silver in a highly parallel way. Since the gap of the antennas is given mainly by the size of the QD, it was estimated to be 6 nm, size which is not routinely achievable with top-down fabrication methods. Such a high precision in placing the QDs into the small gap between the MNPs makes these antennas the ideal platforms to study plasmon-exciton interactions. So far, these constructs have shown the ability to enhance the emission of QDs up to 30-fold, proving the functionality of the device for reaching the weak-coupling regime.

In order to explore to which limit exciton-plasmon coupling can be achieved with these antennas, future work will involve lifetime measurements of the exciton decay for quantifying the maximally achievable Purcell factor, and use larger NPs to strengthen the enhancement of the hot-spot. On the other hand, the use of DNA-based fabrication techniques means that it is also possible to build antennas with an even smaller cavity size, for example using 30 or 20 nm MNPs. These constructs are very good candidates for observing strong coupling, since the coupling constant depends on the inverse square root of the volume of the electric field produced by the antenna. Further work in this direction can be carried out by considering the saturation of the two level-system, and finely tuning light intensity used in dark-field spectroscopy measurements. Moreover, since antennas can be deposited on any substrate, they are also good candidates for measurements at cryogenic temperatures, where the plasmon-exciton interaction is expected to be enabled by the suppression of temperature effects.

Appendix I

Extra data and details on the simulation relative to the publication on which chapter 3 is based. All measurements were performed by me, while the simulations were performed by Mathias K. Ross based on the experimental details and results I presented.

DNA sequences

The following sequences were used:

Monomer 5'-ATC GTA TC T_{cy3} GTG TCT ATG CTA -3'

Dimer 1 base distance 5'-ATCGTATC T_{cy3}G T_{cy3}GTCTATGCTA-3'

Dimer 0 base distance 5'-ATCGTATCTG T_{cy3} T_{cy3}TGTCTATGCTA-3'

T_{cy3} indicates the modified thymine bases.

Cy3 link to the DNA strand

To better understand the constructs used in this work, I show below the functionalization schemes for linking Cy3 to DNA. In the case of Cy3-monomer, Cy3-G-Cy3 and Cy3-Cy3 dimer the dye is linked to thymine bases of the DNA strand by NHS-ester reaction (Scheme 1.a). In this case Cy3 has only one anchor point to the DNA, consisting of a 6-CH linker chain.

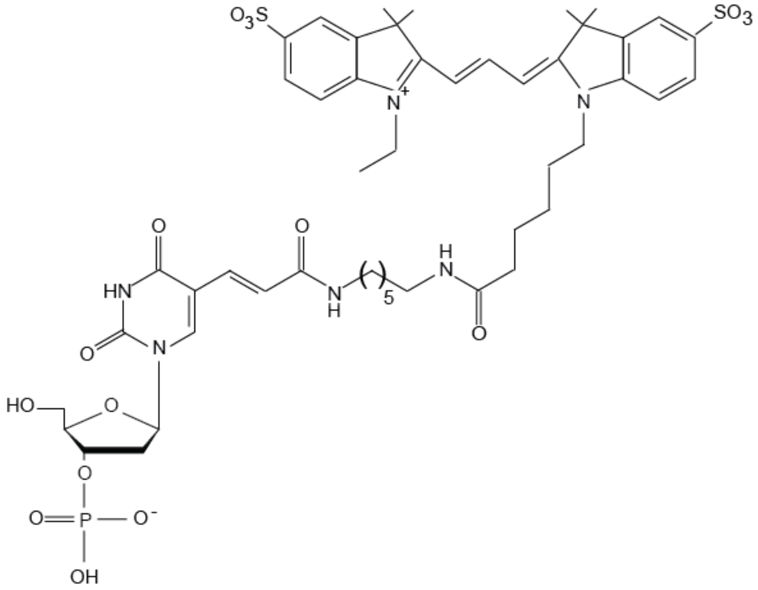

Appendix I - Figure 1. *Functionalization strategy used in the constructs. NHS coupling scheme where a Cy3 molecule is attached to a thymine base via single linker.*

The absorbance of free Cy3 dissolved in aceton nitrile (MeCN) was measured as a reference spectrum for the monomeric state of Cy3. MeCN was used in this case to prevent any possible, partial aggregation of Cy3 in a polar solvent, such as water.

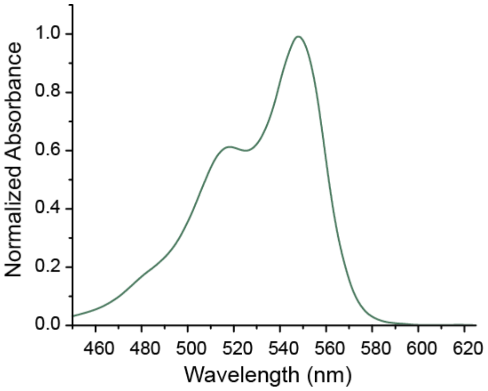

Appendix I - Figure 2 *Absorbance spectrum of free Cy3 in solvent (MeCN).*

Control experiment: Cy3 intercalation in DNA grooves

Since it is known that cyanine dyes can intercalate, as aggregates, in the minor groove of DNA, I performed a control experiment where I mixed free dye with ds-DNA at different ratios. No significant change in the spectrum could be observed, so it can safely be assumed that the H-band appearing in the absorption spectrum of the DNA constructs is not caused by groove intercalation.

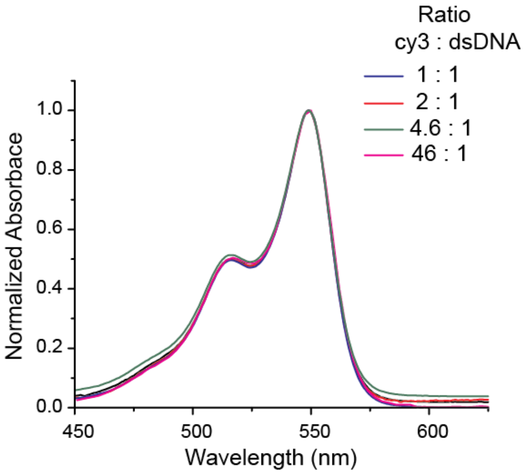

Appendix I - Figure 3. *Absorbance measurements of a mixture of free Cy3 molecules and ds-DNA in 10 mM Tris, 1 mM EDTA and 150 mM NaCl. The ratio between fluorophore and DNA is changed from 1:1 to 46:1 Cy3 to DNA so that the possible intercalation of Cy3 in the DNA groove*[1] *could be excluded from what is observed with the constructs.*

Simulations details

A model system chosen in order to obtain a planar monomer and therefore simplify dimerization was obtained by substituting the $C(CH_3)_2$ groups in the five membered rings with sulfur atoms. This substitution leads to no significant shift of the signal (551 nm in water),[210] and to no change in the overall spectral shape compared to a regular Cy3 monomer. The minimum energy structures was optimized for the ground state and for the excited states S1 and S4 of the monomer and dimer respectively The method used in the calculations is TD-DFT/B3LYP/6-31G(d) in water (PCM), including Grimme's GD3 dispersion correction. Ground state minimum energy structures are shown in Figure S6. Note that the rotation of the monomers by 180 degrees to form the dimer is not of importance here, as the transition dipole moment is located along the molecular axis and therefore the coupling picture according to Molecular Exciton Theory is unchanged. Note further that the frontier orbitals (Figure S7) of the dimer are linear combinations of the frontier orbitals of the monomer.

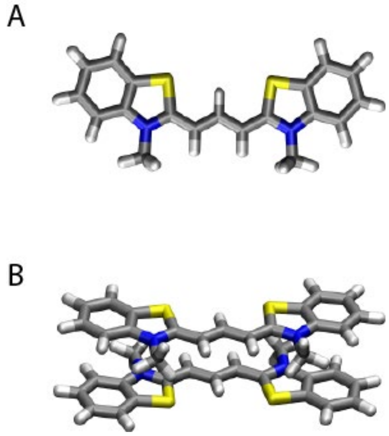

Appendix I - Figure 4. *Optimized molecular structures of the model system for Cy3 with sulfur atoms instead of C(CH3)2 groups in the ground state. Optimized with DFT/B3LYP/6-31G(d) and PCM (water). A) Monomer. B) Dimer consisting of two monomers rotated by 180 degrees at a distance of 3.40 Å. Here, the dispersion correction GD3 from Grimme3 was also used.*

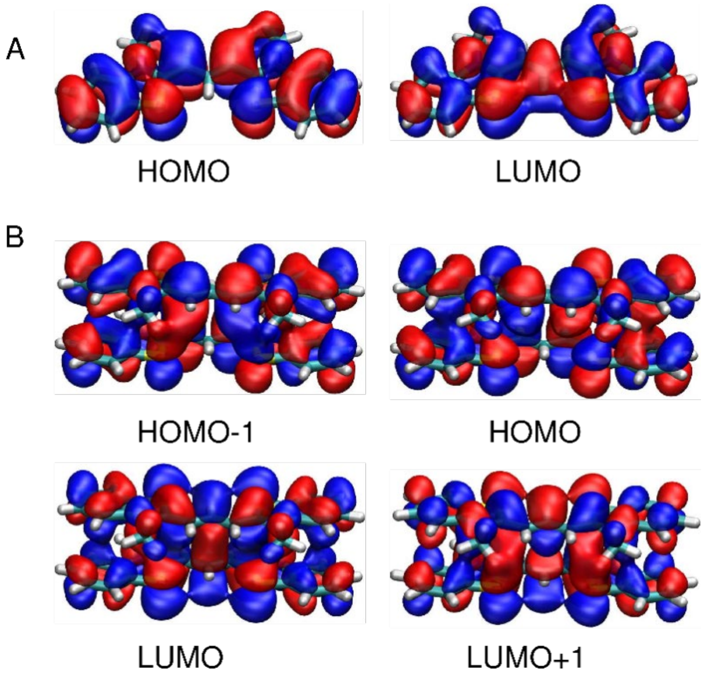

Appendix I - Figure 5. *Molecular orbitals for the Cy3 with sulfur atoms (DFT/B3LYP/6-31G(d)). A) Monomer. B) Dimer.*

	State	*Transition*	*Weight (%)*	*E_{vert} (eV)*	*f*
Monomer	S_1	HOMO -> LUMO	100	2.61	1.6014
Dimer	S_1	HOMO-1 -> LUMO	11	2.18	$< 5*10^{-5}$
		HOMO -> LUMO+1	89		
	S_2	HOMO-1 -> LUMO+1	40	2.22	0.0424
		HOMO -> LUMO	60		
	S_3	HOMO-1 -> LUMO	89	2.43	$< 5*10^{-5}$
		HOMO -> LUMO+1	11		
	S_4	HOMO-1 -> LUMO+1	60	2.80	2.8945
		HOMO -> LUMO	40		

Appendix I - Table 1. *Vertical excitation energies E_{vert}, oscillator strengths f and the involved transitions for the lowest-lying excited states of monomer and stacked dimer obtained with TD-DFT/B3LYP/6-31G(d) in water (PCM). The calculations are performed for a model system with inserted sulfur atoms instead of $C(CH_3)_2$ shown in Supporting Figure S6. For the monomer there is only one excitation of importance with an energy of 2.61 eV. In the case of the dimer only the S_4 state contributes significantly to the absorption and is clearly blue-shifted compared to the monomer with an energy of 2.8 eV. The corresponding orbitals can be seen in figure 5.*

Appendix II

This section contains extra information regarding the DNA origami structure used in the homo-FRET study. Also, single molecule data reported in table 4-4 in chapter 4 are presented as figures. Since single molecule experiments were performed by Anders Barth, co-author of ref. 21, and not by the author of this work, for further information see the associated publication.

DNA origami structure – design and folding

The origami structure consists of a 3-layer block on a square lattice based design. The position of the fluorophores in the structure is marked with a star and all the dyes are by design located on the surface of the origami block. The Cy3 molecule of strand G_2 could not be placed in a perfect line with the other dyes due to the antiparallel nature of DNA strands. In fact, on helix 15 (see Figure S12) the long viral scaffold is on the block surface at the ideal perfect linear alignment with the other dyes. The Cy3 molecule location is consequentially shifted by half helical turn, so that it is located on the origami surface.

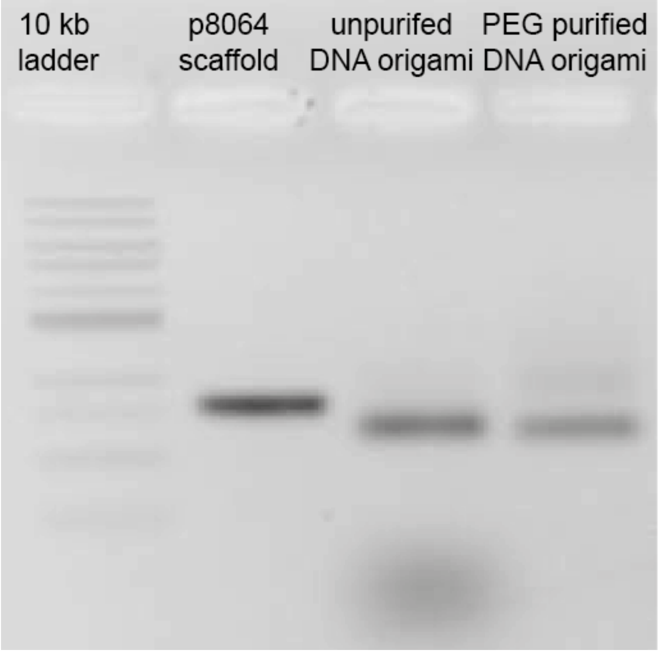

Appendix II - Figure 1 DNA origami gel. *Gel electrophoresis analysis of the DNA origami structure. Labels at the top of each lane describe their content. The gel consists of 1% agarose, in running buffer 10 mM Tris, 1 mM EDTA and 11 mM* $MgCl_2$*. Gel was ran for 2.5 hours at 6.5 V/cm.*

The origami structure was folded by mixing 20 nM ss-DNA scaffold (derived from phage M13 mp18 variant p8064) with a 10X excess sort staple strands (15 to 50 bases long) in 10 mM Tris, 1 mM EDTA and 16 mM $MgCl_2$ buffer. The mixture was annealed with a 16 hour temperature ramp from

65°C to room temperature. The folding of the DNA origami structure was checked by gel electrophoresis (see figure 1). Lane 3 of the gel corresponds to the unpurified structures, the tight band contains the target, folded DNA origami, while the lower “cloud” contains the excess of staples. Lane 4 contains the same DNA origami after two rounds of PEG purification.

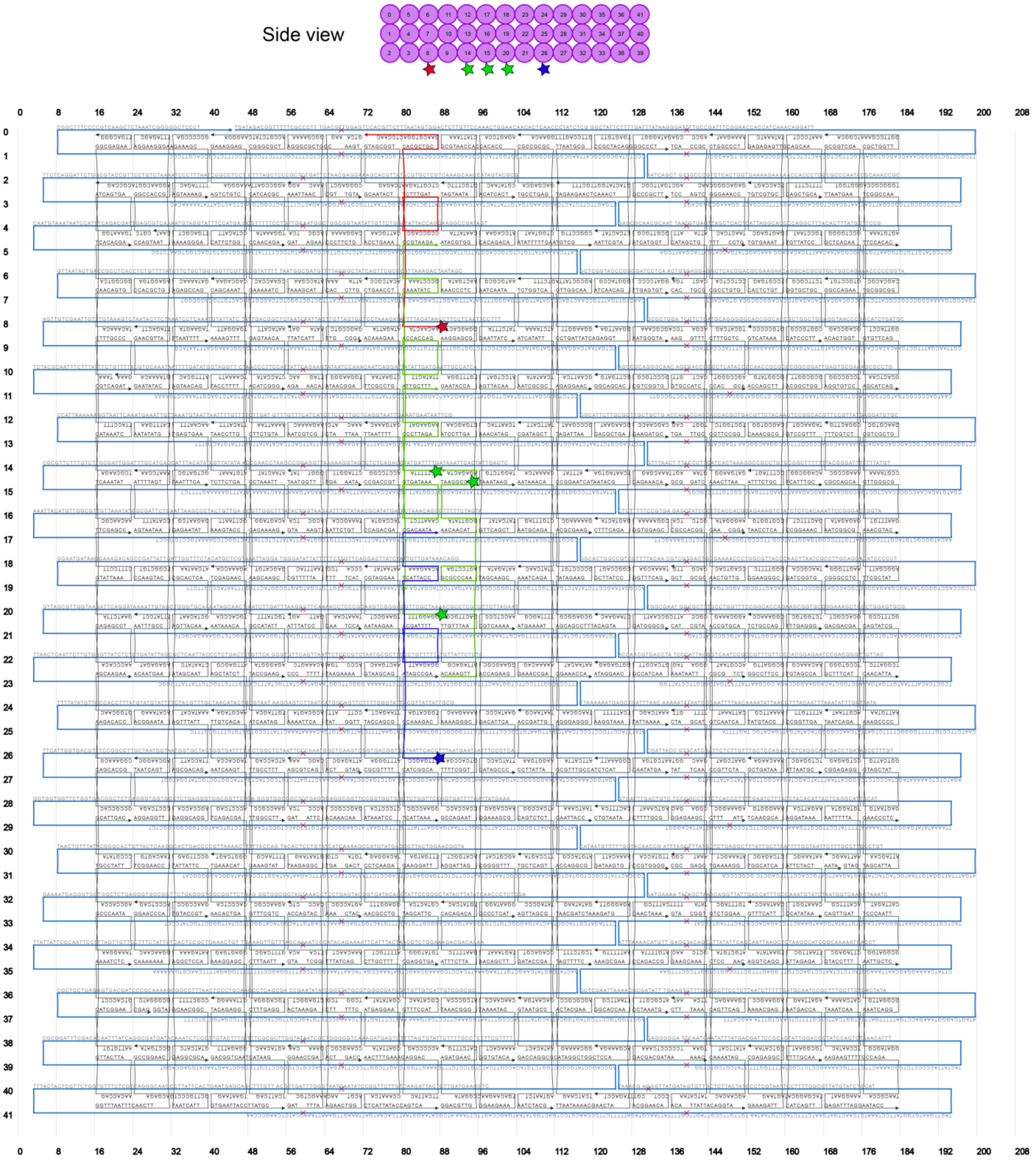

Appendix II - Figure 2. *Design file and DNA sequences of the origami structure from CaDNAno.*[83] *Helixes numbering of the side view drawing correspond to the left and right numbering of the design file. The staples modified with fluorophores are colored according to the spectral characteristics of the dyes (depicted as stars).*

Modified DNA strand

Strands R, G_1, G_3 and B are terminally modified with the desired fluorophore at the 5' end. An additional thymine base, shown as (T) in the table, was added to avoid quenching of fluorophores induced by the proximity with guanine and cytosine bases. Furthermore, fluorophores are known to stack *via* π-interaction of the aromatic rings with the DNA bases especially when DNA is in its double-stranded conformation[159] so the extra base acts also as a local single-stranded DNA to prevent stacking. Strand G_2 is internally modified, meaning Cy3 is linked to a thymine base.

Modified DNA strand	*Name*
cy5- (T)- AACAACTATCTTTGATCCGCCAGCCACGCTGCGAACGTGGACTCCAAC	R
cy3 -(T)-CCTTTTTAACCACCAGTTATACTTCAAATATCGCCCTAAAGCGTAAGA	G_3
ACAAAGTTAGTCCTGAGCGCCCAAGCGTTATATAAGGCGT-cy3-AGAGACTA	G_2
cy3 -(T)-GGAGGTTTGTGATAAACAAATTCTCCCTTAGAAAGAAGATATTGCTTT	G_1
Alexa488- (T)-CTTGAGCCACGATTTTGGAGAATTTCATTACCACAAGAAACGACAATA	B

Appendix II - Table 1. Modified DNA strands. *Strands incorporated in the origami structure to construct the photonic wire. The color coding corresponds to the one used in the design of the DNA origami presented in figure 2.*

Anisotropy measurements

The data points in figure 3 correspond to the signal recorded for each DNA origami structure diffusing through in the focal volume of the laser. To extract anisotropy values reported in table 4-4 a bi-exponential fit was performed as described in Nicoli *et al*.

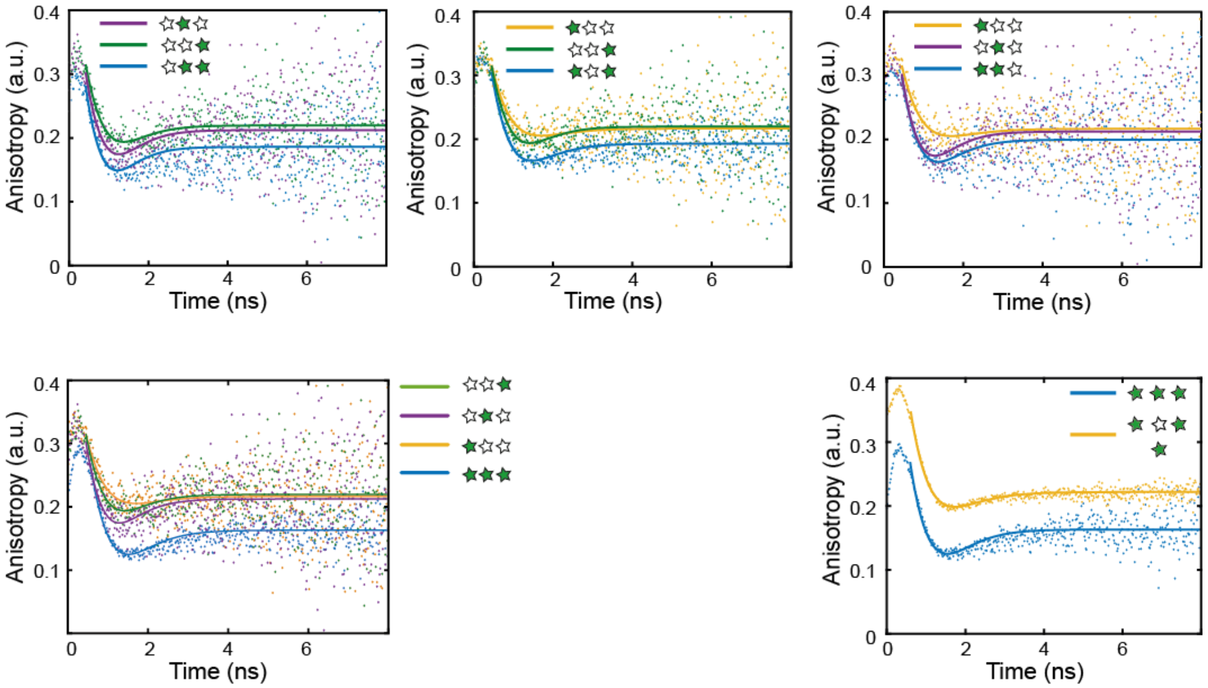

Appendix II - Figure 3. Anisotropy decay. *Time resolved anisotropy decays of Cy3 only labeled structures. Constructs with multiple green dyes are compared with the respective single green-label constructs. In the lower panel (left)* $G_1G_2G_3$ *is compared with a control construct, where all three green dyes are present, but at distances that does not allow any homo-FRET (see scheme of the no homo-FRET construct in chapter 4).*

Appendix III

This section contains extra data and measurements of chapter 6. Theoretical calculations were performed by Boyuan Jin and Christos Argyropoulos as part of a collaborative project.

Spectral Characteristics of QDs and emission measurements from single QDs

I measured the bulk absorption and emission spectra of the QDs functionalized with the respective DNA sequence (see table 1). The absorption measurements were performed using a 10 mm optical path length quartz cuvette (Hellma-analytics) and a V-650 Spectrometer (Jasco) with 1 nm resolution and 1 s/point integration time. Bulk fluorescence measurements were carried out with a cuvette 2 × 10 mm optical path (Hellma-analytics) using a modular spectro-fluorometer Fluorolog3 (Horiba Scientific).

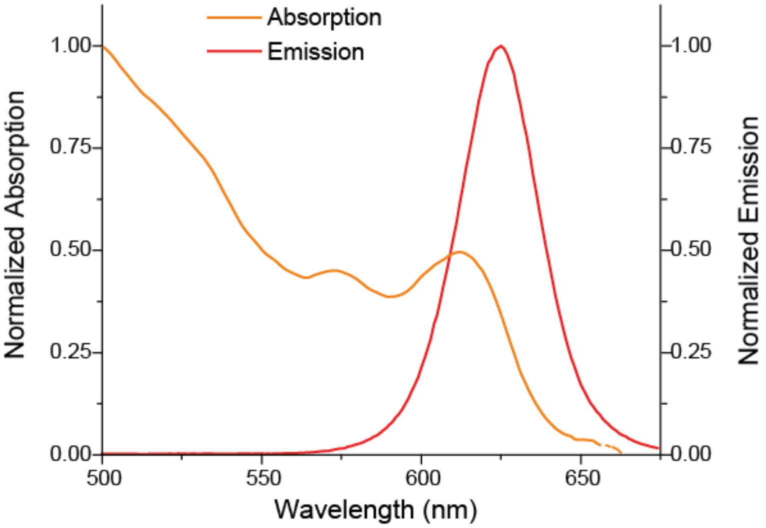

Appendix III - Figure 1. QDs optical properties. *Bulk absorption (orange) and emission (red) spectra of 630-QDs, functionalized with DNA.*

Characterizing single QDs on a surface is challenging, because of the presence of possible contaminants and the collective emission[4] effects of nearby QDs. In order to overcome these challenges, I prepared a series of glass slides with progressively higher dilutions (one order of magnitude per dilution) and observed the changes in the density of fluorescence spots. I analyzed the sample which was diluted enough to show well-spaced fluorescence spots. As a further control, I used an empty glass slide without QDs but exposed to the same conditions (e.g. plasma etching, buffer, washing) and found no detectable fluorescence. All the glass slides were cleaned by sonication in acetone followed by sonication in isopropanol. Right before sample deposition, the surface was further cleaned and charge-activated by oxygen plasma.

Fluorescence Traces Analysis

The analysis of fluorescent traces was performed with a custom-written Matlab script. The movie was imported as a series of 4000 frames; all the frames were added as single matrices and then averaged. The resulting image consists of a 512x512 matrix of doubles and was used to determine the location of fluorescent spots. For each spot an area of 5 by 5 pixels was considered and the background determined as the average of four adjacent areas of also 5 by 5 pixels' size. After determining the location of the signal and the background, the intensity value resulting from the signal minus the background was extracted from the 4000 frames and plotted as a time trace.

Theoretical Calculation

Full-wave three-dimensional simulations of the QD-antennas were performed using the commercial finite-element simulation software COMSOL Multiphysics. The scattering was simulated from the scattered-field formulation, in which we obtained the scattered fields by subtracting them from the analytical solution of an incident plane wave in the absence of the dimer (background field). The field enhancement, shown in Figure S6d in the main paper, was computed at the resonance frequency of the QD-antenna scattering response. The incident excitation wave is always perpendicular to the plane formed by the QD-antenna. The permittivity of gold varies with frequency and is extracted from experiment data.[211] The glass substrate has a refractive index n=1.45.

In general, the fluorescence enhancement factor can be described as the multiplication of several factors computed by theory and experiment and its value is given by the formula:[186] $EF(\bar{r}) = \frac{\eta}{\eta_0}\frac{\gamma_{ex}(\bar{r},\theta)}{\gamma_{ex}^{0}(\bar{r},\theta)}\frac{QY(\bar{r})}{QY_0}$, where η is the emission collection efficiency, γ_{ex} is the excitation rate computed at the excitation frequency of the system (2.21 eV), QY is the quantum yield, $\bar{r}$ is the space vector, and θ is the polar orientation of the emitter's dipole. In the current work, our goal is to compute the trend of fluorescence enhancement to provide some further physical insights to better explain the experimental results presented in the main text. Hence, we use a simplified version of the previously presented fluorescence enhancement formula $\left(\langle EF\rangle \approx \langle \gamma_{ex}/\gamma_{ex}^{0}\rangle \langle QY\rangle\right)$ to compute the trend of the fluorescence enhancement. The quantum yield is defined as: $QY = k_{rad}/(k_{rad}+k_{nrad})$, where k_{rad} and k_{nrad} are the radiative and non-radiative recombination decay rates, respectively. The average $\langle QY\rangle$ can be computed by full-wave simulations where the QD emitter is modelled as a point-dipole with a fixed orientation along the dimer gap.[212] In our simulations, we calculated the Green function originating from the dipole which is assumed to emit monochromatically at the resonance of the gold dimer. The radiative rate can be derived by integrating the power outflow through the boundaries of the simulation domain. The non-radiative rate, on the other hand, is the volume integral of the absorbed power along all the lossy materials. The computed QY for dimers with different gaps is plotted in Figure S5A. The average excitation rate enhancement $\left\langle \gamma_{ex}/\gamma_{ex}^{0} \right\rangle$ is given by the ratio of the maximum field enhancement when the dimer antenna is present over the field enhancement without the antenna computed at the excitation frequency of the system (2.21 eV). The maximum field enhancement is plotted in Figure S5B and is found to be maximum for the 6 nm QD-antenna gap case. When the QY and maximum field enhancement, presented in figures 2A and 2B, respectively, are multiplied, the trend of the average fluorescence enhancement is obtained, as shown in arbitrary units in figure 2C. We clearly demonstrate by full-wave simulations that the maximum fluorescence is expected for a QD-antenna gap thickness equal to 6 nm, similar to the presented experimental results.

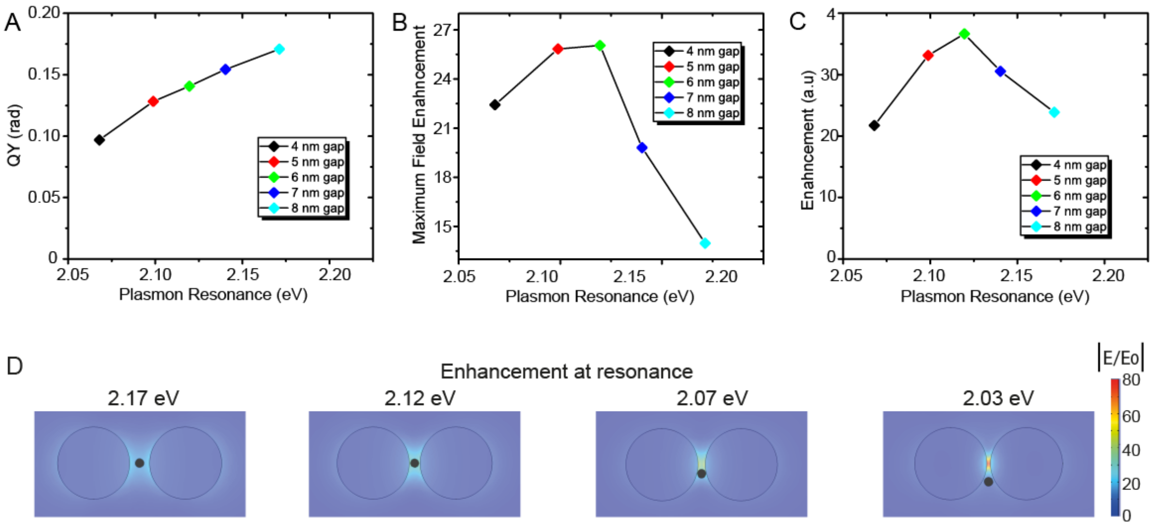

Appendix III - Figure 2. Simulation results of the QD-antenna system for different gaps. *The computed (a) quantum yield (QY), (b) maximum field enhancement at the excitation frequency, and (c) the normalized fluorescence enhancement trend are given in arbitrary units. (d) Calculated electric field enhancement at different plasmon resonances corresponding to nominal gap sizes of 8, 6, 4, and 2 nm (from left to right). The energy of the incident field is 2.21 eV (561 nm), equal to the laser line used in the epifluorescence experiments.*

Control Experiment: AuNPs Dimer Mediated by DNA Origami

Extra data and correlation of the control experiment are presented.

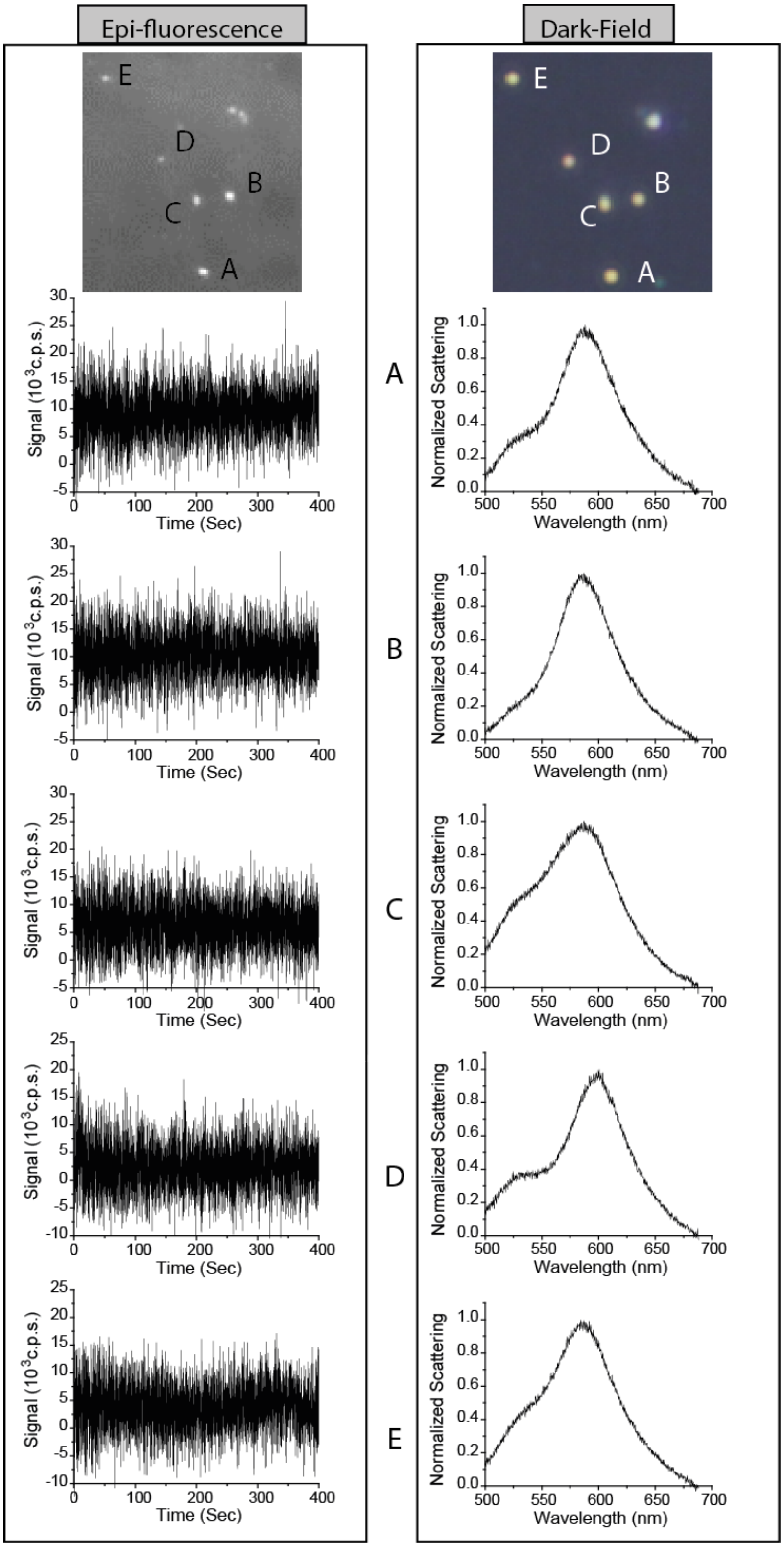

Appendix III - Figure 3. Dimer on DNA origami. *Epi-fluorescence and DF measurements of representative AuNP-origami control structures. Wide-field image accompanied by the corresponding time trace and the scattering spectrum of each individual structure.*

DNA Sequences

DNA was purchased from Eurofins genomics LLC unless otherwise indicated. Strands used for NP functionalization can be divided into three segments: a functional group or sequence attached to the NP (red), a hybridization sequence (black), and a DNA spacer (green). Lower letters indicate phosphothiolated (PTO) bases and SH-C6 is a thiol- 6 carbon linker.

Nanoparticle	**DNA sequence 5' to 3'**
40 nm Au and 40 nm Ag	SH-C6 TT CTC TAC CAC CTA CAT
5 nm Au	ATG TAG GTG GTA GAG AA cgg gcg tgc
QD	ATG TAG GTG GTA GAG AA GGG GGG GGG

Table S2: DNA sequences used to functionalize AuNPs and QDs displaying the functional group or sequence attached to the NP (red), hybridization sequence (black), and DNA spacer (green).

Sample purification and TEM imaging of antennas

The QD-antennas fabricated with conventional AuNPs or ultrasmooth spherical NPs were assembled by mixing a 1:5 QD:AuNPs ratio in 1xTE with 5.5 mM Mg^{2+} buffer (40 mM Tris, 1 mM EDTA and 5.5 mM $MgCl_2$). The samples were then purified using gel electrophoresis and extracted from the band corresponding to the Au-QD-Au construct (see figure 4). TEM imaging was performed as described earlier.

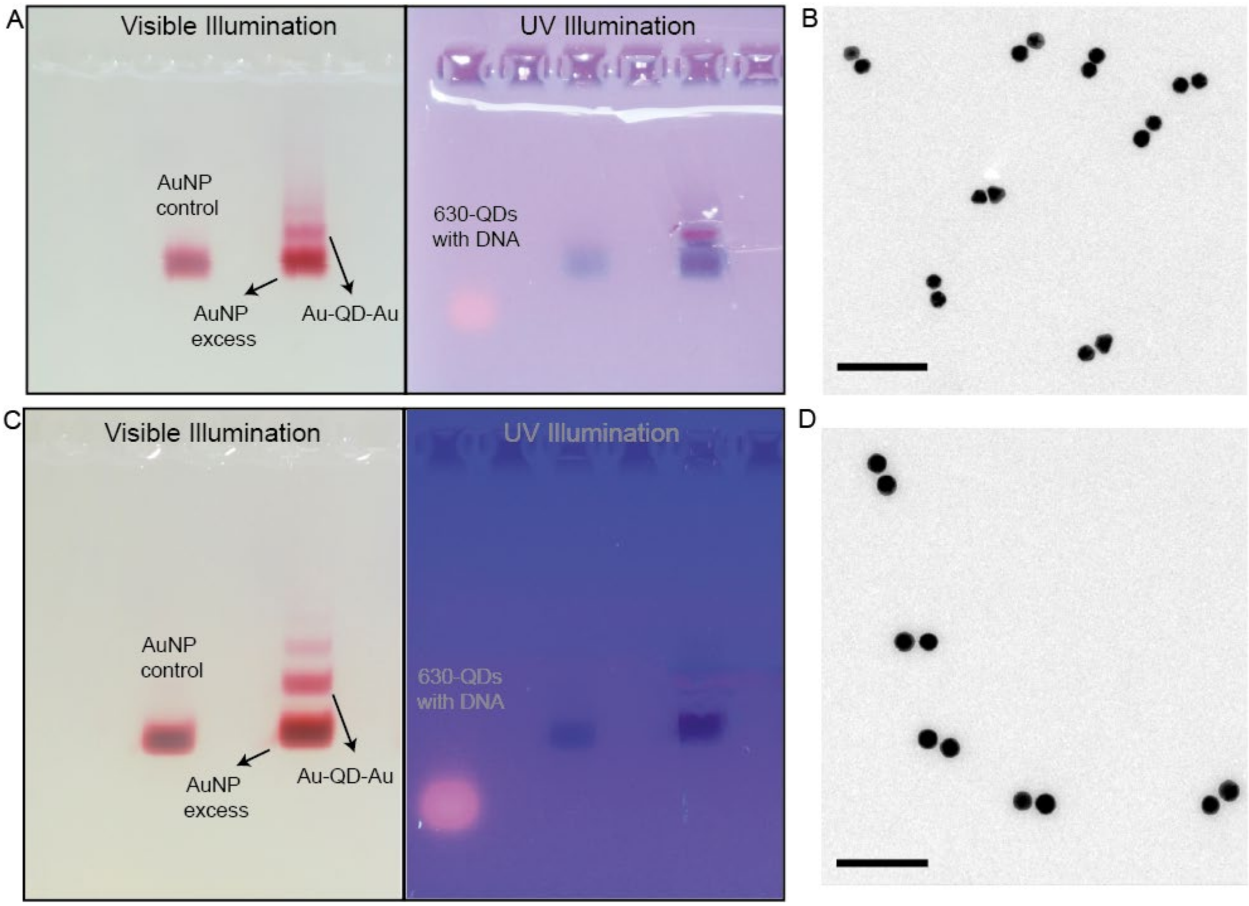

Appendix III - Figure 4. Gel purification and TEM imaging of the sample. *(a) Images of the gel taken with visible light (left) and UV light (right). The gold dimer band is visible with regular ambient light thanks to the red color of commercial AuNPs. The fluorescence from QDs band (control lane) is visible only under UV illumination. (b) TEM image of QD-antennas with commercial AuNPs. (c) and (d) same as a) and b) with ultrasmooth spherical NPs. In TEM images, due to high contrast of AuNPs it is challenging to see the QDs.*

Correlation of all structures measured

All data shown in figure 6-9 is correlated by superimposing fluorescence and dark-field images, as described in chapter 6. Each individual structure made with conventional AuNPs is additionally correlated with SEM imaging (see figure 6) to ensure that all reported structures are dimers. In some limited occasions, SEM revealed that the structure of interest corresponded to individual triangles, trimers, or two closely spaced dimers. On the other hand, antennas fabricated using ultrasmooth spherical AuNPs displayed a consistent plasmon resonance which together with polarization measurements is enough to ensure that the structure corresponds to a well-formed individual dimer (figure 5). The scale bars in the SEM images correspond to 80 nm.

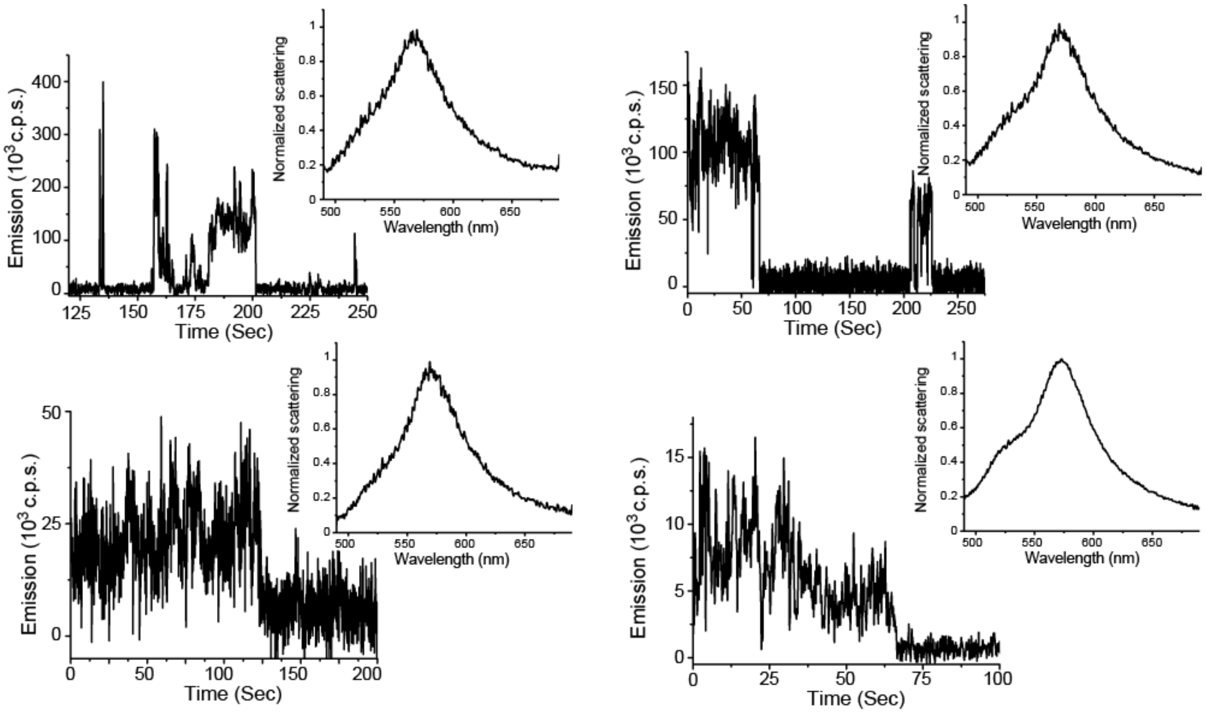

Appendix III - Figure 5. Measurement of all antennas fabricated with ultrasmooth spherical NPs. *Epi-fluorescence traces of each ultrasmooth spherical AuNPs antenna measured, with the respective plasmon scattering signal.*

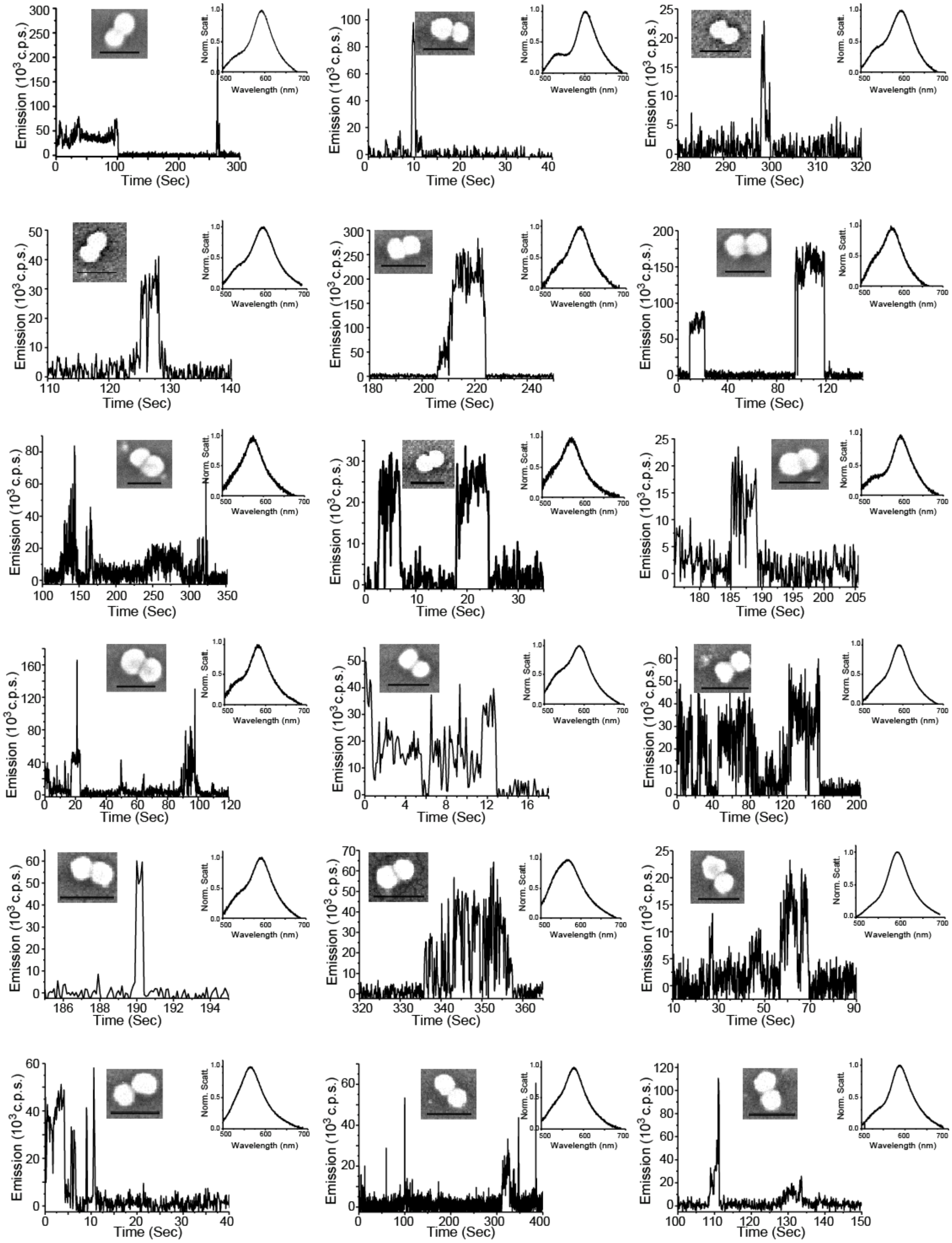

Appendix III - Figure 6. Measurements of all antennas fabricated with conventional AuNPs. *Epi-fluorescence traces of each structure measured, with its respective plasmon scattering and SEM image (scale bar 100 nm).*

Assembly with Silver NPs

To test the flexibility of the assembly approach, I fabricated QD-antennas with silver (Ag) NPs and a 490 nm emission QD (figure 7). AgNPs poses a more intrinsic variability than their AuNP counterparts.

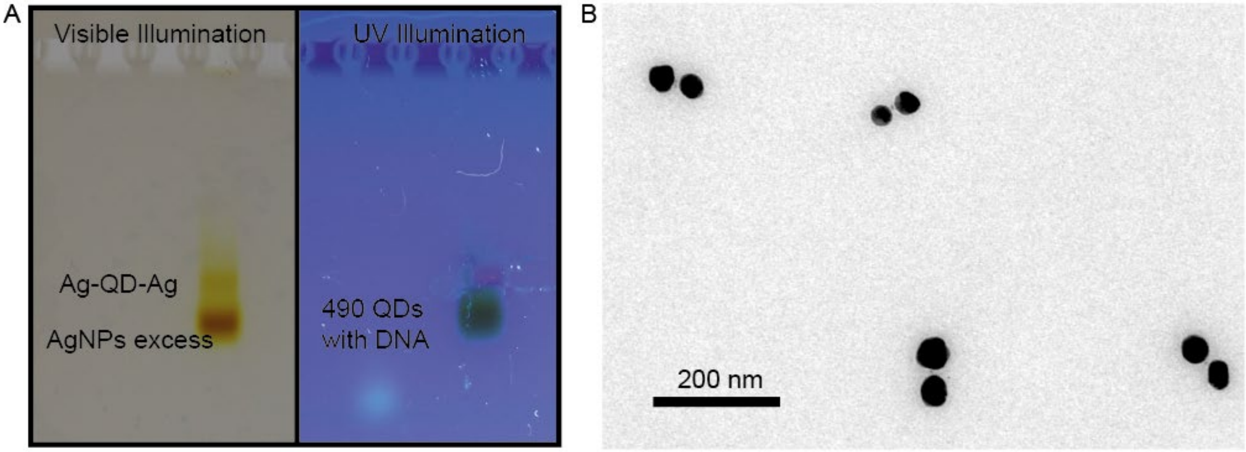

Appendix III - Figure 7. QD-silver antennas. *Gel purification and TEM imaging of silver antennas. (a) Images of the gel taken with visible light (left) and UV light (right). (b) TEM image of QD-Ag Antennas. Since silver has a lower contrast under TEM than AuNPs, it is easier to observe the QDs between the NPs.*

Table of figures

Bibliography

(1) Myroshnychenko, V.; Rodríguez-Fernández, J.; Pastoriza-Santos, I.; Funston, A. M.; Novo, C.; Mulvaney, P.; Liz-Marzán, L. M.; García De Abajo, F. J. Modelling the Optical Response of Gold Nanoparticles. *Chem. Soc. Rev.* **2008**, *37* (9), 1792–1805.

(2) Alivisatos, A. P. Semiconductor Clusters, Nanocrystals, and Quantum Dots. *Science (80-.).* **1996**, *271* (5251), 933–937.

(3) Valeur, B. *Molecular Fluorescence*; Wiley-VCH Verlag GmbH: Weinheim, FRG, 2001; Vol. 8.

(4) Scheibner, M.; Schmidt, T.; Worschech, L.; Forchel, A.; Bacher, G.; Passow, T.; Hommel, D. Superradiance of Quantum Dots. *Nat. Phys.* **2007**, *3* (2), 106–110.

(5) Lodahl, P.; Mahmoodian, S.; Stobbe, S. Interfacing Single Photons and Single Quantum Dots with Photonic Nanostructures. *Rev. Mod. Phys.* **2015**, *87* (2), 347–400.

(6) Seeman, N. C. DNA in a Material World. *Nature* **2003**, *421* (6921), 427–431.

(7) Seeman, N. C.; Sleiman, H. F. DNA Nanotechnology. *Nat. Rev. Mater.* **2017**, *3*.

(8) Tan, S. J.; Campolongo, M. J.; Luo, D.; Cheng, W. Building Plasmonic Nanostructures with DNA. *Nat. Nanotechnol.* **2011**, *6* (5), 268–276.

(9) Pilo-Pais, M.; Acuna, G. P.; Tinnefeld, P.; Liedl, T. Sculpting Light by Arranging Optical Components with DNA Nanostructures. *MRS Bull.* **2017**, *42* (12), 936–942.

(10) Liu, N.; Liedl, T. DNA-Assembled Advanced Plasmonic Architectures. *Chem. Rev.* **2018**, *118* (6), 3032–3053.

(11) Mirkovic, T.; Ostroumov, E. E.; Anna, J. M.; Van Grondelle, R.; Govindjee; Scholes, G. D. Light Absorption and Energy Transfer in the Antenna Complexes of Photosynthetic Organisms. *Chem. Rev.* **2017**, *117* (2), 249–293.

(12) Scholes, G. D.; Fleming, G. R.; Olaya-Castro, A.; van Grondelle, R. Lessons from Nature about Solar Light Harvesting. *Nat. Chem.* **2011**, *3* (10), 763–774.

(13) Croce, R.; Van Amerongen, H. Natural Strategies for Photosynthetic Light Harvesting. *Nat. Chem. Biol.* **2014**, *10* (7), 492–501.

(14) Cheng, Y.-C.; Fleming, G. R. Dynamics of Light Harvesting in Photosynthesis. *Annu. Rev. Phys. Chem.* **2009**, *60* (1), 241–262.

(15) Scholes, G. D. Long-Range Resonance Energy Transfer in Molecular Systems. *Annu. Rev. Phys. Chem.* **2003**, *54* (1), 57–87.

(16) Fleming, G. R.; Grondelle, R. van. Femtosecond Spectroscopy of Photosynthetic Light-Harvesting Systems. *Curr. Opin. Struct. Biol.* **1997**, *7* (5), 738–748.

(17) Trinkunas, G.; Herek, J. L.; Polívka, T.; Sundström, V.; Pullerits, T. Exciton Delocalization Probed by Excitation Annihilation in the Light-Harvesting Atenna LH2. *Phys. Rev. Lett.* **2001**, *86* (18), 4167–4170.

(18) Hu, X.; Damjanovic, A.; Ritz, T.; Schulten, K. Architecture and Mechanism of the Light-Harvesting Apparatus of Purple Bacteria. *Proc. Natl. Acad. Sci.* **1998**, *95* (11), 5935–5941.

(19) van Amerongen, H.; Croce, R. Light Harvesting in Photosystem II. *Photosynth. Res.* **2013**, *116* (2–3), 251–263.

(20) Nicoli, F.; Roos, M. K.; Hemmig, E. A.; Di Antonio, M.; de Vivie-Riedle, R.; Liedl, T. Proximity-Induced H-Aggregation of Cyanine Dyes on DNA-Duplexes. *J. Phys. Chem. A* **2016**, *120* (50), 9941–9947.

(21) Nicoli, F.; Barth, A.; Bae, W.; Neukirchinger, F.; Crevenna, A. H.; Lamb, D. C.; Liedl, T. Directional Photonic Wire Mediated by Homo-Förster Resonance Energy Transfer on a DNA Origami Platform. *ACS Nano* **2017**, *11* (11), 11264–11272.

(22) Gramotnev, D. K.; Bozhevolnyi, S. I. Nanofocusing of Electromagnetic Radiation. *Nat. Photonics* **2014**, *8* (1), 13–22.

(23) Kelly, K. L.; Coronado, E.; Zhao, L. L.; Schatz, G. C. The Optical Properties of Metal Nanoparticles: The Influence of Size, Shape, and Dielectric Environment. *J. Phys. Chem. B* **2003**, *107* (3), 668–677.

(24) Brongersma, M. L. Plasmonics: Engineering Optical Nanoantennas. *Nat. Photonics* **2008**, *2* (5), 270–272.

(25) Xin, H.; Namgung, B.; Lee, L. P. Nanoplasmonic Optical Antennas for Life Sciences and Medicine. *Nat. Rev. Mater.* **2018**.

(26) Rechberger, W.; Hohenau, A.; Leitner, A.; Krenn, J. R.; Lamprecht, B.; Aussenegg, F. R. Optical Properties of Two Interacting Gold Nanoparticles. *Opt. Commun.* **2003**, *220* (1–3), 137–141.

(27) Hugall, J. T.; Singh, A.; Van Hulst, N. F. Plasmonic Cavity Coupling. *ACS Photonics* **2018**, *5* (1), 43–53.

(28) Giannini, V.; Fernández-Domínguez, A. I.; Heck, S. C.; Maier, S. A. Plasmonic Nanoantennas: Fundamentals and Their Use in Controlling the Radiative Properties of Nanoemitters. *Chem. Rev.* **2011**, *111* (6), 3888–3912.

(29) Cao, E.; Lin, W.; Sun, M.; Liang, W.; Song, Y. Exciton-Plasmon Coupling Interactions: From Principle to Applications. *Nanophotonics* **2018**, *7* (1), 145–167.

(30) Pelton, M. Modified Spontaneous Emission in Nanophotonic Structures. *Nat. Photonics* **2015**, *9* (7), 427–435.

(31) Zhang, T.; Nicoli, F.; Pilo-Pais, M.; Liedl, T. Facile and Fast DNA-Functionalization of Quantum Dots Using Purine Nucleotide-ZnS Affinity. *J. Am. Chem. Soc.* **2018**, No. under review.

(32) Nicoli, F.; Zhang, T.; Jin, B.; Selbach, F.; Argyropoulos, C.; Liedl, T.; Pilo-Pais, M. DNA Mediated Self-Assembly of Plasmonic Antennas with a Single Quantum Dot in the Hot Spot. *ACS Nano* **2018**, No. under review.

(33) Lakowicz, J. R. *Principles of Fluorescence Spectroscopy*; Lakowicz, J. R., Ed.; Springer US: Boston, MA, 2006.

(34) Markus, S.; Johan, H.; Jörg, E. Handbook of Fluorescence Spectroscopy and Imaging. *Angew. Chemie Int. Ed.* **2011**, *50* (39), 9017–9018.

(35) Fox, M. Quantum Optics. *Univ. Oxford* **2013**, *53* (9), 1689–1699.

(36) Novotny, L.; Hecht, B. *Principles of Nano-Optics*; Cambridge University Press, 2006.

(37) Medintz, I.; Hildebrandt, N. *FRET - Förster Resonance Energy Transfer*; Medintz, I., Hildebrandt, N., Eds.; Wiley-VCH Verlag GmbH & Co. KGaA: Weinheim, Germany, 2013.

(38) Förster, T. Energy Migration and Fluorescence. *J. Biomed. Opt.* **2012**, *17* (1), 011002.

(39) Bransden, B. H.; Joachim, C. J. *Quantum Mechanics*, Second edi.; Pearson Education Limited, 2000.

(40) Smith, A. M.; Nie, S. Semiconductor Nanocrystals: Structure, Properties, and Band Gap Engineering. *Acc Chem Res.* **2010**, *43*, 190–200.

(41) Davies, J. H. John H. . *The Physics of Low-Dimensional Semiconductors : An Introduction*; Cambridge University Press, 1998.

(42) Algar, W. R.; Susumu, K.; Delehanty, J. B.; Medintz, I. L. Semiconductor Quantum Dots in Bioanalysis: Crossing the Valley of Death. *Anal. Chem.* **2011**, *83* (23), 8826–8837.

(43) Reiss, P.; Protière, M.; Li, L. Core/Shell Semiconductor Nanocrystals. *Small* **2009**, *5* (2), 154–168.

(44) Kuhn, H. A Quantum Mechanical Theory of Light Absorption of Organic Dyes and Similar Compounds. *J. Chem. Phys.* **1949**, *17* (12), 1198–1212.

(45) Hamer, N. I. F. and F. M. A Comparison of the Absorption Spectra of Some Typical Symmetrical Cyanine Dyes. *Procy Londoneedings R. Soc.* **1936**, *154* (883), 703–723.

(46) Maier, S. A. *Plasmonics: Fundamentals and Applications*; Springer US: New York, NY, 2007; Vol. 677.

(47) Modern Plasmonics. In *Modern Plasmonics*; Richardson, N. V, Holloway, S., Eds.; Handbook of Surface Science; North-Holland, 2014; Vol. 4, p i.

(48) Pelton, M.; Bryant, G. *Introduction to Metal-Nanoparticle Plasmonics*; Wiley-VCH Verlag GmbH & Co. KGaA, 2013.

(49) Pelton, M.; Aizpurua, J.; Bryant, G. Metal-Nanoparticle Plasmonics. *Laser Photonics Rev.* **2008**, *2* (3), 136–159.

(50) Gramotnev, D. K.; Bozhevolnyi, S. I. Plasmonics beyond the Diffraction Limit. *Nat. Photonics* **2010**, *4* (2), 83–91.

(51) Schuller, J. A.; Barnard, E. S.; Cai, W.; Jun, Y. C.; White, J. S.; Brongersma, M. L. Plasmonics for Extreme Light Concentration and Manipulation. *Nat. Mater.* **2010**, *9* (3), 193–204.

(52) Juan, M. L.; Righini, M.; Quidant, R. Plasmon Nano-Optical Tweezers. *Nat. Photonics* **2011**, *5* (6), 349–356.

(53) Puchkova, A.; Vietz, C.; Pibiri, E.; Wünsch, B.; Sanz Paz, M.; Acuna, G. P.; Tinnefeld, P. DNA Origami Nanoantennas with over 5000-Fold Fluorescence Enhancement and Single-Molecule Detection at 25 MM. *Nano Lett.* **2015**, *15* (12), 8354–8359.

(54) Lim, D.-K.; Jeon, K.-S.; Kim, H. M.; Nam, J.-M.; Suh, Y. D. Nanogap-Engineerable Raman-Active Nanodumbbells for Single-Molecule Detection. *Nat. Mater.* **2010**, *9* (1), 60–67.

(55) Gómez, D. E.; Roberts, A.; Davis, T. J.; Vernon, K. C. Surface Plasmon Hybridization and Exciton Coupling. *Phys. Rev. B* **2012**, *86* (3), 035411.

(56) Tame, M. S.; McEnery, K. R.; Özdemir, Ş. K.; Lee, J.; Maier, S. A.; Kim, M. S. Quantum Plasmonics. *Nat. Phys.* **2013**, *9* (6), 329–340.

(57) Anger, P.; Bharadwaj, P.; Novotny, L. Enhancement and Quenching of Single-Molecule Fluorescence. *Phys. Rev. Lett.* **2006**, *96* (11), 113002.

(58) Akselrod, G. M.; Argyropoulos, C.; Hoang, T. B.; Ciracì, C.; Fang, C.; Huang, J.; Smith, D. R.; Mikkelsen, M. H. Probing the Mechanisms of Large Purcell Enhancement in Plasmonic Nanoantennas. *Nat. Photonics* **2014**, *8* (11), 835–840.

(59) Totzeck, M.; Ulrich, W.; Göhnermeier, a.; Kaiser, W. Pushing Deep Ultraviolet Lithography to Its Limits. *Nat. Photon.* **2007**, *1* (November), 629–631.

(60) Engstrom, D. S.; Porter, B.; Pacios, M.; Bhaskaran, H. Additive Nanomanufacturing - A Review. *J. Mater. Res.* **2014**, *29* (17), 1792–1816.

(61) Gwo, S.; Chen, H. Y.; Lin, M. H.; Sun, L.; Li, X. Nanomanipulation and Controlled Self-Assembly of Metal Nanoparticles and Nanocrystals for Plasmonics. *Chem. Soc. Rev.* **2016**, *45* (20), 5672–5716.

(62) Jones, M. R.; Osberg, K. D.; MacFarlane, R. J.; Langille, M. R.; Mirkin, C. A. Templated Techniques for the Synthesis and Assembly of Plasmonic Nanostructures. *Chem. Rev.* **2011**, *111* (6), 3736–3827.

(63) Seeman, N. C. Nucleic Acid Junctions and Lattices. *J. Theor. Biol.* **1982**, *99* (2), 237–247.

(64) Chen, J.; Seeman, N. C. Synthesis from DNA of a Molecule with the Connectivity of a Cube. *Nature* **1991**, *350* (6319), 631–633.

(65) Bathe, M.; Rothemund, P. W. K. DNA Nanotechnology: A Foundation for Programmable Nanoscale Materials. *MRS Bull.* **2017**, *42* (12), 882–888.

(66) Seeman, N. C. *Structural DNA Nanotechnology*; Cambridge University Press: Cambridge, 2015.

(67) Luo, D.; Schricker, S. R. *Handbook of Nanomaterials Properties*; Bhushan, B., Luo, D., Schricker, S. R., Sigmund, W., Zauscher, S., Eds.; Springer Berlin Heidelberg: Berlin, Heidelberg, 2014.

(68) Watson, J.; Crick, F. Molecular Structure of Nucleic Acids. *Nature.* **1953**, *171* (4356), 737–738.

(69) Yakovchuk, P.; Protozanova, E.; Frank-Kamenetskii, M. D. Base-Stacking and Base-Pairing Contributions into Thermal Stability of the DNA Double Helix. *Nucleic Acids Res.* **2006**, *34* (2), 564–574.

(70) Breslauer, K. J.; Frank, R.; Blocker, H.; Marky, L. A. Predicting DNA Duplex Stability from the Base Sequence. *Proc. Natl. Acad. Sci.* **1986**, *83* (11), 3746–3750.

(71) Hunter, C. A. Sequence-Dependent DNA Structure. *BioEssays*. 1996, pp 157–162.

(72) SantaLucia, J. A Unified View of Polymer, Dumbbell, and Oligonucleotide DNA Nearest-Neighbor Thermodynamics. *Proc. Natl. Acad. Sci.* **1998**, *95* (4), 1460–1465.

(73) Howard, K. P. Thermodynamics of DNA Duplex Formation: A Biophysical Chemistry Laboratory Experiment. *J. Chem. Educ.* **2000**, *77* (11), 1469.

(74) Schildkraut, C.; Lifson, S. Dependence of the Melting Temperature of DNA on Salt Concentration. *Biopolymers* **1965**, *3* (2), 195–208.

(75) Wang, P.; Chatterjee, G.; Yan, H.; Labean, T. H.; Turberfield, A. J.; Castro, C. E.; Seelig, G.; Ke, Y. Practical Aspects of Structural and Dynamic DNA Nanotechnology. *MRS Bull.* **2017**, *42* (12), 889–896.

(76) Tinland, B.; Pluen, A.; Sturm, J.; Weill, G. Persistence Length of Single-Stranded DNA. *Macromolecules* **1997**, *30* (19), 5763–5765.

(77) Liedl, T.; Högberg, B.; Tytell, J.; Ingber, D. E.; Shih, W. M. Self-Assembly of Three-Dimensional Prestressed Tensegrity Structures from DNA. *Nat. Nanotechnol.* **2010**, *5* (7), 520–524.

(78) Kallenbach, N. R.; Ma, R. I.; Seeman, N. C. An Immobile Nucleic Acid Junction Constructed from Oligonucleotides. *Nature*. 1983, pp 829–831.

(79) Seeman, N. Nucleic Acid Nanostructures and Topology. *Angew. Chemie Int. Ed.* **1998**, *37*, 3220–3238.

(80) Li, X.; Yang, X.; Qi, J.; Seeman, N. C. Antiparallel DNA Double Crossover Molecules as Components for Nanoconstruction. *J. Am. Chem. Soc.* **1996**, *118* (26), 6131–6140.

(81) Winfree, E.; Liu, F.; Wenzler, L. A.; Seeman, N. C. Design and Self-Assembly of Two-Dimensional DNA Crystals. *Nature* **1998**, *394* (6693), 539–544.

(82) Rothemund, P. W. K. Folding DNA to Create Nanoscale Shapes and Patterns. *Nature* **2006**, *440* (7082), 297–302.

(83) Douglas, S. M.; Marblestone, A. H.; Teerapittayanon, S.; Vazquez, A.; Church, G. M.; Shih, W. M. Rapid Prototyping of 3D DNA-Origami Shapes with CaDNAno. *Nucleic Acids Res.* **2009**, *37* (15), 5001–5006.

(84) Castro, C. E.; Kilchherr, F.; Kim, D. N.; Shiao, E. L.; Wauer, T.; Wortmann, P.; Bathe, M.; Dietz, H. A Primer to Scaffolded DNA Origami. *Nat. Methods* **2011**, *8* (3), 221–229.

(85) Douglas, S. M.; Dietz, H.; Liedl, T.; Högberg, B.; Graf, F.; Shih, W. M. Self-Assembly of DNA into Nanoscale Three-Dimensional Shapes. *Nature* **2009**, *459* (7245), 414–418.

(86) Dietz, H.; Douglas, S. M.; Shih, W. M. Folding DNA into Twisted and Curved Nanoscale Shapes. *Science (80-.).* **2009**, *325* (5941), 725–730.

(87) Zhang, T.; Hartl, C.; Frank, K.; Heuer-Jungemann, A.; Fischer, S.; Nickels, P. C.; Nickel, B.; Liedl, T. 3D DNA Origami Crystals. *Adv. Mater.* **2018**, *1800273*, 1–6.

(88) Young, K. L.; Ross, M. B.; Blaber, M. G.; Rycenga, M.; Jones, M. R.; Zhang, C.; Senesi, A. J.; Lee, B.; Schatz, G. C.; Mirkin, C. A. Using DNA to Design Plasmonic Metamaterials with Tunable Optical Properties. *Adv. Mater.* **2014**, *26* (4), 653–659.

(89) Kuzyk, A.; Jungmann, R.; Acuna, G. P.; Liu, N. DNA Origami Route for Nanophotonics. *ACS Photonics* **2018**, *5* (4), 1151–1163.

(90) Zhang, C.; MacFarlane, R. J.; Young, K. L.; Choi, C. H. J.; Hao, L.; Auyeung, E.; Liu, G.; Zhou, X.; Mirkin, C. A. A General Approach to DNA-Programmable Atom Equivalents. *Nat. Mater.* **2013**, *12* (8), 741–746.

(91) Jones, M. R.; Seeman, N. C.; Mirkin, C. A. Programmable Materials and the Nature of the DNA Bond. *Science (80-.).* **2015**, *347* (6224).

(92) Kuzyk, A.; Schreiber, R.; Fan, Z.; Pardatscher, G.; Roller, E. M.; Högele, A.; Simmel, F. C.; Govorov, A. O.; Liedl, T. DNA-Based Self-Assembly of Chiral Plasmonic Nanostructures with Tailored Optical Response. *Nature* **2012**, *483* (7389), 311–314.

(93) Roller, E. M.; Khorashad, L. K.; Fedoruk, M.; Schreiber, R.; Govorov, A. O.; Liedl, T. DNA-Assembled Nanoparticle Rings Exhibit Electric and Magnetic Resonances at Visible Frequencies. *Nano Lett.* **2015**, *15* (2), 1368–1373.

(94) Klein, W. P.; Schmidt, C. N.; Rapp, B.; Takabayashi, S.; Knowlton, W. B.; Lee, J.; Yurke, B.; Hughes, W. L.; Graugnard, E.; Kuang, W. Multiscaffold DNA Origami Nanoparticle Waveguides. *Nano Lett.* **2013**, *13* (8), 3850–3856.

(95) Kuzyk, A.; Schreiber, R.; Zhang, H.; Govorov, A. O.; Liedl, T.; Liu, N. Reconfigurable 3D Plasmonic Metamolecules. *Nat. Mater.* **2014**, *13* (9), 862–866.

(96) Schreiber, R.; Do, J.; Roller, E.-M.; Zhang, T.; Schüller, V. J.; Nickels, P. C.; Feldmann, J.; Liedl, T. Hierarchical Assembly of Metal Nanoparticles, Quantum Dots and Organic Dyes Using DNA Origami Scaffolds. *Nat. Nanotechnol.* **2013**, *9* (1), 74–78.

(97) Albinsson, B.; Hannestad, J. K.; Börjesson, K. Functionalized DNA Nanostructures for Light Harvesting and Charge Separation. *Coord. Chem. Rev.* **2012**, *256* (21–22), 2399–2413.

(98) Díaz, S. A.; Buckhout-White, S.; Ancona, M. G.; Spillmann, C. M.; Goldman, E. R.; Melinger, J. S.; Medintz, I. L. Extending DNA-Based Molecular Photonic Wires with Homogeneous Förster Resonance Energy Transfer. *Adv. Opt. Mater.* **2016**, n/a-n/a.

(99) Dutta, P. K.; Varghese, R.; Nangreave, J.; Lin, S.; Yan, H.; Liu, Y. DNA-Directed Artificial Light-Harvesting Antenna. *J. Am. Chem. Soc.* **2011**, *133* (31), 11985–11993.

(100) Hemmig, E. A.; Creatore, C.; Wünsch, B.; Hecker, L.; Mair, P.; Parker, M. A.; Emmott, S.; Tinnefeld, P.; Keyser, U. F.; Chin, A. W. Programming Light-Harvesting Efficiency Using DNA Origami. *Nano Lett.* **2016**, *16* (4), 2369–2374.

(101) Cannon, B. L.; Kellis, D. L.; Davis, P. H.; Lee, J.; Kuang, W.; Hughes, W. L.; Graugnard, E.; Yurke, B.; Knowlton, W. B. Excitonic AND Logic Gates on DNA Brick Nanobreadboards. *ACS Photonics* **2015**, *2* (3), 398–404.

(102) Schnitzbauer, J.; Strauss, M. T.; Schlichthaerle, T.; Schueder, F.; Jungmann, R. Super-Resolution Microscopy with DNA-PAINT. *Nat. Protoc.* **2017**, *12* (6), 1198–1228.

(103) Blythe, K. L.; Willets, K. A. Super-Resolution Imaging of Fluorophore-Labeled DNA Bound to Gold Nanoparticles: A Single-Molecule, Single-Particle Approach. *J. Phys. Chem. C* **2016**, *120* (2), 803–815.

(104) Bidault, S.; Devilez, A.; Maillard, V.; Lermusiaux, L.; Guigner, J. M.; Bonod, N.; Wenger, J. Picosecond Lifetimes with High Quantum Yields from Single-Photon-Emitting Colloidal Nanostructures at Room Temperature. *ACS Nano* **2016**, *10* (4), 4806–4815.

(105) Busson, M. P.; Rolly, B.; Stout, B.; Bonod, N.; Bidault, S. Accelerated Single Photon Emission from Dye Molecule-Driven Nanoantennas Assembled on DNA. *Nat. Commun.* **2012**, *3* (1), 962.

(106) Würthner, F.; Kaiser, T. E.; Saha-Möller, C. R. J-Aggregates: From Serendipitous Discovery to Supramolecular Engineering of Functional Dye Materials. *Angew. Chemie Int. Ed.* **2011**, *50* (15), 3376–3410.

(107) Czikkely, V.; Försterling, H. D.; Kuhn, H. Light Absorption and Structure of Aggregates of Dye Molecules. *Chem. Phys. Lett.* **1970**, *6* (1), 11–14.

(108) Czikklely, V.; Forsterling, H. D.; Kuhn, H. Extended Dipole Model for Aggregates of Dye Molecules. *Chem. Phys. Lett.* **1970**, *6* (3), 207–210.

(109) Eisfeld, A.; Briggs, J. S. The J- and H-Bands of Organic Dye Aggregates. *Chem. Phys.* **2006**, *324* (2–3), 376–384.

(110) Eisfeld, A. A Simple Method to Obtain Information on the Conformation of Dipole–dipole Coupled Dimers. *Chem. Phys. Lett.* **2007**, *445* (4–6), 321–324.

(111) Takeuchi, T.; Matile, S. Sensing Applications of Synthetic Transport Systems. *Chem. Commun.* **2013**, *49* (1), 19–29.

(112) Chmeliov, J.; Songaila, E.; Rancova, O.; Gall, A.; Robert, B.; Abramavicius, D.; Valkunas, L. Excitons in the LH3 Complexes from Purple Bacteria. *J. Phys. Chem. B* **2013**, *117* (38), 11058–11068.

(113) Sundström, V. Femtobiology. *Annu. Rev. Phys. Chem.* **2008**, *59* (1), 53–77.

(114) Sundstro, V.; Grondelle, R. Van. Photosynthetic Light-Harvesting : Reconciling Dynamics and Structure of Purple Bacterial. **1999**, 2327–2346.

(115) Anna, J. M.; Scholes, G. D.; van Grondelle, R. A Little Coherence in Photosynthetic Light Harvesting. *Bioscience* **2014**, *64* (1), 14–25.

(116) JELLEY, E. E. Spectral Absorption and Fluorescence of Dyes in the Molecular State. *Nature* **1936**, *138* (3502), 1009–1010.

(117) West, W.; Pearce, S. The Dimeric State of Cyanine Dyes. *J. Phys. Chem.* **1965**, *69* (6), 1894–1903.

(118) Slavnova, T. D.; Chibisov, A. K.; Görner, H. Kinetics of Salt-Induced J-Aggregation of Cyanine Dyes. *J. Phys. Chem. A* **2005**, *109* (21), 4758–4765.

(119) Armitage, B.; Retterer, J.; Brien, D. F. O. Dimerization of Cyanine Dyes in Water Driven by Association with Hydrophobic Borate Anions. *J. Am. Chem. Soc.* **1993**, *115* (20), 10786–10790.

(120) Renge, I.; Wild, U. P. Solvent, Temperature, and Excitonic Effects in the Optical Spectra of Pseudoisocyanine Monomer and J-Aggregates. *J. Phys. Chem. A* **1997**, *101* (43), 7977–7988.

(121) von Berlepsch, H.; Böttcher, C.; Ouart, A.; Burger, C.; Dähne, S.; Kirstein, S. Supramolecular Structures of J -Aggregates of Carbocyanine Dyes in Solution. *J. Phys. Chem. B* **2000**, *104* (22), 5255–5262.

(122) Wang, M.; Silva, G. L.; Armitage, B. A. DNA-Templated Formation of a Helical Cyanine Dye J-Aggregate. *J. Am. Chem. Soc.* **2000**, *122* (41), 9977–9986.

(123) Hannah, K. C.; Armitage, B. A. DNA-Templated Assembly of Helical Cyanine Dye Aggregates: A Supramolecular Chain Polymerization. *Acc. Chem. Res.* **2004**, *37* (11), 845–853.

(124) Chen, W.; Schuster, G. B. DNA-Programmed Modular Assembly of Cyclic and Linear Nanoarrays for the Synthesis of Two-Dimensional Conducting Polymers. *J. Am. Chem. Soc.* **2012**, *134* (2), 840–843.

(125) Endo, M.; Shiroyama, T.; Fujitsuka, M.; Majima, T. Four-Way-Branched DNA−Porphyrin Conjugates for Construction of Four Double-Helix-DNA Assembled Structures. *J. Org. Chem.* **2005**, *70* (19), 7468–7472.

(126) Neelakandan, P. P.; Pan, Z.; Hariharan, M.; Zheng, Y.; Weissman, H.; Rybtchinski, B.; Lewis, F. D. Hydrophobic Self-Assembly of a Perylenediimide-Linked DNA Dumbbell into Supramolecular Polymers. *J. Am. Chem. Soc.* **2010**, *132* (44), 15808–15813.

(127) Brotschi, C.; Leumann, C. J. DNA with Hydrophobic Base Substitutes: A Stable, Zipperlike Recognition Motif Based On Interstrand-Stacking Interactions. *Angew. Chemie Int. Ed.* **2003**, *42* (14), 1655–1658.

(128) Kashida, H.; Asanuma, H.; Komiyama, M. Alternating Hetero H Aggregation of Different Dyes by Interstrand Stacking from Two DNA-Dye Conjugates. *Angew. Chemie* **2004**, *116* (47), 6684–6687.

(129) Asanuma, H.; Shirasuka, K.; Takarada, T.; Kashida, H.; Komiyama, M. DNA−Dye Conjugates for Controllable H* Aggregation 1. *J. Am. Chem. Soc.* **2003**, *125* (8), 2217–2223.

(130) Asanuma, H.; Fujii, T.; Kato, T.; Kashida, H. Coherent Interactions of Dyes Assembled on DNA. *J. Photochem. Photobiol. C Photochem. Rev.* **2012**, *13* (2), 124–135.

(131) Chen, W.; Schuster, G. B. Precise Sequence Control in Linear and Cyclic Copolymers of 2,5-Bis(2-Thienyl)Pyrrole and Aniline by DNA-Programmed Assembly. *J. Am. Chem. Soc.* **2013**, *135* (11), 4438–4449.

(132) Kashida, H.; Asanuma, H. Preparation of Supramolecular Chromophoric Assemblies Using a DNA Duplex. *Phys. Chem. Chem. Phys.* **2012**, *14* (20), 7196.

(133) Hannestad, J. K.; Gerrard, S. R.; Brown, T.; Albinsson, B. Self-Assembled DNA-Based Fluorescence Waveguide with Selectable Output. *Small* **2011**, *7* (22), 3178–3185.

(134) Özhalıcı-Ünal, H.; Armitage, B. A. Fluorescent DNA Nanotags Based on a Self-Assembled DNA Tetrahedron. *ACS Nano* **2009**, *3* (2), 425–433.

(135) Hannestad, J. K.; Sandin, P.; Albinsson, B. Self-Assembled DNA Photonic Wire for Long-Range Energy Transfer. *J. Am. Chem. Soc.* **2008**, *130* (47), 15889–15895.

(136) Bouamaied, I.; Nguyen, T.; Rühl, T.; Stulz, E. Supramolecular Helical Porphyrin Arrays Using DNA as a Scaffold. *Org. Biomol. Chem.* **2008**, *6* (21), 3888.

(137) Fendt, L.; Bouamaied, I.; Thöni, S.; Amiot, N.; Stulz, E. DNA as Supramolecular Scaffold for Porphyrin Arrays on the Nanometer Scale. *J. Am. Chem. Soc.* **2007**, *129* (49), 15319–15329.

(138) Kasha, M.; Rawls, H. R.; Ashraf El-Bayoumi, M. The Exciton Model in Molecular Spectroscopy. *Pure Appl. Chem.* **1965**, *11* (3–4), 371–392.

(139) Murphy, M. C.; Rasnik, I.; Cheng, W.; Lohman, T. M.; Ha, T. Probing Single-Stranded DNA Conformational Flexibility Using Fluorescence Spectroscopy. *Biophys. J.* **2004**, *86* (4), 2530–2537.

(140) Kopainsky, B.; Hallermeier, J. K.; Kaiser, W. The First Step of Aggregation of Pic: The Dimerization. *Chem. Phys. Lett.* **1981**, *83* (3), 498–502.

(141) Laurent, A. D.; Jacquemin, D. TD-DFT Benchmarks: A Review. *Int. J. Quantum Chem.* **2013**, *113* (17), 2019–2039.

(142) Lin, K. T. H.; Silzel, J. W. Relation of Molecular Structure to Franck–Condon Bands in the Visible-Light Absorption Spectra of Symmetric Cationic Cyanine Dyes. *Spectrochim. Acta Part A Mol. Biomol. Spectrosc.* **2015**, *142*, 210–219.

(143) Bertolino, C. A.; Ferrari, A. M.; Barolo, C.; Viscardi, G.; Caputo, G.; Coluccia, S. Solvent Effect on Indocyanine Dyes: A Computational Approach. *Chem. Phys.* **2006**, *330*, 52–59.

(144) Yamaoka, K.; Resnik, R. A. The Extrinsic Cotton Effect of Acridine Orange Bound to Native DNA and Helical Poly-α,L-Glutamic Acid 1. *J. Phys. Chem.* **1966**, *70* (12), 4051–4066.

(145) Seibt, J.; Lohr, A.; Würthner, F.; Engel, V. Circular Dichroism and Absorption Spectroscopy of Merocyanine Dimer Aggregates: Molecular Properties and Exciton Transfer Dynamics from Time-Dependent Quantum Calculations. *Phys. Chem. Chem. Phys.* **2007**, *9* (47), 6214.

(146) Heilemann, M.; Tinnefeld, P.; Mosteiro, G. S.; Parajo, M. G.; Van Hulst, N. F.; Sauer, M. Multistep Energy Transfer in Single Molecular Photonic Wires. *J. Am. Chem. Soc.* **2004**, *126* (21), 6514–6515.

(147) Tinnefeld, P.; Heilemann, M.; Sauer, M. Design of Molecular Photonic Wires Based on Multistep Electronic Excitation Transfer. *ChemPhysChem* **2005**, *6* (2), 217–222.

(148) Adeyemi, O. O.; Malinovskii, V. L.; Biner, S. M.; Calzaferri, G.; Häner, R. Photon Harvesting by Excimer-Forming Multichromophores. *Chem. Commun.* **2012**, *48* (77), 9589.

(149) Buckhout-White, S.; Spillmann, C. M.; Algar, W. R.; Khachatrian, A.; Melinger, J. S.; Goldman, E. R.; Ancona, M. G.; Medintz, I. L. Assembling Programmable FRET-Based Photonic Networks Using Designer DNA Scaffolds. *Nat. Commun.* **2014**, *5*, 5615.

(150) Stein, I. H.; Steinhauer, C.; Tinnefeld, P. Single-Molecule Four-Color FRET Visualizes Energy-Transfer Paths on DNA Origami. *J. Am. Chem. Soc.* **2011**, *133* (12), 4193–4195.

(151) Stein, I. H.; Schüller, V.; Böhm, P.; Tinnefeld, P.; Liedl, T. Single-Molecule FRET Ruler Based on Rigid DNA Origami Blocks. *ChemPhysChem* **2011**, *12* (3), 689–695.

(152) Klein, W. P.; Díaz, S. A.; Buckhout-White, S.; Melinger, J. S.; Cunningham, P. D.; Goldman, E. R.; Ancona, M. G.; Kuang, W.; Medintz, I. L. Utilizing HomoFRET to Extend DNA-Scaffolded Photonic Networks and Increase Light-Harvesting Capability. *Adv. Opt. Mater.* **2018**, *6* (1), 1–12.

(153) Douglas, S. M.; Chou, J. J.; Shih, W. M. DNA-Nanotube-Induced Alignment of Membrane Proteins for NMR Structure Determination. *Proc. Natl. Acad. Sci.* **2007**, *104* (16), 6644–6648.

(154) Stahl, E.; Martin, T. G.; Praetorius, F.; Dietz, H. Facile and Scalable Preparation of Pure and Dense DNA Origami Solutions. *Angew. Chemie Int. Ed.* **2014**, *53* (47), 12735–12740.

(155) Bai, X. -c.; Martin, T. G.; Scheres, S. H. W.; Dietz, H. Cryo-EM Structure of a 3D DNA-Origami Object. *Proc. Natl. Acad. Sci.* **2012**, *109* (49), 20012–20017.

(156) Fischer, S.; Hartl, C.; Frank, K.; Rädler, J. O.; Liedl, T.; Nickel, B. Shape and Interhelical Spacing of DNA Origami Nanostructures Studied by Small-Angle X-Ray Scattering. *Nano Lett.* **2016**, *16* (7), 4282–4287.

(157) Bartell, L. S. On the Length of the Carbon-Carbon Single Bond. *J. Am. Chem. Soc.* **1959**, *81* (14), 3497–3498.

(158) Sindbert, S.; Kalinin, S.; Nguyen, H.; Kienzler, A.; Clima, L.; Bannwarth, W.; Appel, B.; Müller, S.; Seidel, C. A. M. Accurate Distance Determination of Nucleic Acids via Förster Resonance Energy Transfer: Implications of Dye Linker Length and Rigidity. *J. Am. Chem. Soc.* **2011**, *133* (8), 2463–2480.

(159) Spiriti, J.; Binder, J. K.; Levitus, M.; van der Vaart, A. Cy3-DNA Stacking Interactions Strongly Depend on the Identity of the Terminal Basepair. *Biophys. J.* **2011**, *100* (4), 1049–1057.

(160) Sanborn, M. E.; Connolly, B. K.; Gurunathan, K.; Levitus, M. Fluorescence Properties and Photophysics of the Sulfoindocyanine Cy3 Linked Covalently to DNA. *J. Phys. Chem. B* **2007**, *111* (37), 11064–11074.

(161) Sigel, R. K. O.; Sigel, H. A Stability Concept for Metal Ion Coordination to Single-Stranded Nucleic Acids and Affinities of Individual Sites. *Acc. Chem. Res.* **2010**, *43* (7), 974–984.

(162) Park, H.; Heldman, N.; Rebentrost, P.; Abbondanza, L.; Iagatti, A.; Alessi, A.; Patrizi, B.; Salvalaggio, M.; Bussotti, L.; Mohseni, M.; *et al*. Enhanced Energy Transport in Genetically Engineered Excitonic Networks. *Nat. Mater.* **2015**, *15* (2), 211–216.

(163) Cunningham, P. D.; Khachatrian, A.; Buckhout-White, S.; Deschamps, J. R.; Goldman, E. R.; Medintz, I. L.; Melinger, J. S. Resonance Energy Transfer in DNA Duplexes Labeled with Localized Dyes. *J. Phys. Chem. B* **2014**, *118* (50), 14555–14565.

(164) Di Fiori, N.; Meller, A. The Effect of Dye-Dye Interactions on the Spatial Resolution of Single-Molecule FRET Measurements in Nucleic Acids. *Biophys. J.* **2010**, *98* (10), 2265–2272.

(165) Iqbal, A.; Arslan, S.; Okumus, B.; Wilson, T. J.; Giraud, G.; Norman, D. G.; Ha, T.; Lilley, D. M. J. Orientation Dependence in Fluorescent Energy Transfer between Cy3 and Cy5 Terminally Attached to Double-Stranded Nucleic Acids. *Proc. Natl. Acad. Sci.* **2008**, *105* (32), 11176–11181.

(166) Ivanov, V.; Li, M.; Mizuuchi, K. Impact of Emission Anisotropy on Fluorescence Spectroscopy and FRET Distance Measurements. *Biophys. J.* **2009**, *97* (3), 922–929.

(167) Alivisatos, A. P.; Johnsson, K. P.; Peng, X.; Wilson, T. E.; Loweth, C. J.; Bruchez, M. P.; Schultz, P. G. Organization of "nanocrystal Molecules" Using DNA. *Nature*. 1996, pp 609–611.

(168) Mirkin, C. A.; Letsinger, R. L.; Mucic, R. C.; Storhoff, J. J. A DNA-Based Method for Rationally Assembling Nanoparticles into Macroscopic Materials. *Nature* **1996**, *382* (6592), 607–609.

(169) Hurst, S. J.; Lytton-Jean, A. K. R.; Mirkin, C. A. Maximizing DNA Loading on a Range of Gold Nanoparticle Sizes. *Anal. Chem.* **2006**, *78* (24), 8313–8318.

(170) Sun, D.; Gang, O. DNA-Functionalized Quantum Dots: Fabrication, Structural, and Physicochemical Properties. *Langmuir* **2013**, *29* (23), 7038–7046.

(171) Samanta, A.; Deng, Z.; Liu, Y.; Yan, H. A Perspective on Functionalizing Colloidal Quantum Dots with DNA. *Nano Res.* **2013**, *6* (12), 853–870.

(172) Mitchell, G. P.; Mirkin, C. A.; Letsinger, R. L. Programmed Assembly of DNA Functionalized Quantum Dots. *J. Am. Chem. Soc.* **1999**, *121* (35), 8122–8123.

(173) Medintz, I. L.; Berti, L.; Pons, T.; Grimes, A. F.; English, D. S.; Alessandrini, A.; Facci, P.; Mattoussi, H. A Reactive Peptidic Linker for Self-Assembling Hybrid Quantum Dot-DNA Bioconjugates. *Nano Lett.* **2007**, *7* (6), 1741–1748.

(174) Sharma, J.; Ke, Y.; Lin, C.; Chhabra, R.; Wang, Q.; Nangreave, J.; Liu, Y.; Yan, H. DNA-Tile-Directed Self-Assembly of Quantum Dots into Two-Dimensional Nanopatterns. *Angew. Chemie - Int. Ed.* **2008**, *47* (28), 5157–5159.

(175) Bui, H.; Onodera, C.; Kidwell, C.; Tan, Y.; Graugnard, E.; Kuang, W.; Lee, J.; Knowlton, W. B.; Yurke, B.; Hughes, W. L. Programmable Periodicity of Quantum Dot Arrays with DNA Origami Nanotubes. *Nano Lett.* **2010**, *10* (9), 3367–3372.

(176) Wang, Q.; Liu, Y.; Ke, Y.; Yan, H. Quantum Dot Bioconjugation during Core-Shell Synthesis. *Angew. Chemie - Int. Ed.* **2008**, *47* (2), 316–319.

(177) Deng, Z.; Samanta, A.; Nangreave, J.; Yan, H.; Liu, Y. Robust DNA-Functionalized Core/Shell Quantum Dots with Fluorescent Emission Spanning from UV-Vis to near-IR and Compatible with DNA-Directed Self-Assembly. *J. Am. Chem. Soc.* **2012**, *134* (42), 17424–17427.

(178) Tikhomirov, G.; Hoogland, S.; Lee, P. E.; Fischer, A.; Sargent, E. H.; Kelley, S. O. DNA-Based Programming of Quantum Dot Valency, Self-Assembly and Luminescence. *Nat. Nanotechnol.* **2011**, *6* (8), 485–490.

(179) Farlow, J.; Seo, D.; Broaders, K. E.; Taylor, M. J.; Gartner, Z. J.; Jun, Y. W. Formation of Targeted Monovalent Quantum Dots by Steric Exclusion. *Nat. Methods* **2013**, *10* (12), 1203–1205.

(180) Shen, J.; Tang, Q.; Li, L.; Li, J.; Zuo, X.; Qu, X.; Pei, H.; Wang, L.; Fan, C. Valence-Engineering of Quantum Dots Using Programmable DNA Scaffolds. *Angew. Chemie - Int. Ed.* **2017**, *56* (50), 16077–16081.

(181) Yao, G.; Pei, H.; Li, J.; Zhao, Y.; Zhu, D.; Zhang, Y.; Lin, Y.; Huang, Q.; Fan, C. Clicking DNA to Gold Nanoparticles: Poly-Adenine-Mediated Formation of Monovalent DNA-Gold Nanoparticle Conjugates with Nearly Quantitative Yield. *NPG Asia Mater.* **2015**, *7* (1), e159.

(182) Shen, J.; Tang, Q.; Li, L.; Li, J.; Zuo, X.; Qu, X.; Pei, H.; Wang, L.; Fan, C. Valence-Engineering of Quantum Dots Using Programmable DNA Scaffolds. *Angew. Chemie Int. Ed.* **2017**, *56* (50), 16077–16081.

(183) Simoncelli, S.; Roller, E.-M.; Urban, P.; Schreiber, R.; Turberfield, A. J.; Liedl, T.; Lohmüller, T. Quantitative Single-Molecule Surface-Enhanced Raman Scattering by Optothermal Tuning of DNA Origami-Assembled Plasmonic Nanoantennas. *ACS Nano* **2016**, *10* (11), 9809–9815.

(184) Benson, O. Assembly of Hybrid Photonic Architectures from Nanophotonic Constituents. *Nature* **2011**, *480* (7376), 193–199.

(185) Novotny, L.; van Hulst, N. Antennas for Light. *Nat. Photonics* **2011**, *5* (2), 83–90.

(186) Hoang, T. B.; Akselrod, G. M.; Argyropoulos, C.; Huang, J.; Smith, D. R.; Mikkelsen, M. H. Ultrafast Spontaneous Emission Source Using Plasmonic Nanoantennas. *Nat. Commun.* **2015**, *6* (1), 7788.

(187) Hoang, T. B.; Akselrod, G. M.; Mikkelsen, M. H. Ultrafast Room-Temperature Single Photon Emission from Quantum Dots Coupled to Plasmonic Nanocavities. *Nano Lett.* **2016**, *16* (1), 270–275.

(188) Skoff, S. M.; Rauschenbeutel, A. Focus on a Single Molecule. *Nat. Photonics* **2016**, *10* (7), 438–440.

(189) Boardman, A. D.; Zayats, A. V. Nonlinear Plasmonics. In *Handbook of Surface Science*; Nature Publishing Group, 2014; Vol. 4, pp 329–347.

(190) Sauvan, C.; Hugonin, J. P.; Maksymov, I. S.; Lalanne, P. Theory of the Spontaneous Optical Emission of Nanosize Photonic and Plasmon Resonators. *Phys. Rev. Lett.* **2013**, *110* (23), 237401.

(191) Manfrinato, V. R.; Zhang, L.; Su, D.; Duan, H.; Hobbs, R. G.; Stach, E. A.; Berggren, K. K. Resolution Limits of Electron-Beam Lithography toward the Atomic Scale. *Nano Lett.* **2013**, *13* (4), 1555–1558.

(192) Scholder, O.; Jefimovs, K.; Shorubalko, I.; Hafner, C.; Sennhauser, U.; Bona, G. L. Helium Focused Ion Beam Fabricated Plasmonic Antennas with Sub-5 Nm Gaps. *Nanotechnology* **2013**, *24* (39).

(193) Cohen-Hoshen, E.; Bryant, G. W.; Pinkas, I.; Sperling, J.; Bar-Joseph, I. Exciton–Plasmon Interactions in Quantum Dot–Gold Nanoparticle Structures. *Nano Lett.* **2012**, *12* (8), 4260–4264.

(194) Acuna, G. P.; Moller, F. M.; Holzmeister, P.; Beater, S.; Lalkens, B.; Tinnefeld, P. Fluorescence Enhancement at Docking Sites of DNA-Directed Self-Assembled Nanoantennas. *Science (80-.).* **2012**, *338* (6106), 506–510.

(195) Thacker, V. V.; Herrmann, L. O.; Sigle, D. O.; Zhang, T.; Liedl, T.; Baumberg, J. J.; Keyser, U. F. DNA Origami Based Assembly of Gold Nanoparticle Dimers for Surface-Enhanced Raman Scattering. *Nat. Commun.* **2014**, *5*, 1–7.

(196) Simoncelli, S.; Roller, E.-M.; Urban, P.; Schreiber, R.; Turberfield, A. J.; Liedl, T.; Lohmueller, T. Quantitative Single Molecule Surface-Enhanced Raman Scattering by Optothermal Tuning of DNA Origami-Assembled Plasmonic Nanoantennas. *ACS Nano* **2016**, acsnano.6b05276.

(197) Roller, E.-M.; Argyropoulos, C.; Högele, A.; Liedl, T.; Pilo-Pais, M. Plasmon–Exciton Coupling Using DNA Templates. *Nano Lett.* **2016**, *16* (9), 5962–5966.

(198) Busson, M. P.; Rolly, B.; Stout, B.; Bonod, N.; Larquet, E.; Polman, A.; Bidault, S. Optical and Topological Characterization of Gold Nanoparticle Dimers Linked by a Single DNA Double Strand. *Nano Lett.* **2011**, *11* (11), 5060–5065.

(199) Lee, Y.-J.; Schade, N. B.; Sun, L.; Fan, J. A.; Bae, D. R.; Mariscal, M. M.; Lee, G.; Capasso, F.; Sacanna, S.; Manoharan, V. N.; *et al.* Ultrasmooth, Highly Spherical Monocrystalline Gold Particles for Precision Plasmonics. *ACS Nano* **2013**, *7* (12), 11064–11070.

(200) Lee, J.; Huh, J. H.; Kim, K.; Lee, S. DNA Origami-Guided Assembly of the Roundest 60–100 Nm Gold Nanospheres into Plasmonic Metamolecules. *Adv. Funct. Mater.* **2018**, *28* (15), 1–13.

(201) Vietz, C.; Kaminska, I.; Sanz Paz, M.; Tinnefeld, P.; Acuna, G. P. Broadband Fluorescence Enhancement with Self-Assembled Silver Nanoparticle Optical Antennas. *ACS Nano* **2017**, *11* (5), 4969–4975.

(202) Bharadwaj, P.; Novotny, L. Spectral Dependence of Single Molecule Fluorescence Enhancement. *Opt. Express* **2007**, *15* (21), 14266.

(203) Neumann, A.; Lindlau, J.; Högele, A. Contamination of Polymethylmethacrylate by Organic Quantum Emitters. **2017**.

(204) Rabouw, F. T.; Cogan, N. M. B.; Berends, A. C.; Stam, W. Van Der; Vanmaekelbergh, D.; Koenderink, A. F.; Krauss, T. D.; Donega, C. D. M. Non-Blinking Single-Photon Emitters in Silica. *Sci. Rep.* **2016**, *6* (January), 1–7.

(205) Wang, X.; Ren, X.; Kahen, K.; Hahn, M. A.; Rajeswaran, M.; Maccagnano-Zacher, S.; Silcox, J.; Cragg, G. E.; Efros, A. L.; Krauss, T. D. Retraction: Non-Blinking Semiconductor Nanocrystals. *Nature* **2015**, *527* (7579), 544–544.

(206) Bharadwaj, P.; Novotny, L. Robustness of Quantum Dot Power-Law Blinking. *Nano Lett.* **2011**, *11* (5), 2137–2141.

(207) Rabouw, F. T.; Kamp, M.; van Dijk-Moes, R. J. A.; Gamelin, D. R.; Koenderink, A. F.; Meijerink, A.; Vanmaekelbergh, D. Delayed Exciton Emission and Its Relation to Blinking in CdSe Quantum Dots. *Nano Lett.* **2015**, *15* (11), 7718–7725.

(208) Nikoobakht, B.; Wang, Z. L.; El-Sayed, M. A. Self-Assembly of Gold Nanorods. *J. Phys. Chem. B* **2000**, *104* (36), 8635–8640.

(209) Xu, Z.-C.; Shen, C.-M.; Xiao, C.-W.; Yang, T.-Z.; Chen, S.-T.; Li, H.-L.; Gao, H.-J. Fabrication of Gold Nanorod Self-Assemblies from Rod and Sphere Mixtures via Shape Self-Selective Behavior. *Chem. Phys. Lett.* **2006**, *432* (1–3), 222–225.

(210) Sims, P. J.; Waggoner, A. S.; Wang, C.-H.; Hoffman, J. F. Mechanism by Which Cyanine Dyes Measure Membrane Potential in Red Blood Cells and Phosphatidylcholine Vesicles. *Biochemistry* **1974**, *13*, 3315–3330.

(211) Ghosh, G.; Palik, E. D. *Handbook of Optical Constants of Solids*; Academic Press, 1985.

(212) Ciracì, C.; Rose, A.; Argyropoulos, C.; Smith, D. R. Numerical Studies of the Modification of Photodynamic Processes by Film-Coupled Plasmonic Nanoparticles. *J. Opt. Soc. Am. B* **2014**, *31* (11), 2601.

Acknowledgements

My first big thank you goes to Tim for welcoming and mentoring me as one of his PhD student. Four (and something) years ago you trusted that I could be a valuable addition to the group, and that I could take on challenges in a field that was very new to me. Thank you for the trust and for the freedom I had during my projects, I believe that the independence I acquired as a result will greatly benefit my future scientific career. I am looking forward to keep working together in the future.

Thank you to the present and past members of the Liedl group: Alex, Amelie, Arthur, Caro, Eva, Ian, Kevin, Linh, Luisa, Luzia, Mauricio, Nils, Philipp, Samet, Susi, Tao, Timon, Vale, Wooli. You have been fantastic colleagues and friends. There is a strong collaborative spirit and mutual support in the group, keep it up!

Thank you to Prof. Joachim Rädler and the whole chair. I really enjoy my time working side-by-side with you, the parties and the chair trips. Special thanks to Rafal, for our late-night scientific/philosophical conversations. They kept me sane during the down times.

Thank you to all my collaborators and co-authors, this work would not have been possible without you. Special thanks to Mauricio for putting up with my ups and downs, my scientific doubts and questions, in so many projects, for so long.

Thank you to Alex and Fabian, my bachelor students. I learned so much from supervising your work and discussing with you.

Thank you to my hiking group: Claudia, Franceline and Susi. Keeping my hobbies alive was fundamental to keep going with the work of these years. The time spent in the mountains with you has been always a breath of fresh air (literally and figuratively).

Un grosso grazie alla mia famiglia senza la quale non sarei a questo punto. Grazie per non aver mai dubitato che ce l’avrei fatta e per avermi dato un supporto incondizionato in questi (tantissimi) anni di università.

To Dave, thank you for your support and patience, and for always believing me. I could not have made it sane to the end without you.